

---

Electronic Thesis and Dissertation Repository

---

6-9-2017 12:00 AM

## Evolution of Cu<sub>2</sub>O Morphology During Copper Corrosion in the Presence of Gamma-Radiation

Arielle M. Jean

*The University of Western Ontario*

Supervisor

Dr. J. Clara Wren


*The University of Western Ontario*

Graduate Program in Chemistry

A thesis submitted in partial fulfillment of the requirements for the degree in Master of Science

© Arielle M. Jean 2017

Follow this and additional works at: <https://ir.lib.uwo.ca/etd>

 Part of the [Analytical Chemistry Commons](#), [Materials Chemistry Commons](#), [Physical Chemistry Commons](#), and the [Radiochemistry Commons](#)

---

### Recommended Citation

Jean, Arielle M., "Evolution of Cu<sub>2</sub>O Morphology During Copper Corrosion in the Presence of Gamma-Radiation" (2017). *Electronic Thesis and Dissertation Repository*. 4593.

<https://ir.lib.uwo.ca/etd/4593>

This Dissertation/Thesis is brought to you for free and open access by Scholarship@Western. It has been accepted for inclusion in Electronic Thesis and Dissertation Repository by an authorized administrator of Scholarship@Western. For more information, please contact [wlsadmin@uwo.ca](mailto:wlsadmin@uwo.ca).

## Abstract

In this work, experiments were carried out in order to develop a mechanistic understanding of the corrosion of copper metal in limited water volumes under gamma-radiation ( $\gamma$ -radiation). When exposed to  $\gamma$ -radiation, water decomposes into chemically reactive oxidizing and reducing species. Under a continuous radiation flux, the concentrations of the radiolytically produced oxidants eventually reach a pseudo-steady state that can influence the corrosion kinetics of metallic surfaces.

The evolution of the surface morphology during water droplet corrosion of copper in the presence of  $\gamma$ -radiation was investigated as a function of irradiation time and pH. The oxide growth kinetics were studied by measuring the amount of dissolved copper in the test solution after irradiation, and analyzing the oxide composition and morphology on the metal surface as a function of time.

The predominant corrosion product was copper (I) oxide ( $\text{Cu}_2\text{O}$ ). The detailed analysis carried out here of  $\text{Cu}_2\text{O}$  formation and growth has allowed a mechanism for radiolytic copper corrosion to be proposed. The mechanism consists of three stages: 1. initial oxidation of  $\text{Cu}^0(\text{m})$  to  $\text{Cu}^{2+}(\text{aq})$ , 2.  $\text{Cu}_2\text{O}$  crystal growth via reduction, and 3. redox-cycle-assisted ripening of  $\text{Cu}_2\text{O}$  crystals. Each stage consists of elementary steps whose reaction rates can impact the kinetics of particle growth and influence the final morphologies of the particles observed on the metal surface. The results and derived mechanism show that the morphology of the oxide formed on the metal surface affects the corrosion rate of the metal. This work could offer critical insights into the corrosion behaviour of copper-coated spent nuclear fuel containers exposed to  $\gamma$ -radiation in a deep geologic repository. The non-uniformity of the evolution of surface

morphology observed in different regions on the copper surface indicate that the corrosion of copper could be highly variable under deep geologic repository conditions.

**Keywords:** polymorphic copper oxide, radiolytic corrosion of copper, steady-state radiolysis, gamma-radiation, copper corrosion

## Co-Authorship Statement

All chapters in this thesis were co-authored by my supervisor, Dr. J. Clara Wren. The roles of others are described below:

Chapter 2: R. Morco provided humid-air radiolysis modeling results that were used to interpret some of the results in this thesis.

Chapter 3: J. Joseph assisted in designing the experimental set-up.

Chapter 4: G. Whitaker assisted in operating the optical microscope for surface analysis. T. Simpson performed FIB analyses.

Chapter 5: M. Nagizhadeh, M. Momeni, and G. Whitaker assisted with surface analysis.

## **Acknowledgements**

I would like to thank my supervisor, Dr. Clara Wren, for her support, guidance, and patience throughout my studies. Thank you for giving me the opportunity to learn from you and your brilliant research group.

I would like to thank the Wren group members for always being kind and helpful. It was a pleasure getting to know all of you, and I learned so much from each one of you. I would like to thank Dr. Jiju Joseph, who provided laboratory training when I first joined the group, assisted in developing experimental procedures, and edited all of my work. Thank you for your time and patience. I would not have been able to complete this project without your guidance. Thank you to our research associate, Giles Whitaker, for assisting in surface analysis and designing graphics for our group. We are truly lucky to have you. Thank you to Masi Naghizadeh and Mojtaba Momeni, who assisted with surface analysis; your help was truly appreciated.

I would also like to thank the teams at Western Nanofabrication Facility and Surface Science Western, for providing surface analysis training that was integral to the results for this thesis.

Last, but certainly not least, thank you to my friends and family who have supported me throughout my academic career. I would not have succeeded without your love and support, and I am so grateful for each and every one of you.

## Table of Contents

Abstract .....	ii
Co-Authorship Statement .....	iv
Acknowledgments .....	v
Table of Contents .....	vi
List of Tables .....	ix
List of Figures .....	x
List of Symbols and Abbreviations .....	xiv
<b>Chapter 1</b> .....	1
1 Introduction .....	1
1.1 General Introduction .....	1
1.2 Thesis Objectives and Outline .....	6
1.3 References .....	7
<b>Chapter 2</b> .....	8
2 Background and Literature Review .....	11
2.1 Materials Background .....	11
2.1.1 Copper Metal .....	11
2.1.2 Electrochemical Potentials of Copper Redox Reactions .....	11
2.1.3 Solubilities of Copper Ions .....	12
2.1.3 Crystal Structures of Copper Oxides .....	13
2.1.5 Evolution of Crystal Morphology During Its Growth .....	16
2.1.6 Synthesis of Cu <sub>2</sub> O Crystals of Different Morphologies .....	17
2.2 Radiation Chemistry .....	21
2.2.1 Radiation Chemistry and Photochemistry .....	21
2.2.1 Types of Ionizing Radiation .....	21
2.2.3 Interaction of Radiation with Matter .....	23
2.2.4 Time Evolution of Radiolysis Product Concentration .....	27
2.2.5 Radiation Induced Nanoparticle Formation .....	32
2.3 References .....	34

<b>Chapter 3</b> .....	41
3 Experimental Principles and Procedures .....	41
3.1 Surface Analysis Techniques .....	41
3.1.1 Digital Microscopy.....	41
3.1.2 Raman Spectroscopy .....	42
3.1.3 Scanning Electron Microscopy and Energy Dispersive X-ray Spectroscopy .....	43
3.1.4 Focused-Ion Beam Milling .....	45
3.1.5 X-ray Diffraction .....	45
3.2 Chemical Analysis Techniques .....	46
3.2.1 Inductively Coupled Plasma Mass Spectrometry .....	46
3.3 Experimental Procedures .....	47
3.3.1 Sample Preparation .....	47
3.4 Irradiation Technique .....	47
3.4.1 Sample Irradiation .....	47
3.4.2 Fricke Dosimetry .....	48
3.5 Sample Analyses after Irradiation .....	49
3.6 References .....	50
<b>Chapter 4</b> .....	51
4 Evolution of Surface Morphology During Corrosion of Rectangular Copper Coupons Under 200 $\mu$ L Water Droplets .....	51
4.1 Introduction .....	51
4.2 Experimental Details .....	52
4.2.1 Sample Preparation and Test Procedure .....	52
4.2.2 Test Analyses .....	53
4.3 Results and Discussion .....	53
4.3.1 Progression of Overall Surface .....	53
4.3.2 Evolution of Morphology of Different Areas Across Surface .....	58
4.3 Summary .....	81
4.4 References .....	82

<b>Chapter 5</b> .....	83
5 Evolution of Surface Morphology During Corrosion of Circular Copper Coupons Under 50 $\mu$ L Water Droplets .....	83
5.1 Introduction .....	83
5.2 Experimental Details .....	83
5.3 Results and Discussion .....	84
5.3.1 Overall Progression of Copper Corrosion .....	84
5.3.2 Surface Variation in Corrosion Progression .....	89
5.3.3 Corrosion Progression of Different Areas .....	93
5.4 Summary .....	98
5.5 References .....	100
<b>Chapter 6</b> .....	93
6 Mechanism of $\text{Cu}_2\text{O}$ Formation and Growth During Water Droplet Corrosion of Copper .....	93
6.1 Proposed Mechanism of Water Droplet Corrosion of Copper .....	93
6.2 Summary .....	111
6.3 References .....	113
<b>Chapter 7</b> .....	115
7 Conclusions and Future Work .....	115
<b>Curriculum Vitae</b> .....	118



## List of Tables

<b>Table 5.1:</b> Values of the concentrations of copper species dissolved in the water droplets from the coupons whose optical micrographs are shown in Figure 5.2. ....	87
---	----

## List of Figures

<b>Figure 1.1</b> An illustration of the Mark II used fuel container proposed by the NWMO. ....	1
<b>Figure 1.2:</b> Shape evolution of Cu <sub>2</sub> O crystals from cubes, truncated cube, truncated octahedral, and octahedral. ....	4
<b>Figure 2.1:</b> Redox reactions between Cu <sup>0</sup> , Cu <sup>+</sup> and Cu <sup>2+</sup> and their standard redox potentials. ...	12
<b>Figure 2.2:</b> The solubility of Cu <sup>+</sup> and Cu <sup>2+</sup> as a function of pH. ....	13
<b>Figure 2.3:</b> The fcc structure of Cu, cubic structure of Cu <sub>2</sub> O and monoclinic structure of CuO. ....	14
<b>Figure 2.4:</b> The fcc packing of Cu atoms, bcc packing of O atoms and cubic structure of Cu <sub>2</sub> O. The schematics were adapted from Chen et al. and redrawn for this thesis. ....	15
<b>Figure 2.5:</b> Schematic of the Cu <sub>2</sub> O crystal unit cell structure and some crystallographic planes. The unit cell consists of fcc packing of Cu atoms and bcc packing of O atoms. For the Cu atoms, only those that are coordinated with the body-centred O atom are shown for clarity. ....	15
<b>Figure 2.6:</b> Schematic showing the different shapes of single Cu <sub>2</sub> O crystals with increasing growth time. ....	17
<b>Figure 2.7:</b> The radiation track of a fast electron (spur size not to scale). ....	23
<b>Figure 2.8:</b> Schematic of the cascade of events that occur in irradiated water to generate the primary radiolysis products. ....	25
<b>Figure 2.9:</b> Schematic of water radiolysis reaction mechanism under long-term (>ms) continuous irradiation. ....	26
<b>Figure 2.10:</b> Calculated concentrations of radiolysis products formed as a function of irradiation time during irradiation of (a) deaerated water and (b) aerated water for pH 6.0 and 9.0 at 25 °C, and a dose rate of 3.0 kGy·h <sup>-1</sup> . ....	29
<b>Figure 2.11:</b> Concentrations of nitrogen species calculated using the humid air radiolysis model for radiolysis of 0% RH, 10% RH, and 85% RH air at 25 °C and a dose rate of 3 kGy·h <sup>-1</sup> . ....	31
<b>Figure 3.1:</b> Illustration showing IR absorption, Rayleigh scattering, Stokes shift, and Anti-	

Stokes shift processes. Arrows pointing upward correspond to light absorption processes, while those pointing downward correspond to light emitting processes. ....	42
<b>Figure 3.2:</b> Illustration of scanning electron microscope (SEM). ....	44
<b>Figure 3.3:</b> Illustration of Energy dispersive x-ray (EDX) spectroscopic technique. ....	44
<b>Figure 3.4:</b> Illustration of X-ray diffraction (XRD) technique. ....	45
<b>Figure 3.5:</b> Illustration of inductively coupled plasma mass spectrometry (ICP-MS). ....	46
<b>Figure 3.6:</b> Schematic representation of the reactions occurring during Fricke dosimetry. ....	48
<b>Figure 4.1:</b> A 200 $\mu\text{L}$ water droplet on the surface of a rectangular copper metal surface. ....	51
<b>Figure 4.2:</b> Optical micrographs of Cu coupons corroded in aerated water at pH 9.0 for different durations in the presence of $\gamma$ -radiation at dose rate of $3.0 \text{ kGy}\cdot\text{h}^{-1}$ . ....	54
<b>Figure 4.3:</b> Raman spectra of the surfaces of the Cu coupons corroded for different periods (24, 48 and 96 h) at pH 9.0 in aerated water in the presence of $\gamma$ -radiation at $3.0 \text{ kGy}\cdot\text{h}^{-1}$ . ....	56
<b>Figure 4.4:</b> XRD spectra of the surfaces of the Cu coupons corroded for different periods (24, 48 and 96 h) at pH 9.0 in aerated water in the presence of $\gamma$ -radiation at $3.0 \text{ kGy}\cdot\text{h}^{-1}$ . ....	57
<b>Figure 4.5:</b> (a) Optical and (b) SEM micrographs with various magnifications of a Cu coupon corroded for 24 h in aerated water at pH 9.0 in the presence of $\gamma$ -radiation at a dose rate of $3.0 \text{ kGy}\cdot\text{h}^{-1}$ . The areas where the images were taken are indicated in the low-magnification optical micrograph shown on the top. ....	60
<b>Figure 4.6:</b> (a) Optical and (b) SEM micrographs with various magnifications of a Cu coupon corroded for 36 h in aerated water at pH 9.0 in the presence of $\gamma$ -radiation at a dose rate of $3.0 \text{ kGy}\cdot\text{h}^{-1}$ . ....	62
<b>Figure 4.7:</b> Optical micrographs with various magnifications of different areas of a Cu coupon corroded for 48 h in aerated water at pH 9.0 in the presence of $\gamma$ -radiation at dose rate of $3.0 \text{ kGy}\cdot\text{h}^{-1}$ . ....	64
<b>Figure 4.8:</b> Comparison of optical micrographs of the areas containing circular oxide islands separated by narrow channels on Cu coupons corroded for 36 h and 48 h in aerated water at pH	

9.0 in the presence of  $\gamma$ -radiation at dose rate of  $3.0 \text{ kGy}\cdot\text{h}^{-1}$ . .....66

**Figure 4.9:** Optical and SEM micrographs of the boundary region (area d of Figure 7) on a Cu coupon corroded for 48 h in aerated water at pH 9.0 in the presence of  $\gamma$ -radiation at a dose rate of  $3.0 \text{ kGy}\cdot\text{h}^{-1}$ . .....67

**Figure 4.10:** Optical and SEM micrographs of the oxide island region (area c of Figure 4.7) on a Cu coupon corroded for 48 h in aerated water at pH 9.0 in the presence of  $\gamma$ -radiation at a dose rate of  $3.0 \text{ kGy}\cdot\text{h}^{-1}$ . .....69

**Figure 4.11:** Optical micrographs of different areas on the surface of a Cu coupon corroded for 72 h at pH 9.0 in aerated water with radiation at a dose rate of  $3 \text{ kGy}\cdot\text{h}^{-1}$ . The approximate areas where the micrographs were taken are marked in the low magnification optical image shown on the top. ....71

**Figure 4.12:** Optical micrographs of the areas showing partially dissolved  $\text{Cu}_2\text{O}$  crystals on a Cu coupon irradiated for 72 h at pH 9.0 in aerated water. The approximate spots where the micrographs were taken are marked in the low magnification optical image shown on the top. .72

**Figure 4.13:** SEM micrographs of the areas showing partially dissolved  $\text{Cu}_2\text{O}$  crystals on a Cu coupon irradiated for 72 h at pH 9.0 in aerated water. ....73

**Figure 4.14:** Optical and SEM micrographs with different magnifications of a focal area of the purple concentric crescent islands on a Cu coupon irradiated for 72 h at pH 9.0 in aerated water. ....75

**Figure 4.15:** Optical and SEM micrographs of areas showing different stages of progression to the formation of well-separated concentric crescent islands on a Cu coupon irradiated for 72 h at pH 9.0 in aerated water. ....77

**Figure 4.16:** Optical and SEM micrographs of the surface of a Cu coupon irradiated for 96 h at pH 9.0 in aerated water. ....78

**Figure 4.17:** SEM micrographs of the surfaces and the FIB-cut cross sections of Cu coupons corroded for different durations at pH 9.0 in aerated water in the presence of  $\gamma$ -radiation at  $3 \text{ kGy}\cdot\text{h}^{-1}$ . ....80

**Figure 5.1:** A  $50 \mu\text{L}$  water droplet on the surface of a circular copper coupon. ....83

**Figure 5.2:** Optical micrographs of the entire surfaces of circular Cu coupons corroded in 50  $\mu\text{L}$  aerated water droplets at initial pH 6.0 or pH 9.0 for different durations in the presence of  $\gamma$ -radiation at dose rate of  $2.8 \text{ kGy}\cdot\text{h}^{-1}$ . .....86

**Figure 5.3:** Concentration of copper species dissolved in the water droplets from the coupons whose optical micrographs are shown in **Figure 5.2**. .....87

**Figure 5.4:** Optical and SEM micrographs of areas of different corrosion progressions on a circular Cu coupon corroded for 36 h in a 50  $\mu\text{L}$  aerated water droplet at pH 9.0 in the presence of  $\gamma$ -radiation at a dose rate of  $2.8 \text{ kGy}\cdot\text{h}^{-1}$ . .....90

**Figure 5.5:** Optical and SEM micrographs of the area marked as Stage 1 on the optical micrograph shown in **Figure 5.4**. .....92

**Figure 5.6:** Optical micrographs of the central areas of the coupons corroded for different durations at pH 6.0 and 9.0 at a dose rate of  $2.8 \text{ kGy}\cdot\text{h}^{-1}$ . .....95

**Figure 5.7:** Optical micrographs of outer ring regions of the coupons corroded for different durations at pH 6.0 and 9.0 at a dose rate of  $2.8 \text{ kGy}\cdot\text{h}^{-1}$ . .....97

## List of Symbols and Abbreviations

A	Absorbance
CS	Carbon Steel
DGR	Deep Geologic Repository
$D_R$	Dose Rate
$\epsilon$	Extinction coefficient
$E^\circ$	Standard potential
EDX	Energy Dispersive X-ray
fcc	Face-Centered Cubic
FIB	Focused-Ion Beam
Gy	Gray
k	Rate Constant
$l$	Length
NWMO	Nuclear Waste Management Organization
PTFE	Polytetrafluoroethylene
$\rho$	Density
SEM	Scanning Electron Microscopy
SKB	Swedish Nuclear Waste Management Company
t	Time
UFC	Used Fuel Container
XPS	X-ray Photoelectron Spectroscopy
XRD	X-ray Diffraction Spectroscopy

## Chapter 1

### Introduction

#### 1.1 General Introduction

Many countries are exploring long-term disposal of used nuclear fuel in a deep geological repository (DGR) using a multiple-barrier system, with a key barrier being the used fuel container (UFC) [1-3]. Copper is an important component of many UFC designs. For example, a current Canadian UFC design consists of an inner vessel made of pressure-vessel-grade carbon steel (CS) for structural strength and an outer layer of integrally applied copper coating as an external corrosion barrier [4]. **Figure 1.1** shows the Mark II Used Fuel Container (UFC) design proposed by the Canadian Nuclear Waste Management Organization (NWMO). The container will house used fuel bundles from CANDU® reactors and be stored approximately 500 meters underground.

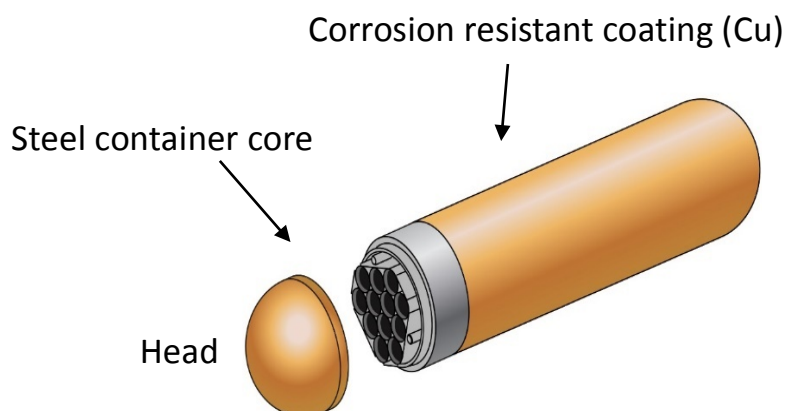
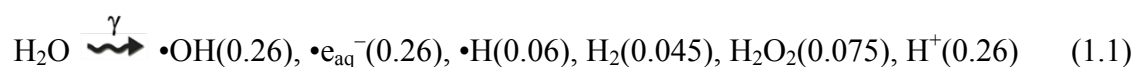


**Figure 1.1** An illustration of the Mark II used fuel container proposed by the NWMO.

In the DGR, the UFC and its corrosion environment will be exposed to a continuous flux of ionizing radiation (particularly  $\gamma$ -radiation) emitted from the decay of radionuclides in the used fuel [5]. The  $\gamma$ -radiation can interact with water condensed on the surface of the container, as well as humid air in the environment. Therefore, the effect of  $\gamma$ -radiation on copper corrosion must be evaluated to ensure that the copper layer provides sufficient corrosion protection that can last hundreds of years over the duration when the radiation level is not negligible [6].

Gamma-radiation decomposes water to yield chemically reactive species (both oxidizing and reducing). For  $\gamma$ -radiolysis of water at room temperature, the primary radiolysis products (formed within  $\sim 100$  ns following the absorption of  $\gamma$ -ray photons) and their yields per unit absorbed radiation energy (in brackets) in units of  $\mu\text{mol}\cdot\text{J}^{-1}$  are given below [7-10]:



In the presence of a continuous radiation flux these primary radiolysis products are continuously generated. As they are produced the primary radiolysis products also undergo chemical reactions with each other and water species ( $\text{H}^+$ ,  $\text{OH}^-$  and  $\text{H}_2\text{O}$ ) in the solution phase before they can diffuse to the copper surface and participate in redox reactions at the metal-solution interface. Consequently, the solution concentrations of radiolytic oxidants in the presence of a continuous radiation flux can be considered to be in pseudo-steady state for surface reactions [11-13]. Since water radiolysis products include both highly oxidizing and highly reducing species, they will determine the aqueous redox conditions of the water and influence the corrosion kinetics of metallic surfaces in radiation-exposed systems [14-18]. The oxidation (or corrosion) of copper in



oxygen-free environments is known to be very slow [19]. However, water radiolysis produces radicals and  $\text{H}_2\text{O}_2$  that can accelerate the oxidation of  $\text{Cu}^0(\text{m})$ . [20]

Predicting the corrosion rate over such an extended period, even without radiation present, is difficult because metal hydroxides/oxides may be formed and grow on the corroding surface which can influence corrosion behaviour. Corrosion is a complex process involving oxidation of metal, reduction of solution species and interfacial transfer of electrons and ions. The transfer of metal cations to the solution phase can induce changes in the physical and (electro-) chemical nature of the interfacial region. Concentration gradients of dissolved metal cations may develop near the surface. The hydrolysis of metal cations can lead to the formation of metal hydroxide/oxides that may be present as a gelatinous solid, crystalline grains or thin films. Changes in the surface layer, in turn, can strongly affect the metal oxidation rate and alter the corrosion pathway.

Copper corrosion has been studied extensively and ubiquitous formation of  $\text{Cu}_2\text{O}$  has been observed on copper under conditions that do not favour oxidation of  $\text{Cu}^0$ , such as anoxic or oxygen-free environments [21]. Nevertheless, there have been very few studies on the mechanism of  $\text{Cu}_2\text{O}$  formation and growth during copper corrosion or the effect of solution environments on  $\text{Cu}_2\text{O}$  growth and corrosion evolution. The difficulty in establishing the mechanism may arise from the very slow rate of copper oxidation and the ability of copper cations to complex with a variety of anions [22].

Cuprous oxide ( $\text{Cu}_2\text{O}$ ), being a stable p-type semiconductor with band gap energy of 2.0 eV [23-25], has many potential applications such as in solar energy conversion and optical devices [26-30], as an electrode material in lithium ion batteries [31], as a catalyst [32-36], and in gas sensors [37-39]. In these applications the size and morphology of the  $\text{Cu}_2\text{O}$  crystals are

important. To date, many methods have been developed for the synthesis of copper oxide nanoparticles which include chemical reduction [40], thermal decomposition [41], microwave heating [42], as well as solvothermal [43], and hydrothermal reduction [44-46].

The formation and growth of  $\text{Cu}_2\text{O}$  crystals by the hydrothermal/chemical reduction method of  $\text{Cu}^{2+}$  salts have been studied extensively. In these methods a cupric salt (a sulphate, nitrate, acetate or chloride) is reduced to  $\text{Cu}^+$  using a chemical reductant reducing agent (such as hydrazine, glucose, ascorbic acid or sodium borohydride) at a temperature typically higher than  $120^\circ\text{C}$ . With this method single  $\text{Cu}_2\text{O}$  crystals in a wide range of sizes and shapes (from cubes to truncated cubes, to truncated octahedral, to octahedral, to dodecahedral and spheres) have been synthesized using different combinations of the concentrations of chemical species (cupric salt, reductant and complexing agent), plus different temperatures, pHs and reaction times [47-54].

Unlike most crystals, single  $\text{Cu}_2\text{O}$  crystals are known to grow into several different polyhedron shapes [47-54]. The shape evolution of  $\text{Cu}_2\text{O}$  crystals from cubes, truncated cube, truncated octahedral, and octahedral is shown in **Figure 1.2**.

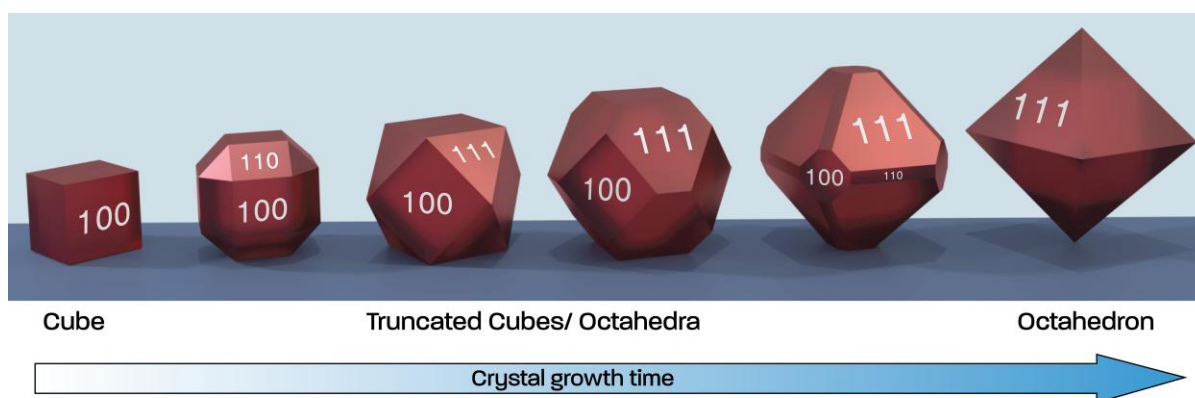


**Figure 1.2:** Shape evolution of  $\text{Cu}_2\text{O}$  crystals from cubes, truncated cube, truncated octahedral, and octahedral.

The polymorphic growth of  $\text{Cu}_2\text{O}$  crystals arises from different growth rates of different crystallographic planes [47]. The formation and growth of  $\text{Cu}_2\text{O}$  crystals is a complex process that involves many elementary steps. However, the existing experimental data do not provide sufficient information to fully understand how changing growth environments directly impact the elementary reaction steps involved in crystal formation and growth.

Whether the crystals are formed by hydrothermal chemical methods or by corrosion of copper metal, the formation and growth of  $\text{Cu}_2\text{O}$  crystals requires the production of the crystal constituent atom,  $\text{Cu}^{\text{I}}$ , nucleation and seed crystal formation, diffusion to and adsorption of  $\text{Cu}^{\text{I}}$  on the surface of a growing crystal, solvation and hydrolysis of copper ions, and  $\text{Cu}_2\text{O}$  lattice formation. Nevertheless, there are also key differences. During the corrosion of copper metal, the key crystal constituent atom  $\text{Cu}^{\text{I}}$  is produced by oxidation of  $\text{Cu}^0$  on the metal surface, which can also promote particle nucleation and seed crystal formation.

Because the  $\text{Cu}_2\text{O}$  crystal formation and growth involves multistep kinetic processes, changing any one of exposure parameters of the crystal growth medium (e.g., reductant concentration, pH, or temperature) can affect the rates of the elementary steps differently. Consequently, the kinetics of  $\text{Cu}_2\text{O}$  crystal growth during copper corrosion will have different dependences on solution environmental parameters. In order to develop a kinetic model that can predict the corrosion rate and its evolution as a function of environmental parameters, it is critical to understand and decouple the elementary processes involved in metal oxide formation and growth. A  $\text{Cu}_2\text{O}$  crystal growth mechanism that can explain how these different dependences arise can provide insight to copper corrosion and its evolution over long times.

## 1.2 Thesis Objectives and Outline

The main objective of this thesis is to investigate the time evolution of the size and morphology of  $\text{Cu}_2\text{O}$  crystals during water droplet corrosion of copper in the presence of a continuous flux of  $\gamma$ -radiation. The solution parameters studied include pH, aeration, and the ratio of water volume to surface area. Each solution parameter affects a certain kinetic step more effectively than other steps involved in the overall corrosion process. For example, the solution pH may be very important in controlling the rate of metal dissolution and the rate of hydrolysis that leads to the precipitation of metal hydroxides and eventually the formation of metal oxide, while the more oxidizing solution environment may increase the initial rate of metal oxidation. A mechanism for  $\text{Cu}_2\text{O}$  crystal growth that can explain the observed dependences of the size and morphology of the crystals by radiolytic oxidation of  $\text{Cu}^0(\text{m})$  is proposed.

The layout of the thesis and the work covered in this thesis are described below:

- Chapter 2 describes the materials background and literature review mainly focusing on the  $\text{Cu}_2\text{O}$  synthesis using chemical methods.
- Chapter 3 provides a description of the experimental techniques and procedures used in this thesis.
- Chapter 4 discusses the evolution of  $\text{Cu}_2\text{O}$  morphology on copper coupons corroded with 200  $\mu\text{L}$  water droplets exposed to gamma-radiation as a function of exposure time.
- Chapter 5 discusses the effect of pH on the evolution of  $\text{Cu}_2\text{O}$  morphology on copper coupons corroded with 50  $\mu\text{L}$  water droplets as a function of irradiation time.
- Chapter 6 describes the general mechanism involved in the  $\text{Cu}_2\text{O}$  formation and growth by radiolytic oxidation of  $\text{Cu}^0(\text{m})$  based on the evolution of surface morphology presented in Chapters 4 and 5.

### 1.3 References

1. NWMO, *Implementing adaptive phase management 2016-2020*, Toronto, Canada, 2015.
2. F. King, C. Lilja, *Corrosion Engineering, Science and Technology*, **2011**, 46(2), 153-158.
3. S. Necib, N. Diomidis, P. Keech, et al. *Swiss J Geosci*, **2017**, 110, 329-342.
4. C.H. Boyle, S.A. Meguid, *Nucl. Eng. Des.*, **2015**, 293, 403-412.
5. F. King, L. Ahonen, C. Taxen, U. Vuorinen, L. Werme, *Copper corrosion under expected conditions in a deep geologic repository*, SKB TR-01-23, 2001.
6. L. Werme, P. Sellin, N. Kjellbert, *Copper canisters for nuclear high level waste disposal*, SKB TR-82-26, SKB, Stockholm, 1992.
7. J.W.T. Spinks, R.J. Woods, *An Introduction to Radiation Chemistry*, 3<sup>rd</sup> Ed., Wiley-Interscience, New York, 1990.
8. Farhataziz, M.A.J. Rodgers, *Radiation Chemistry. Principles and Applications*. VCH Publishers, Inc. Weinheim, 1987.
9. J.H. O'Donnell, D.F. Sangster, *Principles of Radiation Chemistry*, American Elsevier Publishing Co. New York, 1970.
10. Z.D. Draganic, I.G. Draganic, *The Radiation Chemistry of Water*. Academic Press: New York, 1971.
11. J.C. Wren, ACS Symposium Series: Nuclear Energy and the Environment, **2010**, 1046, 271-295.
12. J.M. Joseph, B.S. Choi, P.A. Yakabuskie, J.C. Wren, *Radiat. Phys. Chem.*, **2008**, 77, 1009–1020.
13. P.A. Yakabuskie, J.M. Joseph, J.C. Wren, *Radiat. Phys. Chem.*, **2010**, 79, 777-785.
14. K. Daub, X. Zhang, J.J. Noel, J.C. Wren, *Corrosion Sci.*, **2011**, 53, 11-16.

15. K. Daub, X. Zhang, J.J. Noel and J.C. Wren, *Electrochimica Acta*, **2010**, *55*, 2767-2776.
16. M. Behazin, J.J. Noel, J.C. Wren, *Electrochimica Acta*, **2014**, *134*, 399-410.
17. M. Behazin, M.C. Beisinger, J.J. Noel, J.C. Wren, *Corrosion Sci.*, **2012**, *63*, 40-50.
18. Q.W. Knapp, J.C. Wren, *Electrochimica Acta*, **2012**, *80*, 90 - 99.
19. P. Szakálos, G. Hultquist, G. Wikmark, *Electrochem. Solid State Lett.*, **2007**, *10*, C63–C67.
20. A. Björkbacka, M. Yang, C. Gasparini, C. Leygraf, M. Jonsson, *Dalton Trans.*, **2015**, *44*, 16045-16051.
21. D. Landolt, A. Davenport, J. Payer and D. Shoesmith, *A Review of Materials and Corrosion Issues Regarding Canisters for Disposal of Spent Fuel and High-level Waste in Opalinus Clay*, NAGRA Technical Report 09-02, 2009.
22. M. Drogowska, L. Brossard, H. Menard, *Corrosion*, **1987**, *43*(9), 549-552.
23. B. Qin, Y. B. Zhao, H. Li, L. Qiu, Z. Fan. *Chin. J. Catal.*, **2015**, *36*, 1321–1325.
24. P. Curie, *Bull. Soc. Fr. Mineral Cristallogr.*, **1885**, *8*, 145–150.
25. G. Wulff, *Z. Kristallogr.*, **1901**, *34*, 449–530.
26. A. Mittiga, E. Salza, F. Sarto, M. Tucci, R. Vasanthi, *Appl. Phys. Lett.*, **2006**, *88*, 163502.
27. R.N. Briskman, *Sol. Energy Mater. Sol. Cells.*, **1992**, *27*, 361–368.
28. L.C. Olsen, F.W. Addis, W. Miller, *Sol. Cells*, **1982**, *7*, 247–279.
29. C.C. Hu, J.N. Nian, H. Teng, *Sol. Energy Mater. Sol. Cells*, **2008**, *92*, 1071.
30. S.S. Jeong, A. Mittiga, E. Salza, A. Masci, S. Passerini, *Electrochim. Acta*, **2008**, *53*, 2226.
31. C. Xu, X. Wang, L.C. Yang, Y.P. Wu, *J. Solid State Chem.*, **2009**, *182*, 2486.

32. J. Ramirez-Ortiz, T. Ogura, J. Medina-Valtierra, S.E. Acosta-Ortiz, P. Bosch, J.A. de los Reyes, V.H. Lara, *Appl. Surf. Sci.*, **2001**, *174*, 177–184.
33. H.M. Yang, J. Ouyang, A.D. Tang, Y. Xiao, X.W. Li, X.D. Dong, Y.M. Yu, *Mater. Res. Bull.*, **2006**, *41*, 1310–1318.
34. W.L. Bao, Y.Y. Liu, X. Lv and W.X. Oian, *Org. Lett.*, **2008**, *10*, 3899.
35. H.Z. Bao, W.H. Zhang, Q. Hua, Z.Q. Jiang, J.L. Yang and W.X. Huang, *Angew. Chem. Int. Ed.*, **2011**, *50*, 12294.
36. W.T. Yao, S.H. Yu, Y. Zhou, J. Jiang, Q.S. Wu, L. Zhang. J. Jiang, *J. Phys. Chem. B*, **2005**, *109*, 14011.
37. S.T. Shishiyanu, T.S. Shishiyanu, O.I. Lupan, *Sens. Actuators B*, **2006**, *113*, 468–476.
38. J.T. Zhang, J.F. Liu, Q. Peng, X. Wang, Y.D. Li, *Chem. Mater.*, **2006**, *18*, 867.
39. H.G. Zhang, Q.S. Zhu, Y. Zhang, Y. Wang, L. Zhao, B. Yu, *Adv. Funct. Mater.*, **2007**, *17*, 2766.
40. S. Chen, J.M. Sommers, *J Phys Chem B*, **2001**, *105*, 8816–8820.
41. X. Liu, B. Geng, Q. Dua, J. Ma, X. Liu, *Mater Sci Eng A*, **2007**, *448*, 7–14.
42. H. Zhu, C. Zhang, Y. Yin, *Nanotechnology*, **2005**, *16*, 3079–3084.
43. T. Xin-ling, R. Ling, S. Ling-na, T. Wei-guo, C. Min-hua, H. Chang-wen, *Chem. Res Chinese U*, **2006**, *22*(5), 547-551.
44. H. Shi, K. Yu, Y. Wang, Q. Wang, Z. Zhu, *Appl. Phys. A: Mater. Sci. Process.*, **2012**, *108*(3), 709–717.
45. X. Zou, H. Fan, Y. Tian, et al., *Dalton Trans.*, **2015**, *44*(17), 7811–7821.
46. K. Self, W. Zhou, *Cryst. Growth Des.*, **2016**, *16*, 5377-5384.
47. K. Chen, C.Sun, S. Song, D. Xue, *Cryst. Eng. Comm.* **2014**, *16*, 5257.

48. C.H. Kuo, M.H. Huang, *Nano today*, **2010**, 2, 106.
49. L. Huang, F. Peng, H. Yu, H. Wang, *Mater. Res. Bull.*, **2008**, 43(11), 3047-3053.
50. J. Zhu, Y. Wang, X. Wang, X. Yang, L. Lu, *Powder Technol.*, **2008**, 181(3), 249-254.
51. J. Zhu, H. Bi, Y. Wang, X. Wang, X. Yang, L. Lu. *Mater. Lett.*, **2008**, 62(14), 2081-2083.
52. P. He, X. Shen, H. Gao, *J. Colloid Interface Sci.*, **2005**, 284(2), 510-515.
53. Y. Sui, W. Fu, H. Yang, Y. Zeng, Y. Zhang, Q. Zhao, Y. Li, X. Zhou, Y. Leng, M. Li, G. Zou, *Cryst. Growth Des.*, **2010**, 10(1), 99-108.
54. Y. Shang, L. Guo, *Adv. Sci.*, **2015**, 2, 1-22.



## Chapter 2

### Background and Literature Review

#### 2.1 Materials Background

##### 2.1.1 Copper Metal

Copper is a metal with good electrical and thermal conductivity, corrosion resistance, and it is ductile and easy to alloy with other metals. It is widely used in integrated circuits, pipes, and wires [1-4]. The electronic configuration of copper is  $[\text{Ar}]3d^{10}4s^1$ . Due to the filled 3d orbitals, the interatomic interactions in copper are dominated by the 4s electrons through metallic bonding. That is, metallic bonds in copper lack covalent character and are very weak, which makes copper ductile. The single 4s electron is also responsible for physical properties of copper such as its electrical conductivity and reddish colour. Copper metal has a face-centred cubic (fcc) crystal structure and generally comes in polycrystalline grains [5]. The average size of the  $\text{Cu}^0$  grains of the copper coupons used in this study is rather large, on the order of 100  $\mu\text{m}$ . Different crystal planes of  $\text{Cu}^0$  are known to have different electrochemical reactivity.

##### 2.1.2 Electrochemical Potentials of Copper Redox Reactions

Copper exists in three oxidation states: 0, +1 and +2. The standard electrochemical reduction potentials for redox reactions between different copper species are shown in **Figure 2.1** [6]. These redox potentials show that dissolved cupric ion ( $\text{Cu}^{2+}_{(\text{aq})}$ ) can be reduced to dissolved cuprous ion ( $\text{Cu}^{+}_{(\text{aq})}$ ) with a mild reductant. However, once formed,  $\text{Cu}^{+}_{(\text{aq})}$  will continue to be reduced to  $\text{Cu}^0$  in the same reducing environment, although the second reduction

step may be slower. Similarly, the oxidation of  $\text{Cu}^0$  to form of  $\text{Cu}^+$  can continue to the formation of  $\text{Cu}^{2+}_{(\text{aq})}$ . The redox reactions between other cupric and cuprous species (e.g.,  $\text{Cu}_2\text{O}$ ,  $\text{Cu}(\text{OH})_2$ ) have similar potential relationships [6]. The thermodynamics of copper redox reactions indicate that the kinetics of the reactions will play an important role in controlling the production of cuprous oxide ( $\text{Cu}_2\text{O}$ ) by reduction of  $\text{Cu}^{\text{II}}$  species or by oxidation of  $\text{Cu}^0$ .

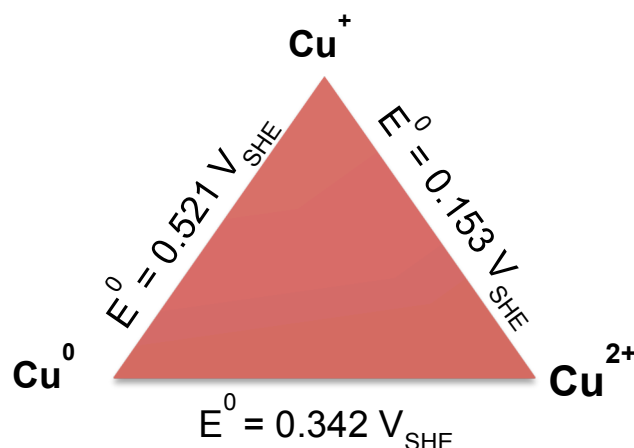


**Figure 2.1:** Redox reactions between  $\text{Cu}^0$ ,  $\text{Cu}^+$  and  $\text{Cu}^{2+}$  and their standard redox potentials.

### 2.1.3 Solubilities of Copper Ions

Metal-oxide crystal growth from dissolved metal cations depends strongly on the solubility of the metal cation in the crystal growth medium (i.e., solution) because of its influence on the adsorption kinetics of the cation on the planes of the growing crystal. The solubility of a metal cation can vary by orders of magnitude, depending on the oxidation state of the metal and the pH of the solution. The  $\text{Cu}^{\text{I}}$  and  $\text{Cu}^{\text{II}}$  have very different solubility limits in water free of complexing anions [7-9]. The solubilities of  $\text{Cu}^{\text{I}}$  and  $\text{Cu}^{\text{II}}$  as a function of pH in water reported in [9] are replotted in **Figure 2.2**. The solubility of  $\text{Cu}^{\text{I}}$  is about two orders of magnitude lower than that of  $\text{Cu}^{\text{II}}$  at pH 5.0 but the difference decreases with increasing pH.

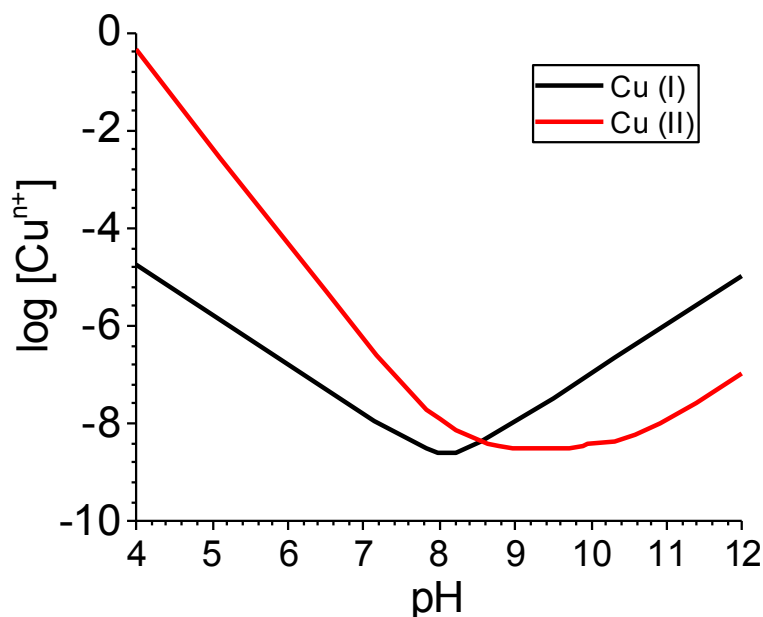


**Figure 2.2:** The solubility of  $\text{Cu}^+$  and  $\text{Cu}^{2+}$  as a function of pH. [9]

#### 2.1.4 Crystal Structures of Copper Oxides

Both cuprous oxide ( $\text{Cu}_2\text{O}$ ) and cupric oxide ( $\text{CuO}$ ) are stable under ambient conditions. They differ in colour, crystal structure and semiconducting properties.  $\text{CuO}$  is a black colored solid and has a monoclinic structure where the Cu atom is coordinated to 4 O atoms. For cupric oxide the lattice constants are:  $a = 4.68 \text{ \AA}$ ,  $b = 3.42 \text{ \AA}$ ,  $c = 5.14 \text{ \AA}$ ,  $\alpha = \gamma = 90^\circ$ , and  $\beta = 99.6^\circ$  [10]. **Figure 2.3** shows the face-centred cubic (fcc) structure of Cu, the cubic structure of  $\text{Cu}_2\text{O}$  and the monoclinic structure of  $\text{CuO}$ .

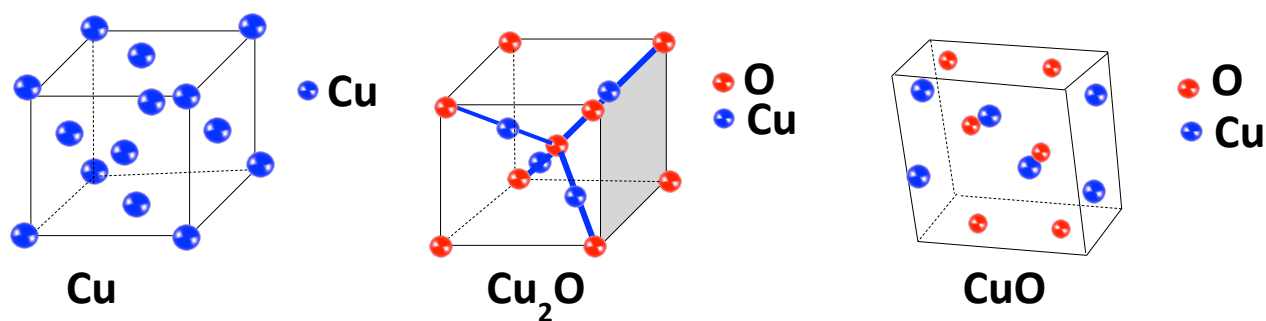


**Figure 2.3:** The fcc structure of Cu, cubic structure of  $\text{Cu}_2\text{O}$  and monoclinic structure of CuO.

Copper (II) hydroxide ( $\text{Cu}(\text{OH})_2$ ) is a blue solid and has an orthorhombic crystal structure. The unit cell parameters are  $a = 2.951 \text{ \AA}$ ,  $b = 10.592 \text{ \AA}$ ,  $c = 5.257 \text{ \AA}$  and  $\alpha = \beta = \gamma = 90^\circ$ . [11]

Cuprous oxide is a red coloured solid. The unit cell structure of  $\text{Cu}_2\text{O}$  crystal is cubic, consisting of four Cu atoms and eight O atoms where each Cu atom is coordinated with two O atoms and each O atom is coordinated with four Cu atoms. The unit cell structure of  $\text{Cu}_2\text{O}$  can be envisioned as two inter-penetrating cubic lattices consisting of face-centred cubic (fcc) packing of Cu atoms and body-centered cubic (bcc) packing of O atoms as shown in **Figure 2.4** [1-4]. The interatomic distances between Cu – O and Cu – Cu are  $1.84 \text{ \AA}$  and  $3.02 \text{ \AA}$ , respectively. [10] The unit cell parameters are  $a = b = c = 4.27 \text{ \AA}$  and  $\alpha = \beta = \gamma = 90^\circ$ . Some of the crystallographic planes with their Miller indices are shown in **Figure 2.5**.

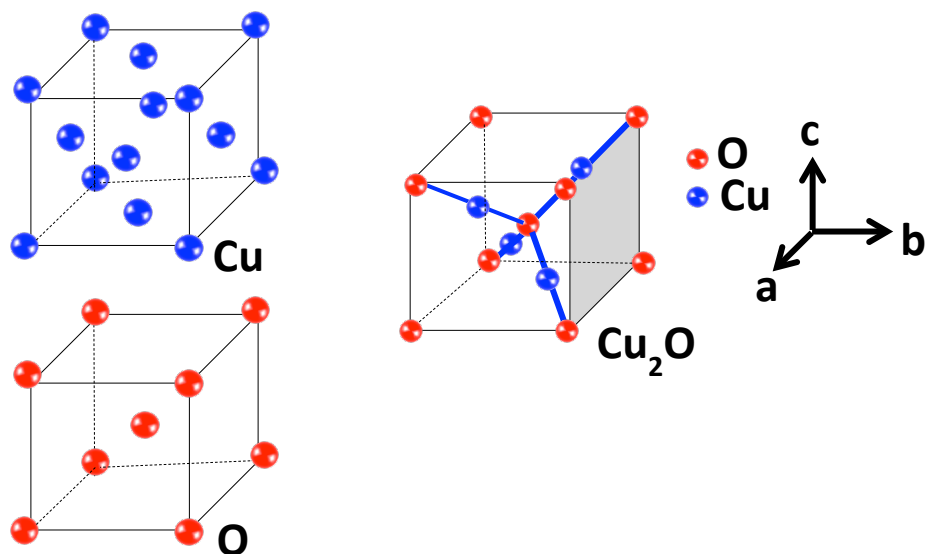


**Figure 2.4:** The fcc packing of Cu atoms, bcc packing of O atoms and cubic structure of  $\text{Cu}_2\text{O}$ . The schematics were adapted from Chen et al. and redrawn for this thesis. [12]

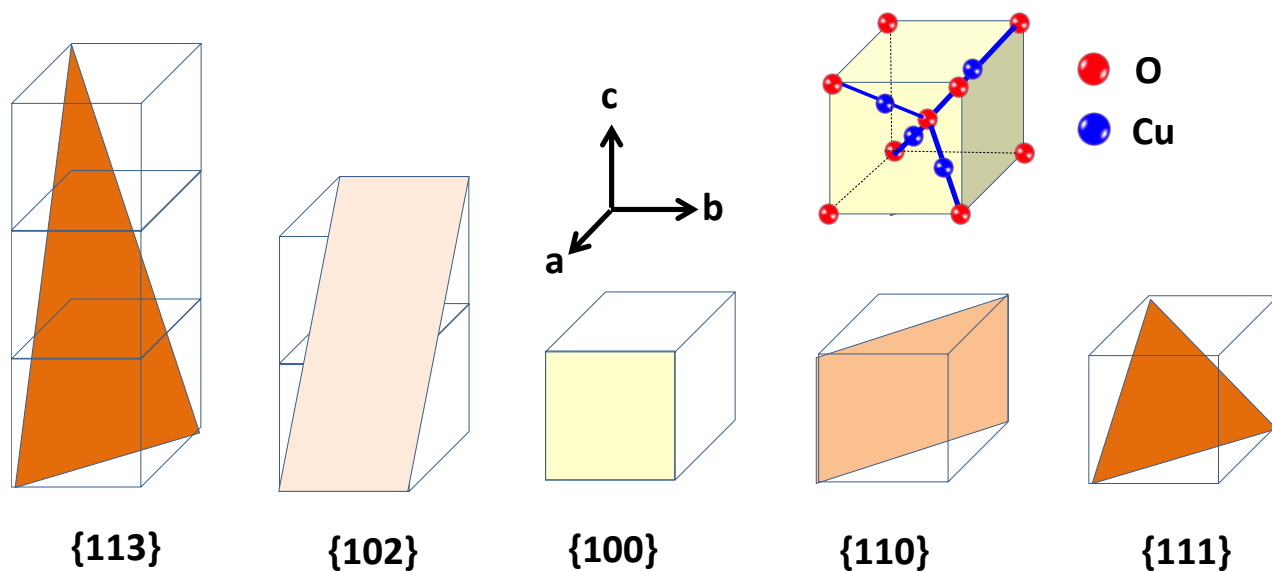


**Figure 2.5:** Schematic of the  $\text{Cu}_2\text{O}$  crystal unit cell structure and some crystallographic planes. The unit cell consists of fcc packing of Cu atoms and bcc packing of O atoms. For the Cu atoms, only those that are coordinated with the body-centred O atom are shown for clarity.

### 2.1.5 Evolution of Crystal Morphology During Its Growth

Following nucleation and seed crystal formation, a salt (or ionic) crystal grows by incorporating the crystal constituent atoms adsorbed on the crystal surfaces into the growing lattice structure. Because of different lattice bond strengths and surface energies of the crystal atoms on different planes, different crystal planes grow at different rates, and the crystal shape changes as it grows. Facets with higher surface energy initially grow the fastest, but diminish with time, while facets with lower surface energies are more thermodynamically stable and grow slowly but are preserved in the final structure or morphology of the  $\text{Cu}_2\text{O}$  crystals.

The thermodynamics of  $\text{Cu}_2\text{O}$  single crystal growth calculated from the surface and lattice energies indicate that the rate of growth perpendicular to a crystal plane is fastest to slowest in the following order of crystallographic planes [12]:

$$\{113\} > \{102\} > \{100\} > \{110\} > \{111\}$$

A crystallographic plane with a faster growth rate diminishes faster during crystal growth. Hence, single  $\text{Cu}_2\text{O}$  crystals initially grow in cubes having 6 facets of  $\{100\}$  planes, but slowly change their shapes from cubes to truncated cubes and truncated octahedrons (different combinations of  $\{100\}$ ,  $\{110\}$  and  $\{111\}$ ) and eventually to octahedrons having 8 facets of the thermodynamically most stable  $\{111\}$  planes, **Figure 2.6**. The  $\text{Cu}_2\text{O}$  crystals with only  $\{113\}$  and/or  $\{102\}$  facets are very unstable and have not been observed.

Depending on the number density of single crystals they may aggregate to form single- or multiple twin crystals early which then continue to grow into shapes ranging from bipyramid, decahedron, icosahedron, etc. [12] In the presence of additives that preferably adsorb on a certain set of crystallographic planes, the growth rate of the crystal is affected resulting in the modification of the final crystal shape [13].

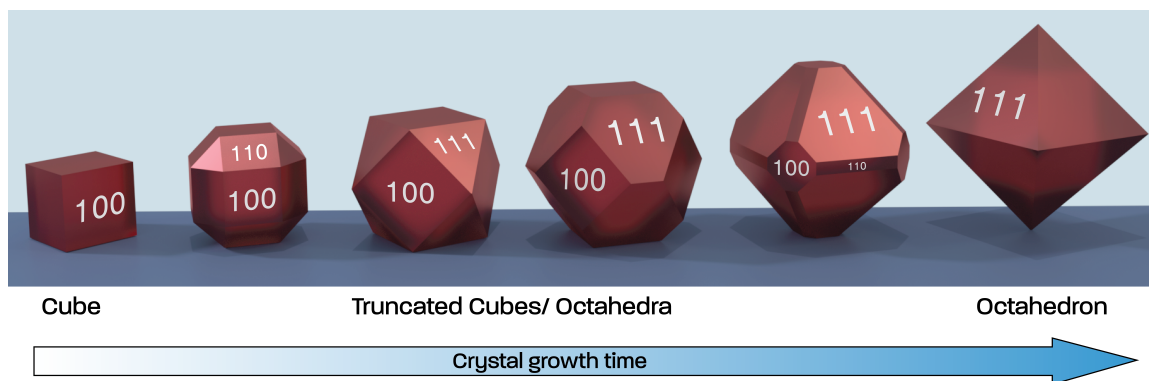


**Figure 2.6:** Schematic showing the different shapes of single  $\text{Cu}_2\text{O}$  crystals with increasing growth time.

### 2.1.6 Synthesis of $\text{Cu}_2\text{O}$ Crystals of Different Morphologies

Cuprous oxide ( $\text{Cu}_2\text{O}$ ) is a stable p-type semiconductor with band gap energy of 2.0 eV [14-16] and is a promising material for several applications, such as solar energy conversion [17-21], gas sensing [22-24], catalysis [25-29], electrode materials for lithium ion batteries [30] etc. The performance of  $\text{Cu}_2\text{O}$  for these applications is mostly determined by the size, morphology and the microstructure of the oxide. For example, different crystal structures of  $\text{Cu}_2\text{O}$  exhibit different photocatalytic properties. A study by Liu et al. showed that the photocatalytic reactivity can be varied by tuning the ratios of different crystal facets of metal oxide semiconductors [31]. The study found that crystals with exposed  $\{110\}$  facets exhibited increased photocatalytic reactivity for the photodegradation of methyl orange due to a high number density of surface atoms on the  $\{110\}$  plane. [31] Huang et al. have discussed the dependence of the electrical behaviour on the morphology of the  $\text{Cu}_2\text{O}$  crystals [32]. The study found that  $\text{Cu}_2\text{O}$  octahedra exhibited higher electrochemical capacity than spherical structures. [32]

Cuprous oxide crystals up to tens of  $\mu\text{m}$  in size have been synthesized in variety polyhedron shapes, including cubes [33], octahedra [34], rhombic dodecahedra [35-37], thin

films [38-39], nanorod arrays [40], nanospheres or nanocubes [41-43], and hollow crystals [44-45].

Various synthesis techniques have been employed such as solution reduction [46-48], hydrothermal/solvothermal synthesis [49-51], electrochemical deposition [52-57], chemical vapour deposition [58], microwave heating [59], and sonochemical methods [60-61]. Among these methods, solution reduction methods are commonly used due to their low cost, high efficiency, and potential for large-scale production.

In a solution reduction method, a cupric salt (a sulphate, nitrate, acetate or chloride) is reduced to  $\text{Cu}_2\text{O}$  using a chemical reductant reducing agent at a temperature typically higher than  $120\text{ }^\circ\text{C}$ . An organic capping agent or stabilizing agent is often used to selectively adsorb on a specific plane(s) to yield a desired crystal structure. Common reducing agents used in the chemical synthesis include glucose [62], ascorbic acid [63], hydroxylamine [64], hydrazine [65], formic acid [66], ethylenediaminetetraacetic acid (EDTA) [67], dimethylformamide (DMF) [68] glutamic acid [69], sodium borohydride [70], diethanolamine (DEA) [71], polyethylene glycol [72], and acetic acid [73]. Common organic capping agents are polyvinylpyrrolidone (PVP) [74], cetyltrimethylammonium bromide (CTAB) [75], sodium dodecyl sulfate (SDS) [76], and polyethylene glycol (PEG) [77]. Inorganic ions used to control the morphology of  $\text{Cu}_2\text{O}$  crystals include  $\text{OH}^-$ ,  $\text{SO}_4^{2-}$ , and  $\text{Cl}^-$  [56,79-81]. Although organic surfactants have proven to be powerful tools in shaping the morphology of  $\text{Cu}_2\text{O}$  crystals, they can strongly bind to the crystals, requiring a special removal step and complicating the synthetic process.

With the solution method  $\text{Cu}_2\text{O}$  crystals in a wide range of sizes (from nanometers to micrometers) and shapes (from cubes to truncated cubes and octahedra, to octahedra, to dodecahedra and spheres) have been synthesized using different combinations of the



concentrations of chemical species (cupric salt, reductant and complexing agent), plus different temperatures, pH, and reaction times [12, 46-51].

Huang et al. synthesized  $\text{Cu}_2\text{O}$  crystals at room temperature by reduction of  $\text{CuCl}_2$  with hydroxylamine hydrochloride ( $\text{NH}_2\text{OH}\cdot\text{HCl}$ ) [76]. Sodium dodecyl sulphate (SDS) was used as a surfactant and sodium hydroxide ( $\text{NaOH}$ ) was used as a reagent to control pH. By increasing the amount of hydroxylamine hydrochloride added to the reaction solution,  $\text{Cu}_2\text{O}$  crystals with shapes ranging from cubic, “face-raised” cubic, truncated octahedral to rhombic dodecahedra were synthesized. The study showed that the reducing agent can control the rate of reduction from  $\text{Cu}^{2+}$  to  $\text{Cu}^+$ , and affect the crystal morphology of  $\text{Cu}_2\text{O}$  observed in the final product.

Sui et al. reported the shape evolution of  $\text{Cu}_2\text{O}$  crystals from cubic to octahedral and spheres by using different amounts of polyvinylpyrrolidone (PVP) [82]. The synthesis was performed at 80 °C using a copper-citrate complex and glucose as a reducing agent. The shape evolution is attributed to the selective interaction of PVP with the  $\{111\}$  facets during the reaction. Zhang et al. [83] also reported on synthesis of  $\text{Cu}_2\text{O}$  with shapes ranging from cubic to octahedral using ascorbic as a reducing agent and PVP as a capping agent.

Song et al. used  $\text{Cl}^-$  to control the morphology of  $\text{Cu}_2\text{O}$  crystals. The  $\text{Cl}^-$  ions selectively adsorbed on  $\{110\}$  crystal facets and it was reported that the  $\text{Cu}_2\text{O}$  crystals formed in  $\text{CuCl}_2$ -citrus-glucose- $\text{NaCl}$  solutions change from octahedra, to truncated octahedra, to rhombic dodecahedra when the  $\text{NaCl}$  concentration was increased from 3.4 mM to 6.8 mM [81].

Siegfried and Choi [55] also reported the synthesis of  $\text{Cu}_2\text{O}$  crystals with different morphologies from octahedral, to truncated octahedral, to cubooctahedral, to truncated cubic, to cubic by varying the  $\text{Cl}^-$  concentration with sodium dodecyl sulphate (SDS). The shape evolution was initially thought to be due to the pH effect since  $\text{HCl}$  was used, but the same effect

was not observed by using  $\text{HNO}_3$ . However, by using  $\text{NaCl}$  the same morphology was observed; this confirmed that  $\text{Cl}^-$  and not the pH change was responsible for the change in morphology.

Siegfried and Choi also studied the effect of an additive on stabilizing certain crystal planes by adding the additive at different times of crystal growth [56]. When  $\text{NH}_4^+$  ions were added to the reaction solution after cubic  $\text{Cu}_2\text{O}$  crystals were formed, the  $\{110\}$  and  $\{111\}$  planes started to grow. As the crystals grew for longer times the area of the  $\{110\}$  plane decreased and the area of the  $\{111\}$  plane increased and the shape of the crystals was eventually transformed to octahedral. When the  $\text{NH}_4^+$  ions were added before the  $\text{Cu}_2\text{O}$  nucleated, the  $\{100\}$  planes grew out of existence before forming crystals with well-defined facets since the  $\text{NH}_4^+$  ions selectively decrease the growth rate along the  $\{111\}$  plane.

Some chemicals (such as diethanolamine (DEA)) can act as both a reductant and a capping agent. A study by Chen et al. found that the shape of  $\text{Cu}_2\text{O}$  crystals changed from truncated octahedral to truncated cubic with increasing DEA concentration [84].

In summary, due to different growth rates of the crystallographic planes, the size and morphology of a  $\text{Cu}_2\text{O}$  crystal that grows changes with time. The faster the rate of net production of  $\text{Cu}^{\text{I}}_{(\text{ad})}$  on the growing crystal is, the larger the  $\text{Cu}_2\text{O}$  crystal will grow over the same growth period. However, as the crystal grows, the surface area of the slower growth plane increases while that of the faster growth plane decreases, favouring the slower growth planes as the crystal grows. The rate of overall growth of  $\text{Cu}_2\text{O}$  will decrease with time. In the solution reduction method different sizes and shapes of single  $\text{Cu}_2\text{O}$  crystals have been synthesized using different combinations of kinetic parameters, such as chemical additives (reducing and complexing agents), reaction temperature, time, and concentration of precursors.

## 2.2 Radiation Chemistry

### 2.2.1 Radiation Chemistry and Photochemistry

Radiation chemistry involves the study of the chemical effects produced in a system when exposed to high-energy ionizing radiation. Ionizing radiation includes high-energy charged particles (e.g.,  $\alpha$  and  $\beta$  particles), fast electrons from accelerators, and electromagnetic radiation (e.g., x-rays and  $\gamma$ -rays).

Radiation chemistry differs significantly from photochemistry, which employs low energy infrared (IR) and ultraviolet (UV) sources. These lower energy sources in the eV energy range can induce vibrational or electronic excitations in the target molecules. These types of interactions involve a photon interacting with a single molecule and the frequency of the radiation can be tuned to interact with a selected molecular group. Due to the high specificity and singular interaction involved, photochemistry of solutions may be described as a solute-oriented process in which the bulk solution remains unaffected by the presence of the radiation. In contrast, high energy ionizing radiation (keV-MeV range) excites or ionizes a large number of molecules indiscriminately along the radiation track. Since all molecules are equally likely to interact with the radiation, the bulk solution is most affected. As a result, radiation chemistry of solutions can be described as a solvent-oriented process [85].

### 2.2.2 Types of Ionizing Radiation

As described above, ionizing radiation includes high-energy charged particles (e.g.  $\alpha$  and  $\beta$  particles), fast electrons from accelerators and electromagnetic radiation (e.g. x- and  $\gamma$ -rays). Ionizing radiation transfers its energy to an interacting medium mainly by colliding non-discriminately with the electrons bound to atoms and molecules in the medium. Due to their

high kinetic energy, each radiation particle undergoes a series of collisions before it thermalizes. Radiation energy moving through a medium leaves a radiation track.

Alpha-particles, the nuclei of helium atoms, are emitted by radioactive nuclei and have discrete energies that are characteristic of the radioisotope decay process. The  $\alpha$ -particles interact with electrons within a medium, primarily through inelastic collisions, along the radiation path. Due to their large size in comparison with the electrons they perturb, only small amounts of energy are lost with each collision, and the large  $\alpha$ -particles are not easily deflected from their paths. However, the large collision cross section with electrons prevents these particles from penetrating deeply into the medium, resulting in a very dense collection of excited and ionized particles along a short stretch of the radiation track [85-88].

Beta-particles are high-energy electrons or positrons that interact through inelastic collisions with electrons along their paths and have a large penetration depth. Since  $\beta$ -particles share the same mass as the electrons with which they interact, the particles can lose up to half of their energy with each collision, and can be deflected through a large angle.  $\beta$ -particles can interact with additional electrons to lose their remaining energy. Also, the electrons with which the  $\beta$ -particles interacted can propagate the electron ejection process, but with reduced efficiency through each cascade. Therefore, these particles create a low-density collection of ions or excited molecules along their radiation tracks [85-88].

Gamma rays are electromagnetic radiation with energies in the range of 40 keV to 4 MeV and have the largest penetration depth of the ionizing radiation types described thus far [85]. A given gamma radiation source emits  $\gamma$ -rays of specific energies. Gamma-rays transfer most of their energy by Compton scattering if their energy exceeds 0.01 MeV [85]. Compton scattering is a phenomenon in which the  $\gamma$ -ray interaction with matter causes electron ejection from the

molecule and the resulting  $\gamma$ -ray photon emerges with a reduced energy. The most probable Compton scatterings are either near 100% energy transfer or near 0% energy transfer. Due to the low probability of the inelastic Compton scattering, the penetration depth of  $\gamma$ -radiation is large relative to all other radiation forms [85]. Each ejected electron from these high-energy collisions acts similarly to a  $\beta$ -particle and prolongs the collision effect by transferring its kinetic energy.

### 2.2.3 Interaction of Radiation with Matter

The processes occurring in the interacting medium following the absorption of radiation energy can be schematically represented as shown in **Figure 2.7** for water. The interaction of a radiation particle (or high energy electron from the Compton scattering for a  $\gamma$ -photon) with matter transfers energy in a series of small steps to produce secondary electrons with a kinetic energy of the order of 100 eV. These secondary “hot” electrons can ionize or excite nearby solvent molecules within a very short time scale ( $\sim 10^{-14}$  s) creating a cluster or spur of 2-3 ion pairs (electrons and solvent cations) or excited molecules [85,89].

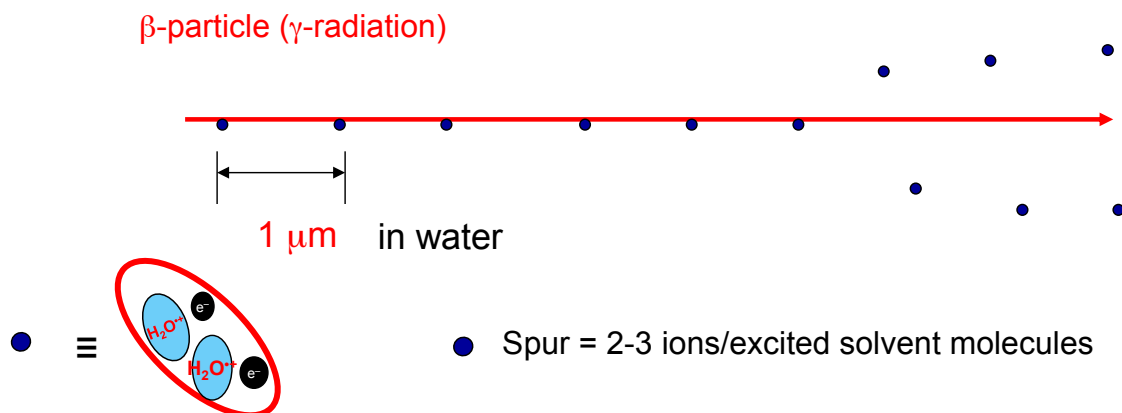


**Figure 2.7:** The radiation track of a fast electron (spur size not to scale).

The cascade of events that occur when a radiation photon deposits energy in water is shown in **Figure 2.8**. The ‘hot’ electrons, cations, and excited species formed initially in the spur can dissociate, or react with a nearby water molecule, to form radicals within the solvent cages. Some of the radicals produced in the spur combine to form molecular products such as H<sub>2</sub> and H<sub>2</sub>O<sub>2</sub> [85-89]. Ion pairs or excited molecules formed in a spur may have sufficient kinetic energy to overcome the Coulombic force of the original counter ion, and the spur expands. A large fraction of the ion pairs and radical pairs formed within spurs undergo geminate recombination to form stable products, but a small fraction can escape to become “free” ions or radicals. The escape probability depends on the dielectric constant of the medium, the larger the dielectric constant of the medium the higher the escape probability. Due to the high dielectric constant of water, the radiolysis of water can produce many free radicals.

The chemical yields of species after  $\sim 10^{-7}$  s, when homogeneous distribution along the track is achieved, are referred to as the primary radiolysis yields and those species are called primary radiolysis products.

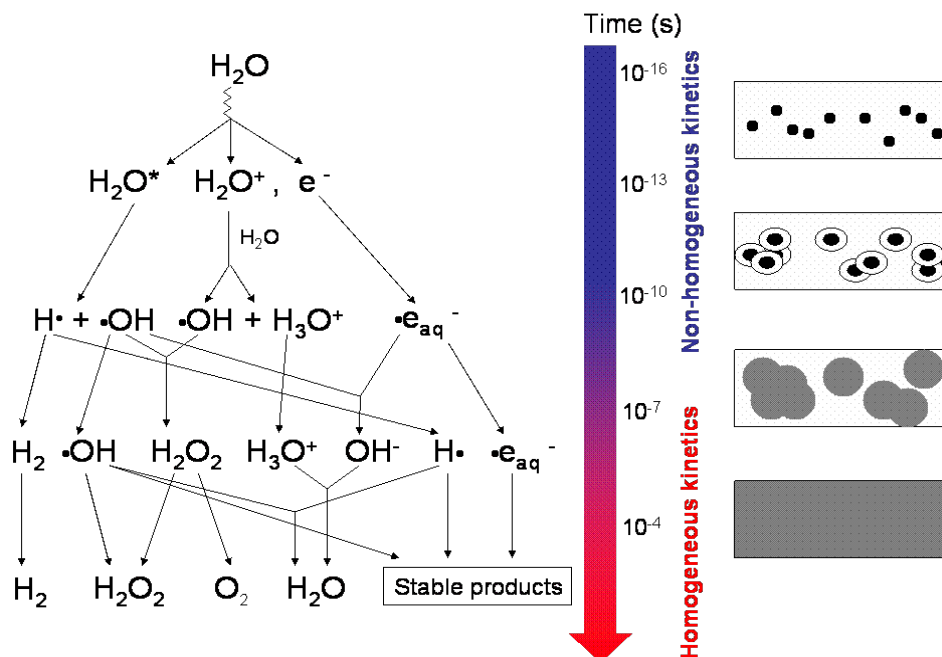
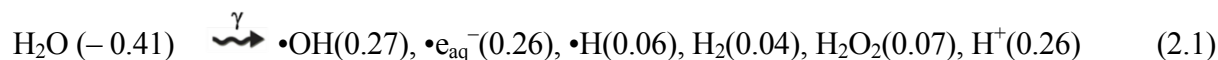


**Figure 2.8:** Schematic of the cascade of events that occur in irradiated water to generate the primary radiolysis products.

The yields of the primary radiolysis products per absorbed energy are referred to as G-values, in units of molecules/100 eV or  $\mu\text{mol}\cdot\text{J}^{-1}$ . The G-values for water radiolysis products have been reported in the literature for different radiation sources and have been determined by pulse radiolysis experiments [85-89].



Following their formation, the primary radiolysis products will react normally with any other species that is present. The reactants will include other radiolysis products, water and its dissociation products, and other additives. This creates an environment that is often referred to as the chemical stage. The products of reactions of the primary radiolysis products with each other are referred to as secondary radiolysis products. This includes molecular species like  $O_2^-$

and  $\text{H}_2\text{O}_2$ . The bulk-phase chemical reactions of the radiolysis products with any other species present at low concentrations (less than  $0.01 \text{ mol}\cdot\text{dm}^{-3}$ ) proceed on a much slower time scale than the events in a radiation spur, and thus do not have a significant impact on the primary yields. The kinetics of interfacial reactions or materials corrosion, which typically have large activation energies and proceed fairly slowly, are determined by the concentrations of the chemically reactive species present in the chemical stage and not by the primary radiolysis yields.

If there is a continuous flux of ionizing radiation, water molecules will continuously decompose at a rate determined by the radiation dose rate ( $\text{J}/\text{kg}/\text{s}$  or  $\text{Gy}/\text{s}$ ) and G-value. This provides a continuous source of reactive species that feed the chemical stage as shown in **Figure 2.9**.

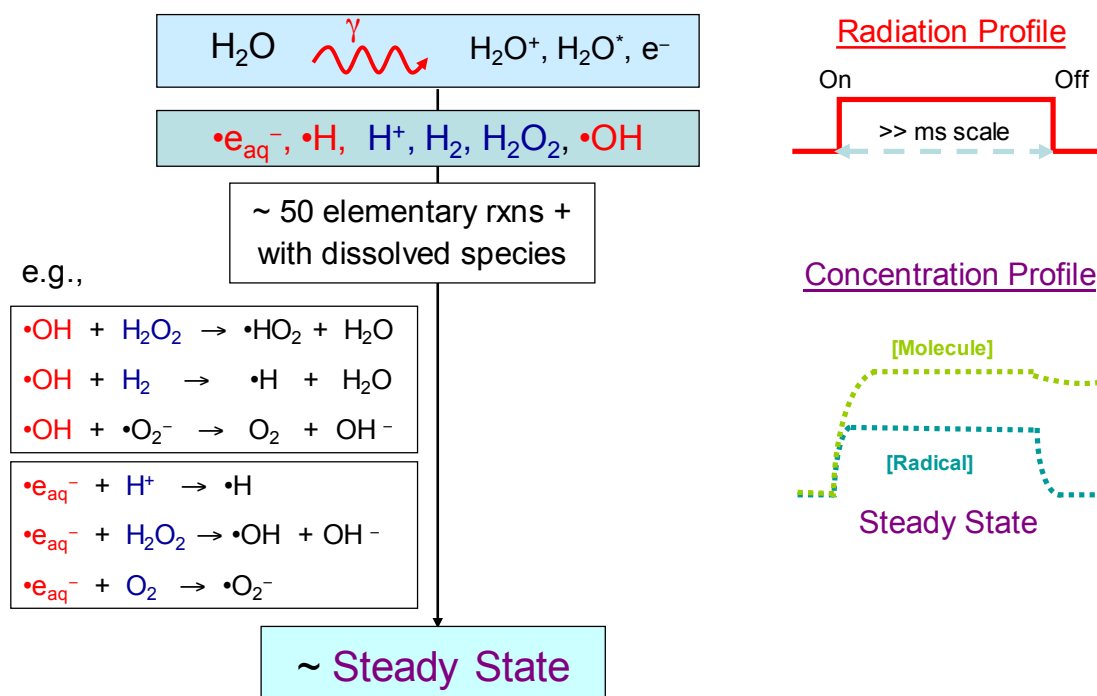


**Figure 2.9:** Schematic of water radiolysis reaction mechanism under long-term (>ms) continuous irradiation.



In such a system, the concentrations of the reactive primary and secondary radiolysis products will eventually reach a steady-state concentration when the rates of production and loss become equal [89-92]. The presence of species that preferentially react with any of the radiolysis products can alter the steady-state concentrations. Due to the high chemical reactivity of radicals, some dissolved impurities, particularly metal ions with more than one stable oxidation state, even at very low concentrations, can have a significant impact on the concentrations of the radiolysis products and can significantly alter the solution redox state.

#### 2.2.4 Time Evolution of Radiolysis Product Concentration

Pure water radiolysis model calculations were used to determine the concentration of the water radiolysis products present as a function of irradiation time. Because many of the radiolysis products are radical species that are reactive and short-lived, the model is useful for predicting the concentrations of radiolysis products after a given time. Irradiation of aerated water can produce nitric acid but the production of nitric acid at 25 °C is small and was not considered in these calculations. The model takes into account the  $\gamma$ -ray dose rate, the G-values, the rate constants of the many possible reactions, as well as variable experimental parameters, such as pH and temperature. The water radiolysis model used in this study has been previously validated against experimental data under a wide range of conditions [93-95].

**Figure 2.10** (a) shows the concentrations of water radiolysis products formed as a function of irradiation time in deaerated water for pH 6.0 and pH 9.0 at 25 °C. Initially, at pH 6.0, the concentrations of  $\bullet e_{aq}^-$  and  $\bullet H$  increase with irradiation time. There is a slight decrease in  $\bullet e_{aq}^-$  and  $\bullet H$  concentrations as the  $O_2$  concentration starts to increase around  $10^{-3}$  s, and finally

$\bullet e_{aq}^-$  and  $\bullet H$  reach a steady state. The final concentrations of the molecular products  $H_2O_2$  and  $H_2$  are lower compared to the aerated case at pH 6.0, **Figure 2.10** (b).

For pH 9.0 under deaerated conditions, the concentrations of  $\bullet e_{aq}^-$  and  $\bullet H$  first increase with irradiation time and then decrease steadily as the concentration of  $O_2$  increases continuously throughout the duration of the experiment. The concentrations of the molecular products increase linearly with irradiation time and are higher than those seen at pH 6.0.

**Figure 2.10** (b) shows the concentrations of water radiolysis products formed as a function of irradiation time in aerated water for pH 6.0 and pH 9.0 at 25 °C. At pH 6.0, the  $O_2$  present in the water inhibits the production of  $\bullet e_{aq}^-$  (through reaction 2.2) and the concentration of these species remains nearly constant, and quite low throughout the irradiation period.



The concentrations of  $\bullet O_2^-$ ,  $\bullet HO_2$  and  $\bullet OH$  increase linearly with time before reaching steady-state concentrations. For the molecular products, such as  $H_2O_2$  and  $H_2$ , the concentrations also increase linearly with irradiation time. Aerated conditions favour the formation of molecular products such as  $H_2O_2$  and  $H_2$ . At pH 9.0, the formation of  $\bullet e_{aq}^-$  is again inhibited by the presence  $O_2$ , while the concentrations of  $H_2O_2$ ,  $H_2$ , and  $\bullet O_2^-$  increase with increasing irradiation time.

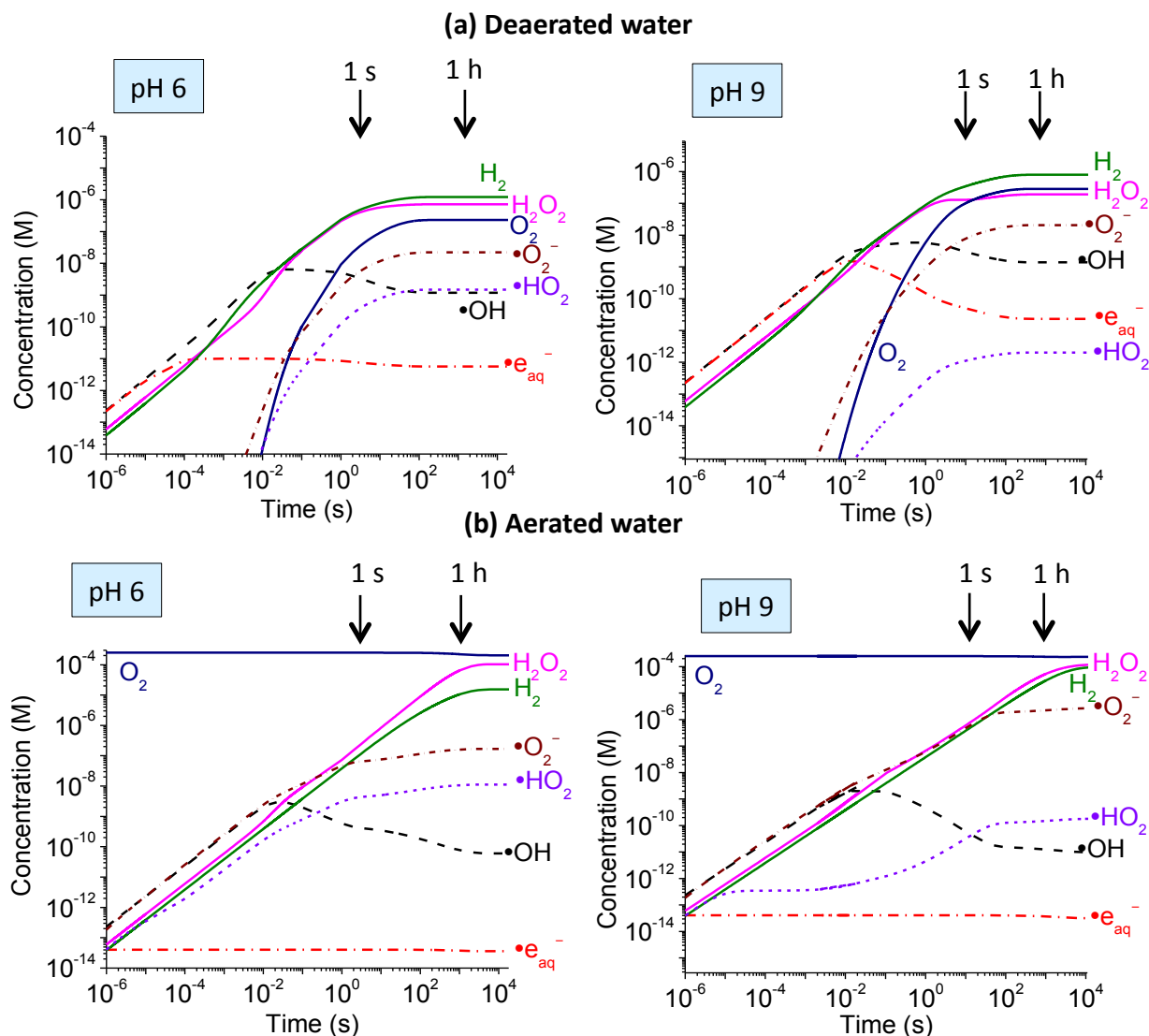


**Figure 2.10:** Calculated concentrations of radiolysis products formed as a function of irradiation time during irradiation of (a) deaerated water and (b) aerated water for pH 6.0 and 9.0 at 25 °C, and a dose rate of  $3.0 \text{ kGy}\cdot\text{h}^{-1}$ .

Nitric acid ( $\text{HNO}_3$ ) production becomes important in humid air environments exposed to radiation. A humid air radiolysis model (HARM) has been developed in the Wren group to calculate the production rate of  $\text{HNO}_3$  by humid air radiolysis.  $\text{HNO}_3$  formed in the gas phase can adsorb into condensed water that is in contact with the humid air. This adsorption leads to a

decrease in pH, and increases the concentration of nitrate ( $\text{NO}_3^-$ ) in the water droplet. Since  $\text{NO}_3^-$  is a potential oxidant for copper, the production of  $\text{NO}_x$  species by humid air radiolysis is an important factor in calculating the corrosion rate of copper metal.

**Figure 2.11** shows the humid air radiolysis modeling results. The concentrations of nitrogen species produced by irradiation of 0% RH, 10% RH, and 85% RH air were calculated at 25 °C and a dose rate of  $3 \text{ kGy}\cdot\text{h}^{-1}$ . The calculations show that for the irradiation of 0% RH air, nitric acid production is negligible. The main products are  $\text{O}_3$  and  $\text{NO}_x$  species ( $\text{N}_2\text{O}_5$ ,  $\text{NO}_2$ ,  $\text{N}_2\text{O}$ ). However, in humid air,  $\text{HNO}_3$  production becomes significant. At 10% RH, the  $\text{HNO}_3$  production increases with increasing irradiation time. At 85% RH,  $\text{HNO}_3$  is the main oxidizing species. The modeling results show that  $\text{H}_2\text{O}_2$  is also produced during humid air radiolysis.

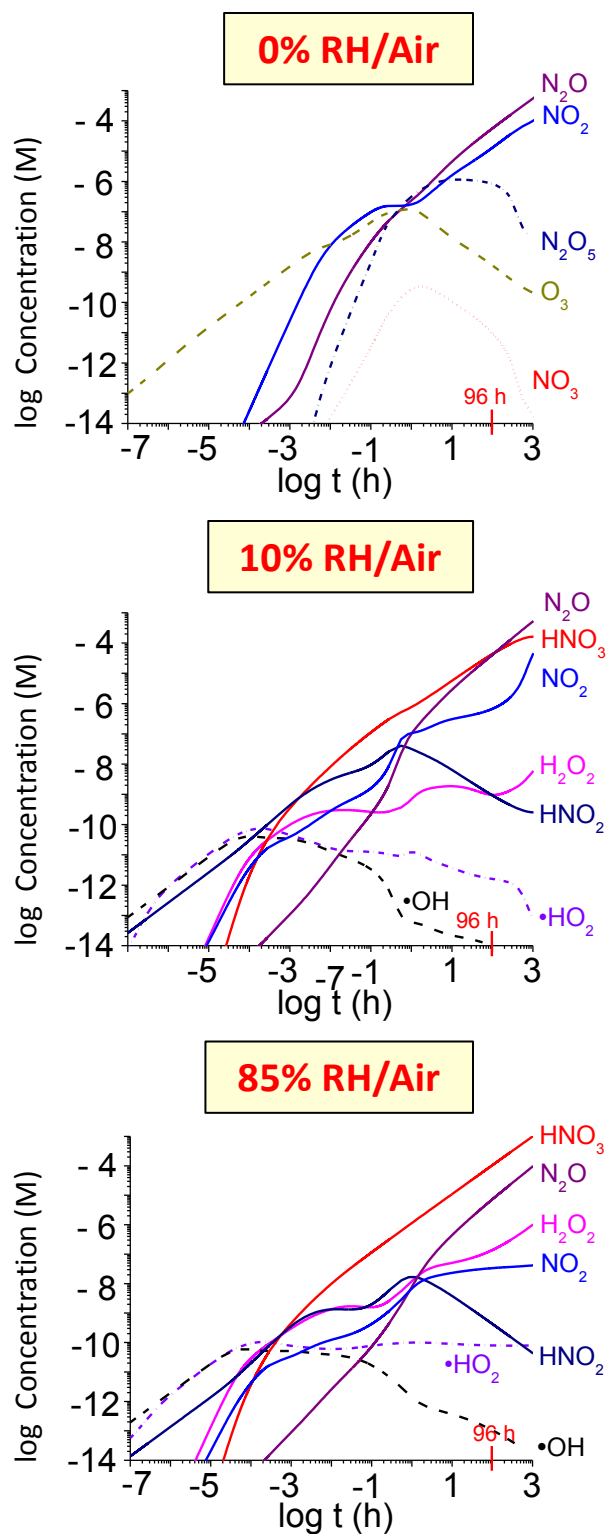


**Figure 2.11:** Concentrations of nitrogen species calculated using the humid air radiolysis model for radiolysis of 0% RH, 10% RH, and 85% RH air at 25 °C and a dose rate of 3 kGy·h<sup>-1</sup>.

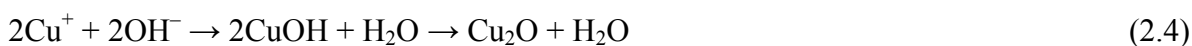
### 2.2.5 Radiation Induced Nanoparticle Formation

Radiolysis is a promising new technique that can be applied to the synthesis of metal oxide nanoparticles and thin films to provide superior control of the size and morphology of the particles. Gamma-radiation decomposes water to yield a range of redox active species (reaction 2.1) and the chemical yields per unit energy input of the radical species are very high, and cannot be obtained by other thermal processes. Because  $\gamma$ -radiation penetrates deeply in water, it generates a uniform homogeneous distribution of radiolysis products that, in turn, leads to the simultaneous generation of homogeneously distributed nucleation sites. This leads to the formation of nanoparticles with a narrow, uniform size distribution. Radiation-induced nanoparticle formation is also considered a cleaner technique since the addition of chemical additives or stabilizers is not required for particle formation or size control. Another unique feature of  $\gamma$ -radiolysis is the production of redox active species consisting only of H and O atoms. Important consequences of this are the generation of redox active species without altering the metal-cation solubility in the solution and without unwanted waste products. This eliminates the need for other chemical agents that can interfere with the particle growth kinetics.

Wren et al. have reported the mechanism of  $\gamma$ -radiation-induced formation and growth of metal-oxide nanoparticles from initially dissolved metal cations in aqueous solutions ( $\gamma$ -FeOOH from  $\text{Fe}^{2+}$ ,  $\text{Co}_3\text{O}_4$  from  $\text{Co}^{2+}$ , and  $\text{Cr}_2\text{O}_3$  from  $\text{Cr}^{6+}$ ) [96-101]. In these studies the strong oxidizing power of  $\bullet\text{OH}$  and  $\text{H}_2\text{O}_2$  or the strong reducing power of  $\bullet\text{e}_{\text{aq}}^-$ , and the difference in the solubility of the oxidation products are utilized for the metal oxide nanoparticle formation. Depending on the equilibrium potential of the redox reaction involved, either the oxidizing or reducing water radiolysis products are utilized for the generation of nucleation sites and particle growth. In the case of chromium oxide, the reducing power of  $\bullet\text{e}_{\text{aq}}^-$  is used whereas for the iron

and cobalt systems the oxidizing powers of  $\bullet\text{OH}$  and  $\text{H}_2\text{O}_2$  are employed. Each of these systems takes advantage of a large difference in the solubility of the initially dissolved metal ions and their oxidized or reduced relatives.

The synthesis of  $\text{Cu}_2\text{O}$  nanocrystals by ionizing radiation ( $\gamma$  and e-beams) has been reported [102-105]. The synthesis of the crystals was achieved by irradiating a  $\text{CuSO}_4$  solution in the presence of chemical scavengers (such as isopropyl alcohol) and chemical stabilizers (such as polyvinyl alcohol). In this method the hydrated electron, which is a powerful reducing agent, reduces  $\text{Cu}^{2+}$  to  $\text{Cu}^+$ . In the presence of  $\text{OH}^-$ ,  $\text{CuOH}$ , which is an unstable complex will form and then decompose into  $\text{Cu}_2\text{O}$  as shown in reaction 2.3 and 2.4.



The size and morphology of the particles formed depends on the pH of the initial solution as well as the irradiation dose. The solubility of the cuprous and cupric ions is pH dependent, and the difference in their solubility can be utilized to form colloidal particles and thereby generate nucleation sites for particle growth under irradiation.

Although extensive work has been carried out to control the morphology of isolated particles, fewer studies have focussed on controlling the size and morphology of particles grown on a metal substrate. The radiation technique provides a convenient way of optimizing the morphology of particles formed on a metal substrate, which can be directly used as electrode material. Most of the recent photoelectrochemical devices such as solar cells, photoelectrochemical cells, fuel cells, and batteries use semiconducting and metallic electrodes as their main components.

### 2.3 References

1. K. Chen, D. Xue, *Cuprous Oxide: The Only Example that Features Nanoscience and Nanotechnology*, Encyclopedia of Semiconductor Nanotechnology, Volume 2, American Scientific Publishers, 2012.
2. M. Yin, C. Wu, Y. Lou, C. Burda, J. T. Koberstein, Y. Zhu, S. O'Brien, *J. Am. Chem. Soc.*, **2005**, *127*, 9506.
3. M.B. Gawande, A. Goswami, F.X. Felpin, T. Asefa, X. Huang, R. Silva, X. Zou, R. Zboril, R.S. Varma, *Chem. Rev.*, **2016**, *116*, 3722-2811.
4. K. Chen, D. Xue, *Appl. Sci. Converg. Technol.*, **2014**, *23*(1), 14-26.
5. J.R. Davis, *Copper and copper alloys*, ASM International, Materials Park, Ohio, 2001.
6. A.J. Brad, L.R. Faulkner, *Electrochemical Methods: Fundamentals and Applications*, 2<sup>nd</sup> Ed, John Wiley & Sons Inc., New York, 2001.
7. C.F. Baes, R.E. Mesmer, *Hydrolysis of Cations*, 2<sup>nd</sup> Ed, Krieger Pub. Co., Malabar, Florida, 1986.
8. D.A. Palmer, *J Solution Chem.*, **2011**, *40*, 1067-1093
9. D.A. Palmer, P. Benezeth, *Solubility of copper oxides in water and steam*, 14<sup>th</sup> International Conference on the Properties of Water and Steam in Kyoto, 2004, 492-296.
10. J. Ghijsen, L.H. Tjeng, J. Van Elp, H. Eskes, J. Westerink, G.A. Sawatzky, M.T. Czyzyk, *Phys. Rev. B*, **1988**, *38*, 11322.
11. H.R. Oswald, A. Reller, H.W. Schmalle, E. Dubler, *Acta Cryst. C*, **1990**, *46*, 2279-2284.
12. K. Chen, C. Sun, S. Song, D. Xue, *Cryst. Eng. Comm.*, **2014**, *16*, 5257-5267.
13. K.S. Choi, *Dalton. Trans.*, **2008**, 5432-5438.
14. B. Qin, Y.B. Zhao, H. Li, L. Qiu, Z. Fan, *Chin. J. Catal.* **2015**, *36*, 1321–1325.



15. P. Curie, *Bull. Soc. Fr. Mineral Cristallogr.* **1885**, 8, 145–150.
16. G. Wulff, *Z. Kristallogr.* **1901**, 34, 449–530.
17. A. Mittiga, E. Salza, F. Sarto, M. Tucci, R. Vasanthi, Heterojunction, *Appl. Phys. Lett.* **2006**, 88, 163502.
18. R.N. Briskman, *Sol. Energy Mater. Sol. Cells*, **1992**, 27, 361–368.
19. L.C. Olsen, F.W. Addis, W. Miller, *Sol. Cells*, **1982**, 7, 247–279.
20. C.C. Hu, J.N. Nian, H. Teng, *Sol. Energy Mater. Sol. Cells*, **2008**, 92, 1071.
21. S.S. Jeong, A. Mittiga, E. Salza, A. Masci, S. Passerini, *Electrochim. Acta*, **2008**, 53, 2226.
22. S.T. Shishiyanu, T.S. Shishiyanu, O.I. Lupan, *Sens. Actuators. B.*, **2006**, 113, 468–476.
23. J.T. Zhang, J.F. Liu, Q. Peng, X. Wang, Y.D. Li, *Chem. Mater.*, **2006**, 18, 867.
24. H.G. Zhang, Q.S. Zhu, Y. Zhang, Y. Wang, L. Zhao, B. Yu, *Adv. Funct. Mater.*, **2007**, 17, 2766.
25. J. Ramirez-Ortiz, T. Ogura, J. Medina-Valtierra, S.E. Acosta-Ortiz, P. Bosch, J.A. De Los Reyes, V.H. Lara, *Appl. Surf. Sci.*, **2001**, 174, 177–184.
26. H.M. Yang, J. Ouyang, A.D. Tang, Y. Xiao, X.W. Li, X.D. Dong, Y.M. Yu, *Mater. Res. Bull.*, **2006**, 41, 1310–1318.
27. W.L. Bao, Y.Y. Liu, X. Lv, W.X. Oian, *Org. Lett.*, **2008**, 10, 3899.
28. H.Z. Bao, W.H. Zhang, Q. Hua, Z.Q. Jiang, J.L. Yang, W.X. Huang, *Angew. Chem. Int. Ed.*, **2011**, 50, 12294.
29. W.T. Yao, S.H. Yu, Y. Zhou, J. Jiang, Q. S. Wu, L. Zhang, J. Jiang, *J. Phys. Chem. B.*, **2005**, 109, 14011.
30. C. Xu, X. Wang, L.C. Yang, Y.P. Wu, *J. Solid State Chem.*, **2009**, 182, 2486.

31. G. Liu, J.C. Yu, G.Q. Lu, H.M. Cheng, *Chem. Commun.*, **2011**, 47, 6763-6783.
32. X. Zhang, Z. Cui, *Mater. Sci. Eng. B.*, **2009**, 162(2), 82–86.
33. L.F. Gou, C.J. Murphy, *Nano Lett.*, **2003**, 3, 231.
34. H.L. Xu, W.Z. Wang, W. Zhu, *J. Phys. Chem. B.*, **2006**, 110, 13829.
35. X.D. Liang, L. Gao, S.W. Yang and J. Sun, *Adv. Mater.*, **2009**, 21, 2068.
36. K.X. Yao, X.M. Yin, T.H. Wang and H.C. Zeng, *J. Am. Chem. Soc.*, **2010**, 132, 6131.
37. W.C. Huang, L.-M. Lyu, Y.-C. Yang and M. H. Huang, *J. Am. Chem. Soc.*, **2012**, 134, 1261.
38. Z.G. Zang, A. Nakamura, J. Temmyo, *Opt. Express*, **2013**, 21, 11448–11456.
39. M. Shahmiri, N.A. Ibrahim, F. Shayesteh, N. Asim, N. Motallebi, *J. Mater. Res.*, **2013**, 28, 3109– 3118.
40. Y.S. Chen, C.H. Liao, Y.L. Chueh, C.C. Lai, L.Y. Chen, A.K. Chu, C.T. Kuo, H.C. Wang, *Opt. Mater*, **2014**, 4, 1473–1483.
41. H. Guo, L.X. Liu, T.T. Li, W.W. Chen, J.J. Liu, Y.Y. Guo, Y.C Guo, *Nanoscale*, **2014**, 6, 5491– 5497.
42. R. Khan, M. Vaseem, L.W. Jang, J.H. Yun, Y.B. Hahn, I.H. Lee, *J. Alloys Compd.*, **2014**, 609, 211–214.
43. C.F. Gou, C.J. Murphy, *Nano Lett.*, **2003**, 3, 231–234.
44. L.L. Feng, C.L. Zhang, G. Gao, D.X. Cui, *Nanoscale Res. Lett.*, **2012**, 7, 276.
45. C. Lu, L. Qi, J. Yang, X. Wang, D. Zhang, J. Xie, J. Ma, *Adv. Mater.*, **2005**, 17, 2562–2567.
46. L. Tang, J. Lv, S. Sun, et al., *New J. Chem.*, **2014**, 38(10), 4656–4660.
47. H.Xu, W. Wang, W. Zhu, *J. Phys. Chem. B.*, **2006**, 110(28), 13829–13834.

48. D.F. Zhang, H. Zhang, L. Guo, K. Zheng, X.D. Han, Z. Zhang, *J. Mater. Chem.*, **2009**, *19*(29), 5220–5225.
49. H. Shi, K. Yu, Y. Wang, Q. Wang, Z. Zhu, *Appl. Phys. A: Mater. Sci. Process.*, **2012**, *108*(3), 709–717.
50. X. Zou, H. Fan, Y. Tian, et al., *Dalton Trans.*, **2015**, *44*(17), 7811–7821.
51. K. Self, W. Zhou, *Cryst. Growth Des.* **2016**, *16*, 5377–5384.
52. M.A. Shoeib, O.E. Abdelsalam, M.G. Khafagi, R.E. Hammam, *Adv. Powder Technol.*, **2012**, *23*(3), 298–304.
53. Y. Zhai, H. Fan, Q. Li, et al., *Appl. Surf. Sci.*, **2012**, *258*(7), 3232–3236.
54. M.J. Siegfried, K.S. Choi, *Angew. Chem., Int. Ed.* **2005**, *44*, 3218–3223.
55. M.J. Siegfried, K.S. Choi, *Adv. Mater.* **2004**, *16*, 1743–1746.
56. M.J. Siegfried, K.S. Choi, *J. Am. Chem. Soc.* **2006**, *128*, 10356–10357.
57. W.T. Yao, S.H. Yu, Y. Zhou, J. Jiang, Q.S. Wu, L. Zhang, J. Jiang, *J. Phys. Chem. B.*, **2005**, *109*, 14011–14016.
58. M. D. Susman, Y. Feldman, A. Vaskevich, I. Rubinstein, *ACS Nano*, **2014**, *8*(1), 162–174.
59. H. Zhu, C. Zhang, Y. Yin, *Nanotechnology*, **2005**, *16*, 3079.
60. R.V. Kumar, Y. Mastai, Y. Diamant, A. Gedanken, *J. Mater. Chem.*, **2001**, *11*, 1209–1213.
61. H. Zheng, Q. Li, C. Yang, H. Lin, M. Nie, L. Qin, Y. Li, *RSc. Adv.*, **2015**, *5*, 59349–59353.
62. S. Jiao, L. Xu, K. Jiang, D. Xu, *Adv. Mater.*, **2006**, *18*(9), 1174–1177.
63. H. Xu, W. Wang, *Angew. Chem. Int. Ed.*, **2007**, *46*(9), 1489–1492.

64. C.H. Kuo, M.H. Huang, *J. Am. Chem. Soc.*, **2008**, *130*(38), 12815–12820.
65. W. Wang, G. Wang, X. Wang, Y. Zhan, Y. Liu, C. Zheng, *Adv. Mater.*, **2002**, *14*(1), 67–69.
66. Y. Chang, H.C. Zeng, *Cryst. Growth Des.*, **2004**, *4*(2), 273–278.
67. J. Xu, D. Xue, *Acta Materialia*, **2007**, *55*(7), 2397–2406.
68. Y. Chang, J.J. Teo, H.C. Zeng, *Langmuir*, **2005**, *21*(3), 1074–1079.
69. H. Zhang, Q. Zhu, Y. Zhang, Y. Wang, L. Zhao, B. Yu, *Adv. Fun. Mater.*, **2007**, *17*(15), 2766–2771.
70. J. Zhang, J. Liu, Q. Peng, X. Wang, Y. Li, *Chem. Mater.*, **2006**, *18*(4), 867–971.
71. K. Chen, D. Xue. *Appl. Sci. Conver. Technol.*, **2014**, *23*(1), 14-26.
72. L. Zhang, H. Wang, *ACS Nano*, **2011**, *5*, 3257-3267.
73. S. Arshadi-Rastabi, J. Moghaddam, M.R. Eskandarian, *Ind. Eng. Chem. Res.*, **2015**, *22*, 34-40.
74. R.V. Kumar, Y. Mastai, Y. Diamant, A. Gedanken, *J. Mater. Chem.*, **2001**, *11*, 1209–1213.
75. Y. Sui, W. Fu, H. Yang, Y. Zeng, Y. Zhang, Q. Zhao, Y. Li, X. Zhou, Y. Leng, M. Li, *Cryst. Growth Des.*, **2009**, *10*(1), 99–108.
76. X. Zhang, Z. Cui, *Mater. Sci. Eng. B.*, **2009**, *162*(2), 82–86.
77. W.C. Huang, L.M. Lyu, Y.C. Yang, M.H. Huang. *J. Am. Chem. Soc.*, **2012**, *134*, 1261-1267.
78. L. Gou, C.J. Murphy, *J. Mater. Chem.*, **2004**, *14*, 735-738.
79. L. Mei, Y. Chao, W. Cheng, *Cryst. Eng. Comm.*, **2012**, *14*(24), 8454–8461.
80. M.H. Kim, B. Lim, E.P. Lee, Y. Xia, *J. Mater. Chem.*, **2008**, *18*(34), 4069–4073.

81. K. Song, D. Xue, K. Chen, S. Sun, *Cryst. Eng. Comm.*, **2014**, *16*, 5257-5267.
82. Y. Sui, W. Fu, H. Yang, Y. Zeng, Y. Zhang, Q. Zhao, Y. Li, X. Zhou, Y. Leng, M. Li, G. Zou, *Cryst. Growth. Des.*, **2010**, *10*(1) 99-108.
83. D. Zhang, H. Zhang, L. Guo, K. Zheng, X.D. Han, Z. Zhang, *J. Mater. Chem.*, **2009**, *19*, 5220-5225.
84. K. Chen, Y. Si, D. Xue. *Nanosci. Nanotechnol. Lett.* **2011**, *3*, 423.
85. J.W.T. Spinks, R.J. Woods, *An Introduction to Radiation Chemistry*, 3<sup>rd</sup> Ed., Wiley-Interscience, New York, 1990.
86. Farhataaziz, M.A.J. Rodgers, *Radiation Chemistry. Principles and Applications*. VCH Publishers, Inc. Weinheim, 1987.
87. J.H. O'Donnell, D.F. Sangster, *Principles of Radiation Chemistry*, American Elsevier Publishing Co. New York, 1970.
88. Z.D. Draganic, I.G. Draganic, *The Radiation Chemistry of Water*. Academic Press: New York, 1971.
89. J.C. Wren, *ACS Symposium Series: Nuclear Energy and the Environment*, **2010**, *1046*, 271-295.
90. J.M. Joseph, B.S. Choi, P.A. Yakabuskie, J.C. Wren, *Radiat. Phys. Chem.*, **2008**, *77*, 1009–1020.
91. P.A. Yakabuskie, J.M. Joseph, J.C. Wren, *Radiat. Phys. Chem.*, **2010**, *79*, 777-785.
92. P.A. Yakabuskie, J.M. Joseph, C.R. Stuart, J.C. Wren, *J. Phys. Chem. A.*, **2011**, *115*, 4270–4278.
93. J.M. Joseph, B.S. Choi, P.A. Yakabuskie, J.C. Wren, *Radiat. Phys. Chem.*, **2008**, *77*, 1009.

94. P.A. Yakabuskie, J.M. Joseph, J.C. Wren, *Radiat. Phys. Chem.*, **2010**, *79*, 777.
95. J.C. Wren, G.A. Glowa, *Radiat. Phys. Chem.*, **2000**, *58*, 341-356.
96. P.A. Yakabuskie, J.M. Joseph, P. Keech, G.A. Botton, D.A. Guzanos, J.C. Wren, *Phys. Chem. Chem. Phys.*, **2011**, *13*, 7198-7206.
97. T.I. Sutherland, C.J. Sparks, J.M. Joseph, Z. Wang, G. Whitaker, T.K. Sham and J.C. Wren, *Phys. Chem. Chem. Phys.*, **2017**, *19*, 695.
98. L.M. Alrehaily, J.M. Joseph, J.C. Wren, *J. Phys. Chem. C*, **2015**, *119*(28), 16321.
99. L.M. Alrehaily, J.M. Joseph, J.C. Wren, *Phys. Chem. Chem. Phys.*, **2015**, *17*, 24138.
100. L.M. Alrehaily, J.M. Joseph, M.C. Biesinger, D.A. Guzonas, J.C. Wren, *Phys. Chem. Chem. Phys.*, **2013**, *15*, 1014.
101. L.M. Alrehaily, J.M. Joseph, A.Y. Musa, D.A. Guzonas, J.C. Wren, *Phys. Chem. Chem. Phys.*, **2013**, *15*, 98.
102. Q.D. Chen, X.H. Shen, H.C. Gao. *J. Colloid Interf. Sci.*, **2007**, *312*, 272–278.
103. P. He X.H. Shen, H.C. Gao. *J. Colloid Interf. Sci.*, **2005**, *284*, 510–515.
104. W.F. Miao, H.R. Liu, Z.G. Zhang, et al. *Solid State Sci.*, **2008**, *10*, 1322–1326.
105. L. Xiangfengw, Z. Ruimin, S. Xiaohai, Z. Jianqiang, *Nucl. Sci. Tech.*, **2010**, *21*, 146-151.

## Chapter 3

### Experimental Principles and Procedures

This chapter describes the surface analysis techniques, chemical analysis techniques and the general experimental procedures used in this thesis project. Any additional experimental details and information that are specific to each chapter are provided in the appropriate experimental sections of those chapters.

#### 3.1 Surface Analysis Techniques

##### 3.1.1 Digital Microscopy

Digital microscopy is a technique that provides information about the topography and morphology of a surface. The digital microscope is a microscope without an eyepiece, where a camera acts as the detector and images are displayed on a screen. The microscope produces an image by focusing the lens on a particular point of the sample. The digital microscope can produce high resolution, multi-focus, and 3D images of the surface morphology.

In this work the digital microscope was used to analyze the surface morphology of copper coupons exposed to different environments. The images were produced using a Leica DVM 6A digital microscope. The same lighting settings were used to image each sample.

### 3.1.2 Raman Spectroscopy

Raman spectroscopy is a spectroscopic technique that provides information about the chemical phase and composition of a molecule. A monochromatic light source, typically a laser beam, is used to irradiate the sample. The incident radiation is scattered by certain molecules and the scattered light is detected. Scattering involves a distortion of electrons distributed around a bond in a molecule, followed by reemission of the radiation as the bond returns to its normal state. [1] When a molecule is struck by light, it can absorb the energy of the light and become excited to a virtual state. When this excitation occurs, the molecule can scatter the light elastically or inelastically. Elastic (or Rayleigh) scattering occurs when the photon emitted has the same energy as the incident photon. The molecule may also relax back to its original electronic state, but in a different vibrational or rotational state. This results in the emission of a photon with different energy than the incoming light. If the energy is lower than the incident photon energy, the shift in the frequency of light is called a Stokes shift. If it is higher than the incident photon energy, it is called an Anti-Stokes shift [2-4]. These processes are illustrated below in **Figure 3.1**.

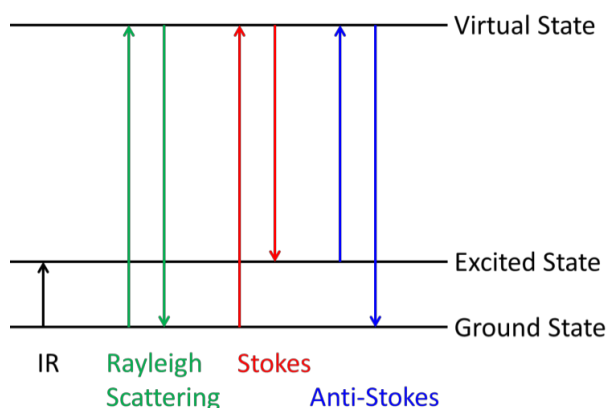


**Figure 3.1:** Illustration showing IR absorption, Rayleigh scattering, Stokes shift, and Anti-Stokes shift processes. Arrows pointing upward correspond to light absorption processes, while those pointing downward correspond to light emitting processes.



Raman scattering measurements were performed using a Renishaw model 2000 Raman Spectrometer with a laser excitation wavelength of 633 nm. The 50x objective lens was used to focus on the copper surfaces and spectra were recorded over the wavenumber range 120-2000  $\text{cm}^{-1}$  at 0.5 mW of power. Spectra were calibrated using the 520.5  $\text{cm}^{-1}$  line of a silicon wafer. Raman scattering measurements were carried out at Surface Science Western.

### 3.1.3 Scanning Electron Microscopy and Energy Dispersive X-ray Spectroscopy

Scanning electron microscopy (SEM) is a surface analysis technique used to examine the morphology of a surface. It can also provide information about the particle sizes of a sample. The SEM operates by directing a high-energy electron beam onto a sample in order to yield high-resolution images, as shown in **Figure 3.2**. The beam of electrons is accelerated through scanning coils that move the beam along the sample. When the beam of electrons interacts with the sample, secondary electrons are ejected. The secondary electrons are generated via inelastic collisions between the electron beam and the material. The secondary electrons are collected above the sample by a detector and an image is produced at every point that the beam interacts with the sample.

SEM analysis was performed using a LEO (Zeiss) 1540XB FIB/SEM microscope in order to examine the morphology of the particles formed. SEM analyses were carried out at the Western Nanofabrication Facility.

### Scanning Electron Microscope

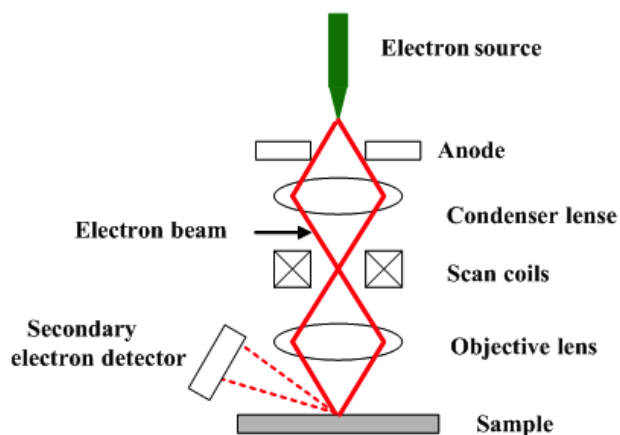


**Figure 3.2:** Illustration of scanning electron microscope (SEM).

Energy dispersive x-ray (EDX) spectroscopy is a semi-quantitative technique used to determine the elemental composition of a sample. As the electrons interact with a sample, a core electron is ejected. Once the core shell electron is ejected, a hole is created and an outer shell electron will take its place to fill the vacancy. The difference in energy between the outer and core shell electron will be emitted as an x-ray with energy characteristic of a certain element, as illustrated in **Figure 3.3**. EDX analyses were carried out at the Western Nanofabrication Facility.

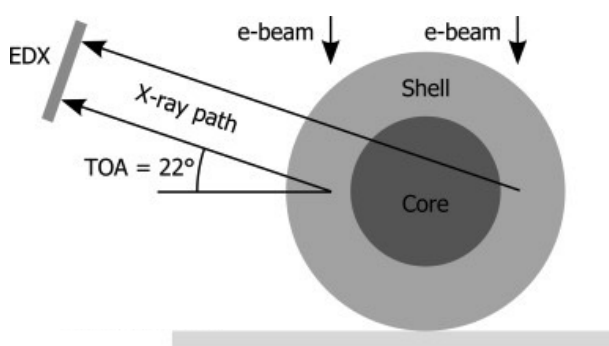


**Figure 3.3:** Illustration of Energy dispersive x-ray (EDX) spectroscopic technique.

### 3.1.4 Focused-Ion Beam Milling

Focused-ion beam (FIB) milling or sputtering is a technique used to study the morphology of a cross-section. It is also a useful technique for determining the oxide thickness on a sample. As the focused-ion beam sputters the surface, secondary electrons are generated. These secondary electrons are collected to form an image. Gallium ions were used to sputter the surface at an accelerating voltage between 5 to 50 keV. FIB milling was carried out at the Western Nanofabrication Facility.

### 3.1.5 X-ray Diffraction

X-ray diffraction (XRD) is a technique used to identify the phase of a crystalline material. It also provides information about the crystal's unit cell dimensions. A sample is bombarded with an x-ray; this causes the crystalline material to diffract the incident beam into a pattern of diffracted beams with specific angles and intensities, as shown in **Figure 3.4**. By converting the diffraction peaks to d-spacings, the crystal can be identified, as each crystalline phase has a characteristic set of d-spacings. XRD analyses were performed at the Western X-ray Facility.

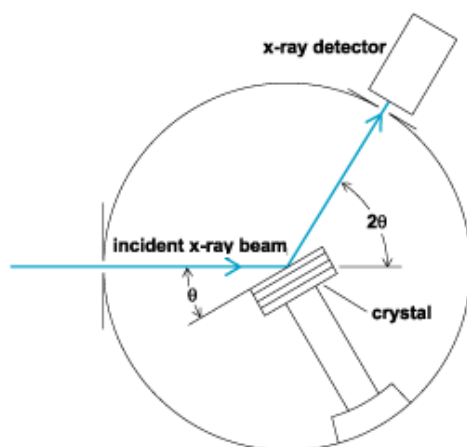


**Figure 3.4:** Illustration of X-ray diffraction (XRD) technique.

## 3.2 Chemical Analysis Techniques

### 3.2.1 Inductively Coupled Plasma Mass Spectrometry

Inductively coupled plasma mass spectrometry (ICP-MS) is an analytical technique used to determine the concentration of elements in a sample. ICP-MS combines a high temperature inductively coupled plasma source with a mass spectrometer as illustrated in **Figure 3.5**. The inductively coupled plasma is a plasma source where the energy is supplied by electric currents produced by a magnetic field. The sample introduction can be preceded by separation techniques depending on the type of sample being analyzed. For liquid samples, High Performance Liquid Chromatography (HPLC) can be used to separate components before introduction to the plasma. Once the sample is introduced to the system, an aerosol is generated. The elements in the sample are then converted to gaseous atoms and ionized by the plasma source. The ions are then separated based on their mass to charge ratio and detected by the mass spectrometer. Typically, an argon plasma source is used for ICP-MS analysis.

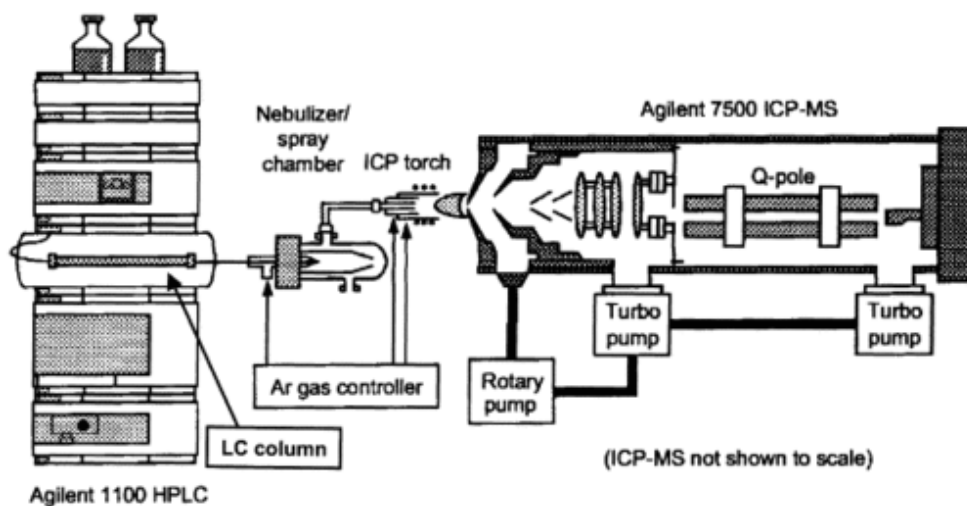


**Figure 3.5:** Illustration of inductively coupled plasma mass spectrometry (ICP-MS).

In this work, ICP-MS was used to determine the concentration of dissolved copper present in the test solution after irradiation. These analyses were performed at the Biotron facility using an Agilent 1260 Infinity HPLC connected directly to an Agilent 7700 Series ICP-MS.

### **3.3 Experimental Procedures**

#### **3.3.1 Sample Preparation**

The test coupons used in this study were cut from wrought copper samples (provided from SKB, The Swedish Nuclear Waste Management Company, 99.9% purity). The coupons were polished manually with 400, 600, and 1200 grit silicon carbide papers on a grinder polisher wheel (Grinder-Polisher Buehler (MetaServ 2000)). The coupons were sonicated first in methanol and then in water purified with a NANOpure Diamond UV ultra-pure water system (Barnstead International) with a resistivity of 18.2 MΩ·cm. The copper coupons were dried with argon gas, then placed in a glass-quartz vial and sealed using aluminum crimp caps with polytetrafluoroethylene (PTFE) silicone septa. The test solutions were pH 6.0 and 9.0 solution. The desired volume of the test solution (200 or 50 μL) was added to the surface of each coupon using a syringe, forming a droplet on the surface. The vials were then placed in a cobalt-60 (<sup>60</sup>Co) gamma-irradiation cell for different durations.

### **3.4 Irradiation Technique**

#### **3.4.1 Sample Irradiation**

The sample vials were placed in a custom designed sample holder to ensure a uniform dose to all vials throughout the irradiation period. The irradiation was carried out in a MDS

Nordion Gamma Cell 220 Excel  $^{60}\text{Co}$  irradiator. The  $^{60}\text{Co}$  radiation source has a half-life of 5.3 years and emits two characteristic  $\gamma$ -photons with energies of 1.332 MeV and 1.173 MeV [6].



A  $\beta$ -particle is also emitted with an energy of 0.318 MeV, but this particle is easily blocked from entering the irradiation chamber by the metal shielding around the chamber. The absorbed radiation dose rate in the irradiation chamber during the experiments was 3.0 kGy/h, where 1 Gy = 1 J absorbed per kg of water, determined using Fricke Dosimetry.

### 3.4.2 Fricke Dosimetry

A Fricke dosimeter is a chemical dosimeter used to quantify the amount of energy deposited by ionizing radiation in the irradiated system. The Fricke dosimeter consists of an aerated solution of 1 mM  $\text{FeSO}_4$  under acidic conditions (0.4 M  $\text{H}_2\text{SO}_4$ ). Under these conditions,  $\text{Fe}^{2+}$  will be oxidized to  $\text{Fe}^{3+}$  by the oxidizing radiolysis products as shown in the reaction scheme below (**Figure 3.6**).

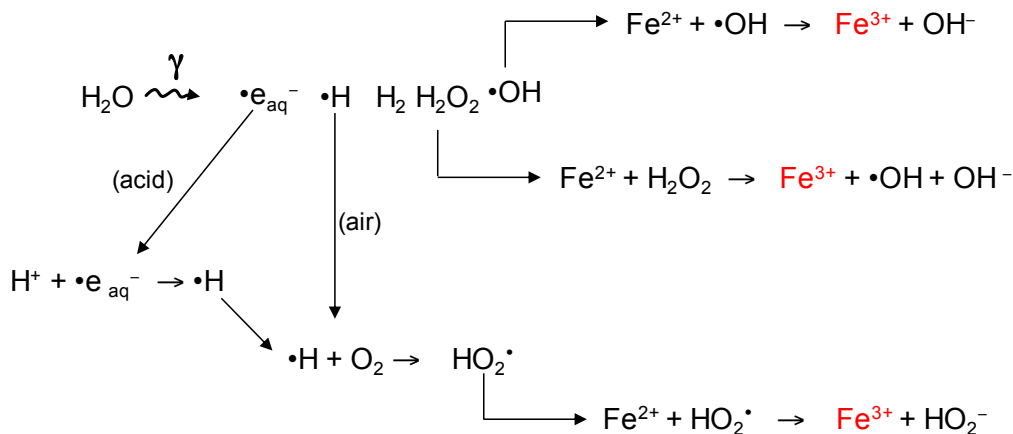


**Figure 3.6:** Schematic representation of the reactions occurring during Fricke dosimetry.

The rate of oxidation of  $\text{Fe}^{2+}$  to  $\text{Fe}^{3+}$  is dictated by the rate of generation of the oxidizing radiolysis products. A known volume of the Fricke solution is irradiated using the gamma cell for a fixed amount of time (60 s). The amount of  $\text{Fe}^{3+}$  produced is determined by measuring the absorbance at 304 nm and the dose is calculated from equation 3.2,

$$Dose(Gy) = \frac{9.648 * 10^6 * \Delta A_{304}}{\varepsilon_{304} l \rho G(products)} \quad (3.2)$$

where  $\Delta A_{304}$  is the difference in the absorbance of the irradiated sample and a sample that was not irradiated,  $\varepsilon_{304}$  is the molar extinction coefficient of  $\text{Fe}^{3+}$  at 304 nm,  $l$  is the length of the UV-Vis cuvette that the light passes through,  $\rho$  is the density of the dosimeter solution (1.024  $\text{g/cm}^3$ ),  $G(products)$  is the known dose required to generate the species necessary to produce the observed  $[\text{Fe}^{3+}_{(aq)}]$  (15.5),  $t$  is time, and  $9.648 \times 10^6$  is a proportionality constant [6].

### 3.5 Sample Analyses after Irradiation

Individual vials were removed from the irradiation chamber at regular time intervals for aqueous and surface analysis. The solution phase was analyzed using ICP-MS for the dissolved copper. The topography and morphology of the coupon surface were analysed using digital optical microscopy and scanning electron microscopy (SEM). The composition of the oxide formed on the coupon surface was analysed using Raman spectroscopy, energy dispersive x-ray (EDX) spectroscopy, and x-ray diffraction spectroscopy (XRD). Focused-ion beam (FIB) milling was used to determine the thickness of the oxide layer.

### 3.6 References

1. D.A. Skoog, F.J. Holler, S.R. Crouch, *Principals of Instrumental Analysis*, 6<sup>th</sup> Ed, Brooks/Cole, Belmont, CA, 2007.
2. E. Smith, G. Dent, *Modern Raman spectroscopy: a practical approach*, John Wiley, Hoboken, NJ; Chichester, UK, 2005.
3. R. L. McCreery, *Raman Spectroscopy for Chemical Analysis*, John Wiley & Sons, New York, 2000.
4. J. R. Ferraro, *Introductory Raman Spectroscopy*, Academic Press San Diego, CA, 1994.
5. R.F. Egerton, I. Books, *Physical principles of electron microscopy: an introduction to TEM, SEM, and AEM*, Springer Science & Business Media, New York, 2005.
6. J. W. T. Spinks and R. J. Woods, *An Introduction to Radiation Chemistry*, Wiley-Interscience, New York, 1990.



## Chapter 4

### Evolution of Surface Morphology During Corrosion of Rectangular Copper Coupons Under 200 $\mu\text{L}$ Water Droplets

#### 4.1 Introduction

The evolution of surface morphology during water droplet corrosion of copper was initially investigated using a water volume of 200  $\mu\text{L}$  on rectangular (1 cm  $\times$  0.7 cm) coupons. The water droplets on these coupons form ellipsoidal shapes whose two axes spread to the edges of the coupons, as shown in **Figure 4.1**. The water droplet corrosion study presented in this chapter was conducted with aerated water droplets with their initial pHs adjusted to 9.0 using NaOH. The initial pH 9.0 was chosen because both cuprous and cupric species have their minimum solubilities at this pH. The kinetics of copper corrosion were investigated by following surface changes only, and no dissolved copper analysis was performed. Thus, the information obtained in this study is more qualitative in nature. A better controlled study on water droplet corrosion of copper and the effect of pH on the corrosion kinetics was performed using 50  $\mu\text{L}$  water droplets on 1-cm diameter circular coupons. The results from that study are presented in Chapter 5. This chapter presents the results obtained using 200  $\mu\text{L}$  water droplets on the rectangular coupons.

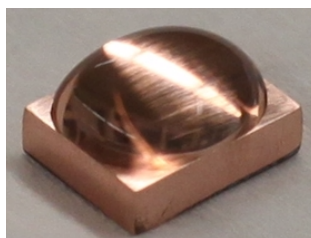


**Figure 4.1:** A 200  $\mu\text{L}$  water droplet on the surface of a rectangular copper metal surface.

## 4.2 Experimental Details

### 4.2.1 Sample Preparation and Test Procedure

The copper metal coupons used in this study were fabricated from a wrought copper block provided by SKB, the Swedish Nuclear Fuel and Waste Management Company. The coupons were cut to dimensions of 1 cm × 0.7 cm × 0.3 cm. Each side of the coupon was polished manually with a series of silicon carbide papers with successively finer grits (400, 600 and 1200 grit). The polished coupons were then cleaned by sonication in methanol followed by washing with water purified with a NANOpure Diamond UV ultra-pure water system (Barnstead International) with a resistivity of 18.2 MΩ·cm, and finally drying with argon (Ar). The polished and dried coupons were placed in individual 20-ml glass vials (Agilent Technologies). The vials were sealed with a PTFE (polytetrafluoroethylene) silicon septum and aluminum crimp cap and the sealed vials were then purged with compressed hydrocarbon-free air (Praxair) for 30 mins.

The test solutions were prepared with water purified with a NANOpure Diamond UV ultra-pure water system (Barnstead International) to give a resistivity of 18.2 MΩ·cm. No other additives except for pH-controlling agents were used. The pH of the water was adjusted to 9.0 by adding 1 M sodium hydroxide stock solution dropwise. The pH of each solution was measured using an Accumet AB 15 (Fisher Scientific) pH meter. The test solution was then purged with hydrocarbon-free air for 60 min. Using a syringe, 200 μL of the prepared solution was placed on the surface of a coupon in the sealed test vial.

The test vials were then irradiated for a period of 12, 24, 36, 48, 72, or 96 h in a <sup>60</sup>Co gamma cell irradiator (220 Excel, MDS Nordion). The absorbed radiation dose rate in the irradiation chamber during the experiments was 3.0 kGy·h<sup>-1</sup>, where 1 Gy = 1 J absorbed per kg of water. The radiation dose rate was calculated using Fricke dosimetry.

## 4.2.2 Test Analyses

After irradiation, the vials were removed from the irradiation chamber and post-exposure tests were carried out. Each coupon was then removed from the test vial, dried with argon gas and stored under vacuum. The surface morphology and oxide composition were analysed using Raman spectroscopy, optical microscopy, x-ray diffraction (XRD), and scanning electron microscopy (SEM) on surfaces and on focused-ion beam (FIB) milled cross sections.

## 4.3 Results and Discussion

### 4.3.1 Progression of Overall Surface

**Figure 4.2** shows the low magnification optical micrographs of the entire surface areas of coupons irradiated for different durations. Comparison of the optical and SEM micrographs (to be presented later) shows that the different shades of colour in the optical images correlate well with the composition of the copper oxide or hydroxide and the average density and size of copper oxide particles on the surface.

The optical micrographs clearly demonstrate that oxide formation at any given time during water droplet corrosion is not uniform across the surface of a copper coupon, and that the surface morphologies of different areas evolve differently. The surface corroded for 12 h does not show any significant formation of oxide particles; the surface is relatively smooth and the colour is uniformly yellow across the surface. The optical image of the coupon corroded for 24 h shows a dark bluish band in the area along the edge of the water droplet while the inner areas are red. The dark region has spread to the entire area of the coupon after 36 h. The coupons corroded for longer than 48 h show more complicated combinations of different colours.

The time evolution of the surface morphologies of different areas was further investigated using high-magnification optical micrographs and SEM, and the results are discussed in detail in Section 4.3.2. The micrographs show that non-uniformity and concomitant high variability in the evolution of different areas on the copper surface are inherent to copper corrosion; see discussion in Section 4. The non-uniformity manifests increasingly with longer corrosion time, which may be due to the small water volume used in the experiments and variation in water layer thickness across the surface.

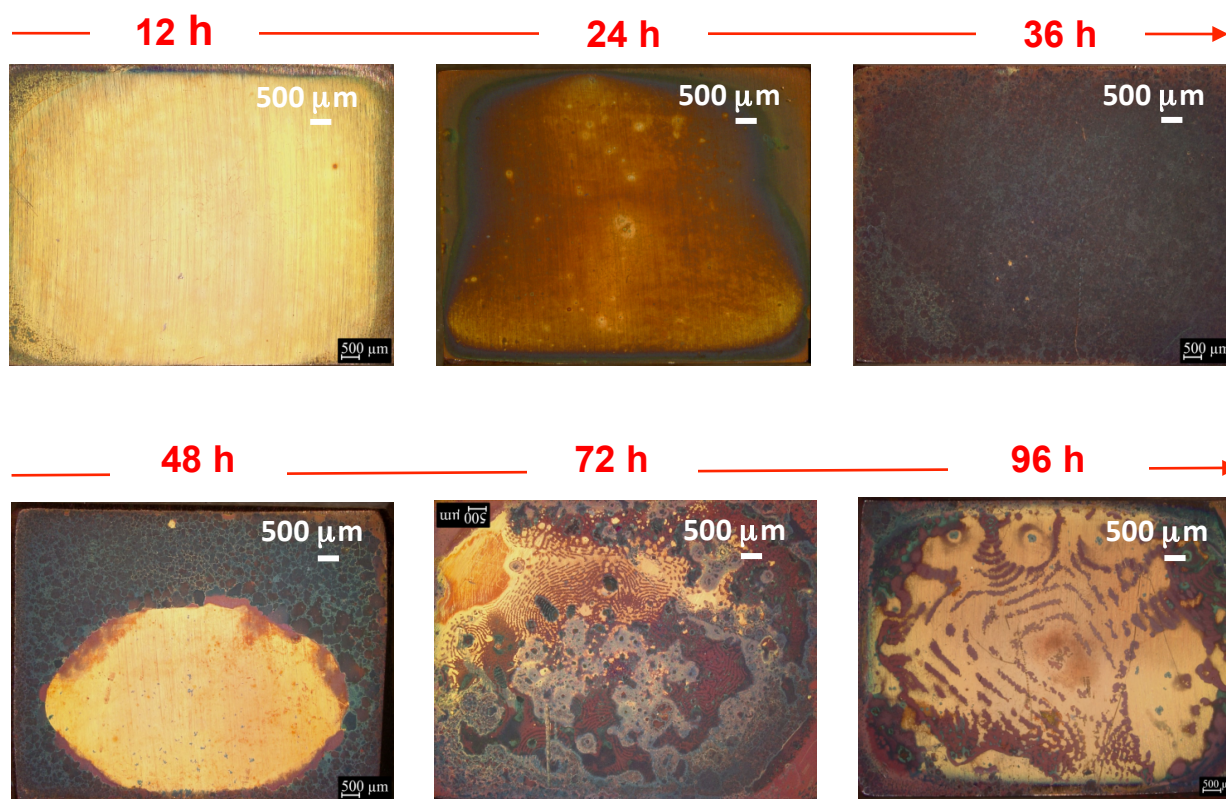


**Figure 4.2:** Optical micrographs of Cu coupons corroded in aerated water at pH 9.0 for different durations in the presence of  $\gamma$ -radiation at dose rate of  $3.0 \text{ kGy}\cdot\text{h}^{-1}$ .

The Raman and XRD analyses of the surfaces of coupons corroded for different durations are shown in **Figure 4.3** and **Figure 4.4**, respectively. The Raman spectra of all surfaces show

three main peaks at  $219\pm 1$ ,  $524\pm 4$  and  $626\pm 4$   $\text{cm}^{-1}$ , which correspond very well with those of  $\text{Cu}_2\text{O}$  [1-2]. Cupric hydroxide has main peaks at  $292\pm 1$  and  $489\pm 1$   $\text{cm}^{-1}$  while  $\text{CuO}$  has main Raman peaks at  $298\pm 2$ ,  $346\pm 1$  and  $610\pm 10$   $\text{cm}^{-1}$  [1-2]. The Raman scattering probabilities of  $\text{Cu}(\text{OH})_2$  and  $\text{CuO}$  are lower than that of  $\text{Cu}_2\text{O}$  [1-2]. Thus, the cupric hydroxide/oxide may be present on the surfaces, but was not detected by the Raman spectroscopy. (In a study on water droplet corrosion of copper, M. Naghizadeh et al. obtained the XPS spectra of large  $\text{Cu}_2\text{O}$  crystals present on a corroded surface and found that the large  $\text{Cu}_2\text{O}$  crystals formed at longer times are covered by a layer of  $\text{Cu}(\text{OH})_2$  a few nm thick [3]).

The XRD analysis results contain the diffraction patterns of both  $\text{Cu}$  and  $\text{Cu}_2\text{O}$  crystals as shown in **Figure 4.4**. The Raman spectrum in **Figure 4.3** indicates that a significant amount of  $\text{Cu}_2\text{O}$  is present on the 24 h corroded coupon. However, the XRD spectra obtained for the surface exhibit the features of  $\text{Cu}$  crystals, predominantly. The peak at  $2\theta = 43^\circ$  may contain the  $\text{Cu}_2\text{O}$  {200} component, but other  $\text{Cu}_2\text{O}$  components ({111}, {220} and {222}) are absent. The combination of the Raman and XRD results indicate that the  $\text{Cu}_2\text{O}$  present on the 24 h corroded coupon are mostly non-crystalline or amorphous  $\text{Cu}_2\text{O}$  particles. It could also indicate that after 24 h, there is less  $\text{Cu}_2\text{O}$  on the surface than at the longer irradiation times, and therefore could not be detected by XRD. The missing {111} component observed in the 24 h diffraction pattern could also be attributed to the changing morphology of  $\text{Cu}_2\text{O}$  crystals on the surface. Initially, the  $\text{Cu}_2\text{O}$  crystals grow with {100} facets. However, the {100} component would be observed at  $2\theta = 21.5^\circ$ , which is not within the detection limit of the instrument used. The XRD spectra of the surfaces corroded for longer durations show the presence of  $\text{Cu}_2\text{O}$  crystals.

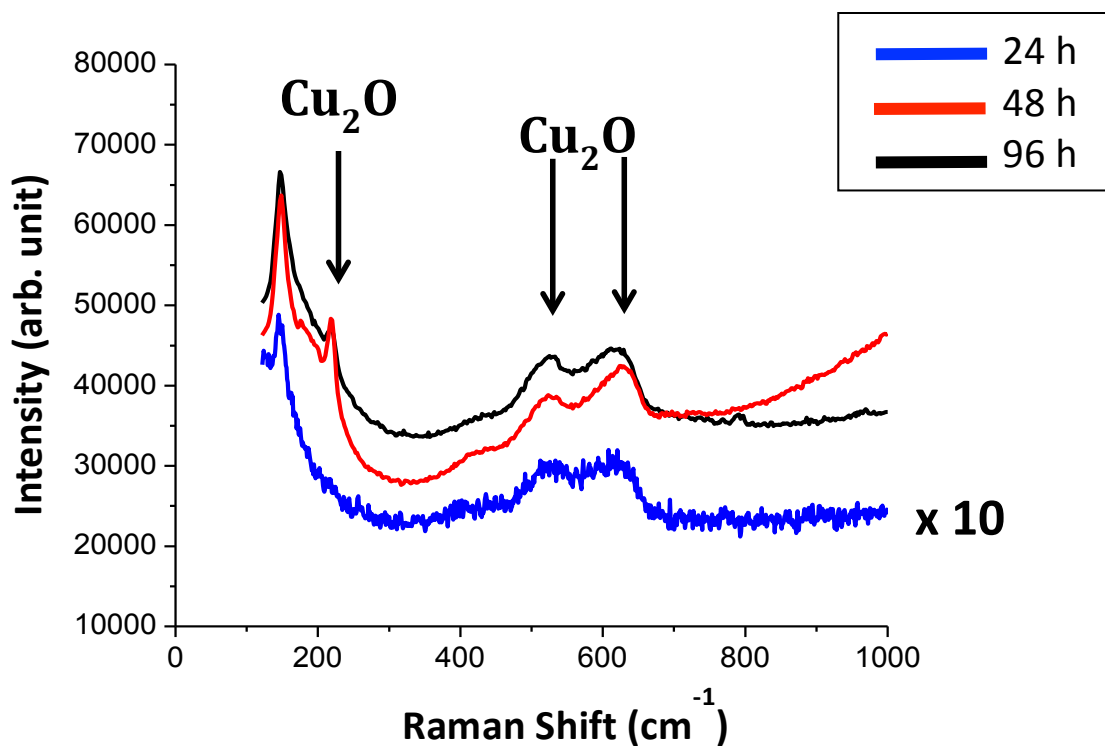


**Figure 4.3:** Raman spectra of the surfaces of the Cu coupons corroded for different periods (24, 48 and 96 h) at pH 9.0 in aerated water in the presence of  $\gamma$ -radiation at  $3.0 \text{ kGy}\cdot\text{h}^{-1}$ .

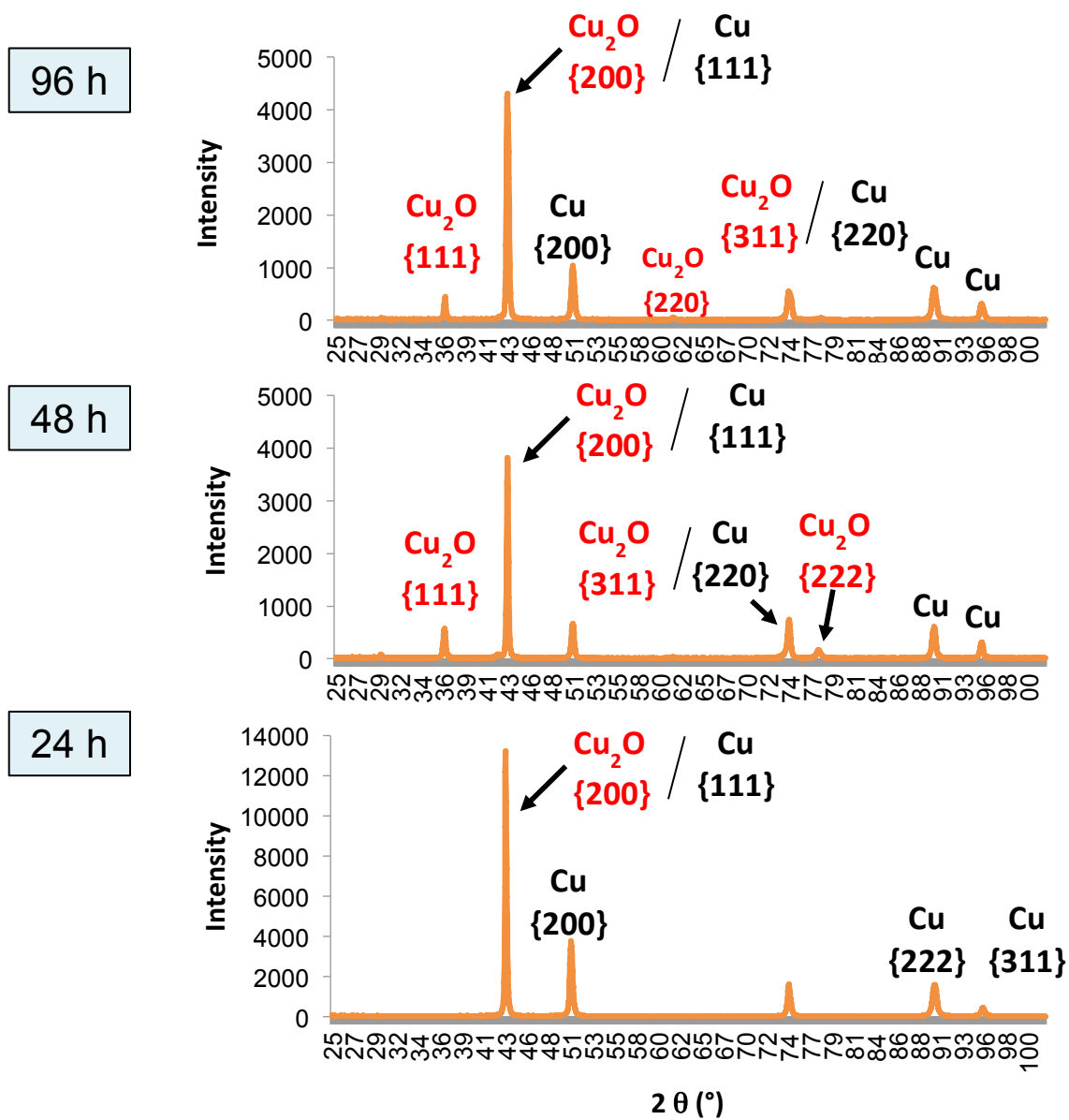


**Figure 4.4:** XRD spectra of the surfaces of the Cu coupons corroded for different periods (24, 48 and 96 h) at pH 9.0 in aerated water in the presence of  $\gamma$ -radiation at  $.0 \text{ kGy}\cdot\text{h}^{-1}$ .

### 4.3.2 Evolution of Morphology of Different Areas Across Surface

The low magnification optical images presented in **Figure 4.2** demonstrate that the copper oxide/hydroxide particle formation is not uniform across the surface and that the surface morphologies of different areas evolve differently. The time-evolutions of the surface morphologies of different areas were examined in more detail using high-magnification optical micrographs and SEM, and their results are presented in **Figure 4.5** to **Figure 4.17**.

The micrographs of different areas of the 24 h corroded coupon are shown in **Figure 4.5**. Comparison of the optical with SEM micrographs shows that the centre region (area a) is uniformly covered with a few nm sized granular particles, on which 10-100 nm sized polyhedron crystals with well-defined facets are distributed sparsely. On the other hand, the area near the edge of the water droplet (area c) is densely packed with large polyhedron crystals. Within this purple-coloured region the density, size and morphology of the crystals are relatively uniform with average size of a few  $\mu\text{m}$ . The SEM images of area (d) show that the density and the average size of polyhedral crystals decrease sharply with distance away from the circumference towards the centre. The optical micrograph of the transition area shows the colour changing from blue to purple, pink, and reddish brown. Depending on the size and purity, the colour of  $\text{Cu}_2\text{O}$  particles ranges from yellow to red while  $\text{Cu}(\text{OH})_2$  is blue and  $\text{CuO}$  is black [4].

Comparison of the surface morphology with the Raman and XRD analyses of this surface (**Figures 4.3** and **4.4**) indicate that the small particles in the centre region are  $\text{Cu}_2\text{O}$ , giving the region the red colour. The SEM images indicate that some of the  $\text{Cu}_2\text{O}$  particles have grown into crystals with well-defined facets during the 24 h corrosion. The average size of  $\text{Cu}_2\text{O}$  crystals is much smaller in the centre region, and the shapes of the particles in this region range from small cubes to truncated cubes. The shapes of the crystals formed in the higher particle-density region



(purple region) are closer to truncated octahedra to octahedra. As reviewed in Chapter 2, single crystals of  $\text{Cu}_2\text{O}$  are able to grow successively from cubes to truncated cubes, and then truncated octahedra and octahedra as the crystals grow in a solution medium [5-12]. The observed sizes and shapes of the  $\text{Cu}_2\text{O}$  crystals are consistent with the expectation that the  $\text{Cu}_2\text{O}$  crystals grow at faster rates in the outer than in the inner area, and that crystals formed earlier grow larger faster with time.

The SEM images also show that these oxide particles are formed preferentially along the scratch lines created during polishing of the coupon surface. This indicates that the seed crystals of  $\text{Cu}_2\text{O}$  are formed earlier along the scratch lines and hence the  $\text{Cu}_2\text{O}$  crystals grow bigger over a same growth period. The metal used for this study is a wrought copper and contains metal grains, tens to hundreds of  $\mu\text{m}$  in size. It has been reported that the catalytic, thermal and electrical properties of copper metal depend strongly on the specific crystal plane of the metal grain [13-14]. However, the surface morphology observed for the coupon corroded for 24 h does not show any effect of  $\text{Cu}^0_{(m)}$  grain orientation or grain boundary corrosion. This may indicate that oxide particle nucleation rather than interfacial charge transfer (or electrochemical reaction) is the rate controlling step for  $\text{Cu}_2\text{O}$  particle growth at early stages of copper corrosion under the studied conditions (see further discussion in Chapter 6).

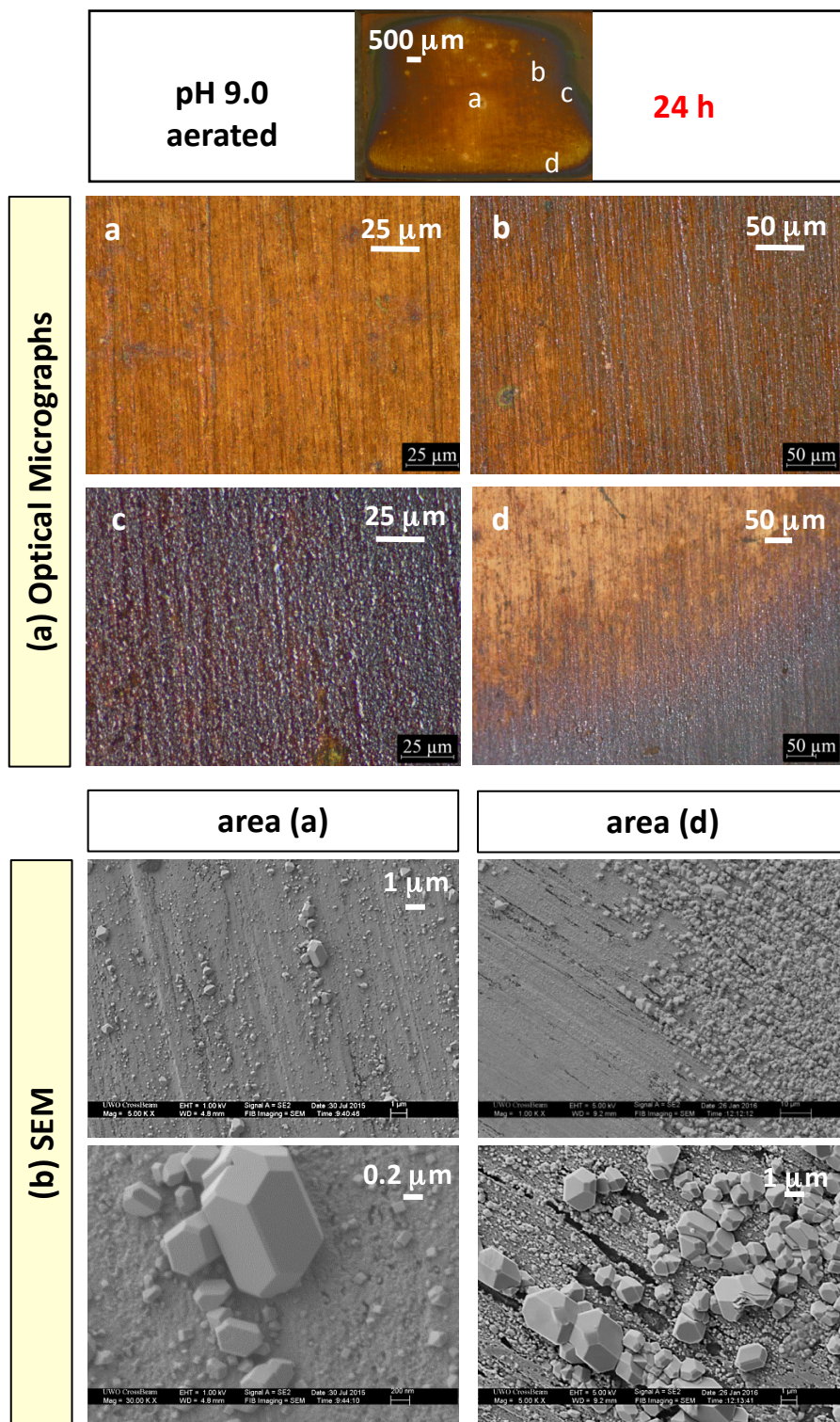
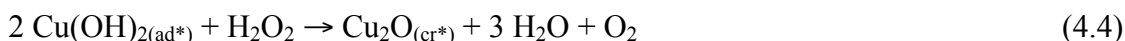
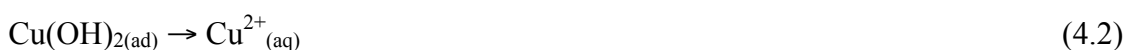
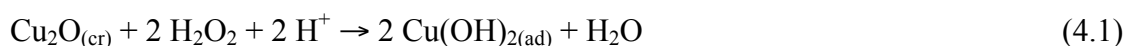


**Figure 4.5:** (a) Optical and (b) SEM micrographs with various magnifications of a Cu coupon corroded for 24 h in aerated water at pH 9.0 in the presence of  $\gamma$ -radiation at a dose rate of  $3.0 \text{ kGy}\cdot\text{h}^{-1}$ . The areas where the images were taken are indicated in the low-magnification optical micrograph shown on the top.

The surface of the coupon corroded for 36 h is completely covered with Cu<sub>2</sub>O particles (**Figure 4.6**). However, the number density of the particles varies across the surface. The most interesting observation is the development of circular oxide islands, 20 to 50 μm in size, separated by narrow channels. The SEM images of the coupon indicate that the channels are the areas where larger Cu<sub>2</sub>O crystals that formed earlier have begun dissolving. The SEM images also show bimodal size distributions of Cu<sub>2</sub>O crystals within individual islands, one centred around a few nm and the other centred around hundreds of nm. The bimodal size distribution may be a result of what we refer to as ‘redox-cycle-assisted ripening’, which causes larger crystals to grow and smaller crystals to diminish:



The asterisk implies the formation of “new” Cu(OH)<sub>2(ad)</sub> and Cu<sub>2</sub>O<sub>(cr)</sub> that can deposit onto the crystals formed earlier. The proposed mechanism for the growth of Cu<sub>2</sub>O is similar to Smoluchowski and Ostwald ripening [15] except that the dissolution and reprecipitation of crystals occurs through the oxidation product of a crystal constituent atom (see further discussion in Chapter 6).

It is not clear as to what contributes to the formation of circular islands. The sizes of the islands do not correspond to the sizes of copper metal grains of the samples used in this study that are 50-100 μm [16]. Furthermore, the larger crystals within the individual islands are still aligned preferentially along the scratching lines. Thus, the contribution of grain boundary corrosion to the channel formation is ruled out.

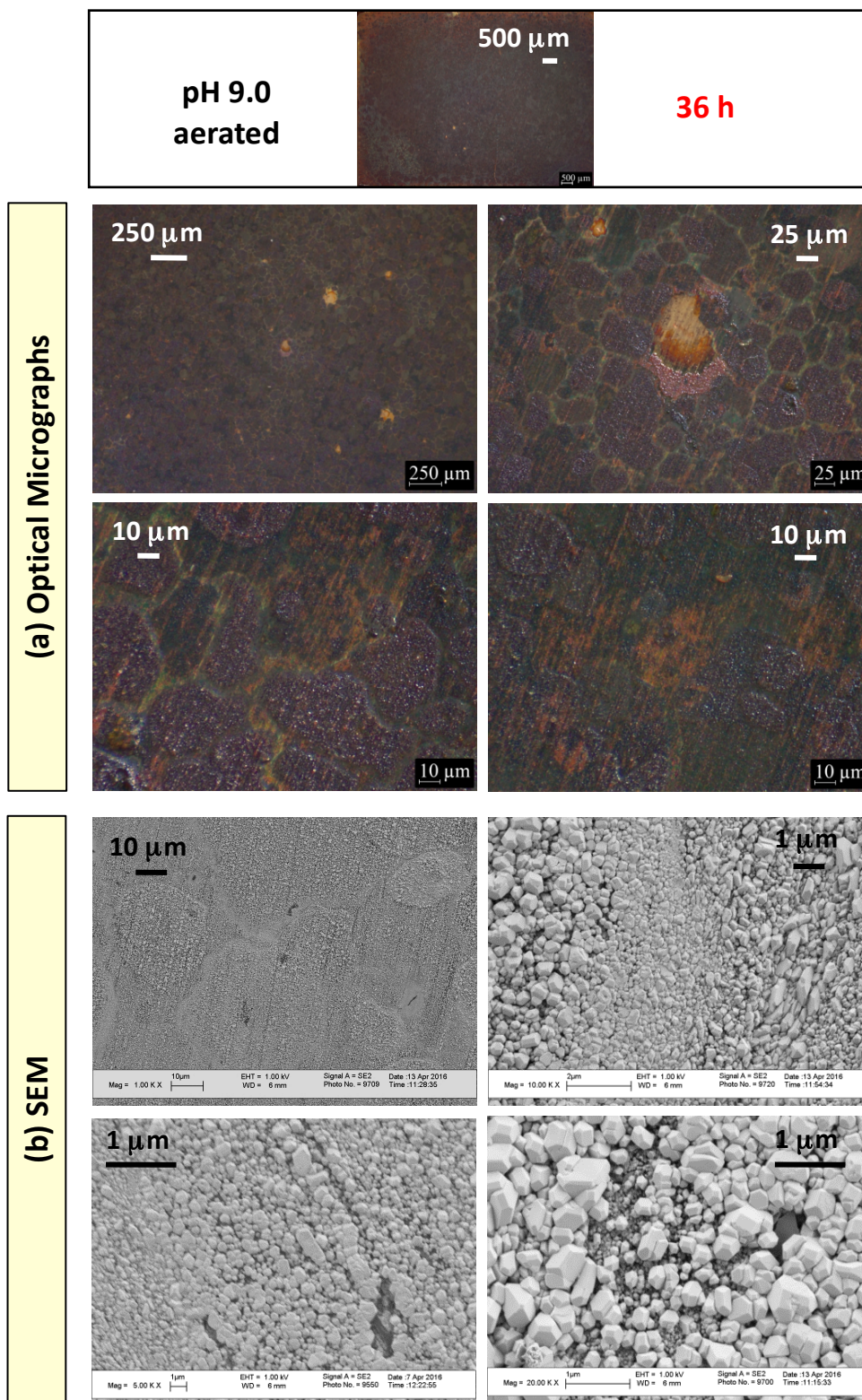


**Figure 4.6:** (a) Optical and (b) SEM micrographs with various magnifications of a Cu coupon corroded for 36 h in aerated water at pH 9.0 in the presence of  $\gamma$ -radiation at a dose rate of  $3.0 \text{ kGy}\cdot\text{h}^{-1}$ .

The optical and SEM micrographs of a coupon corroded for 48 h are shown in **Figure 4.7** to **Figure 4.10**. The low-magnification optical micrographs of the coupon shown in **Figure 4.2** illustrate that there are two broad regions with different densities of oxide particles. The central region is nearly free of oxide particles, while the outer region is densely covered by them. The transition between the two regions is relatively sharp. The underlying surface of the central region is very smooth. **Figure 4.7** shows that red and green spots (tens of  $\mu\text{m}$  sized) are distributed across the region. The red-coloured deposits are small  $\text{Cu}_2\text{O}$  particulates as discussed above. The green-coloured deposits in the central region (area a) can be seen more clearly in **Figure 4.8**. These deposits do not form granular particles, but rather spread more laterally and show dendritic edges. The colour and the morphology of these deposits suggest that they are  $\text{Cu}(\text{OH})_2$ .

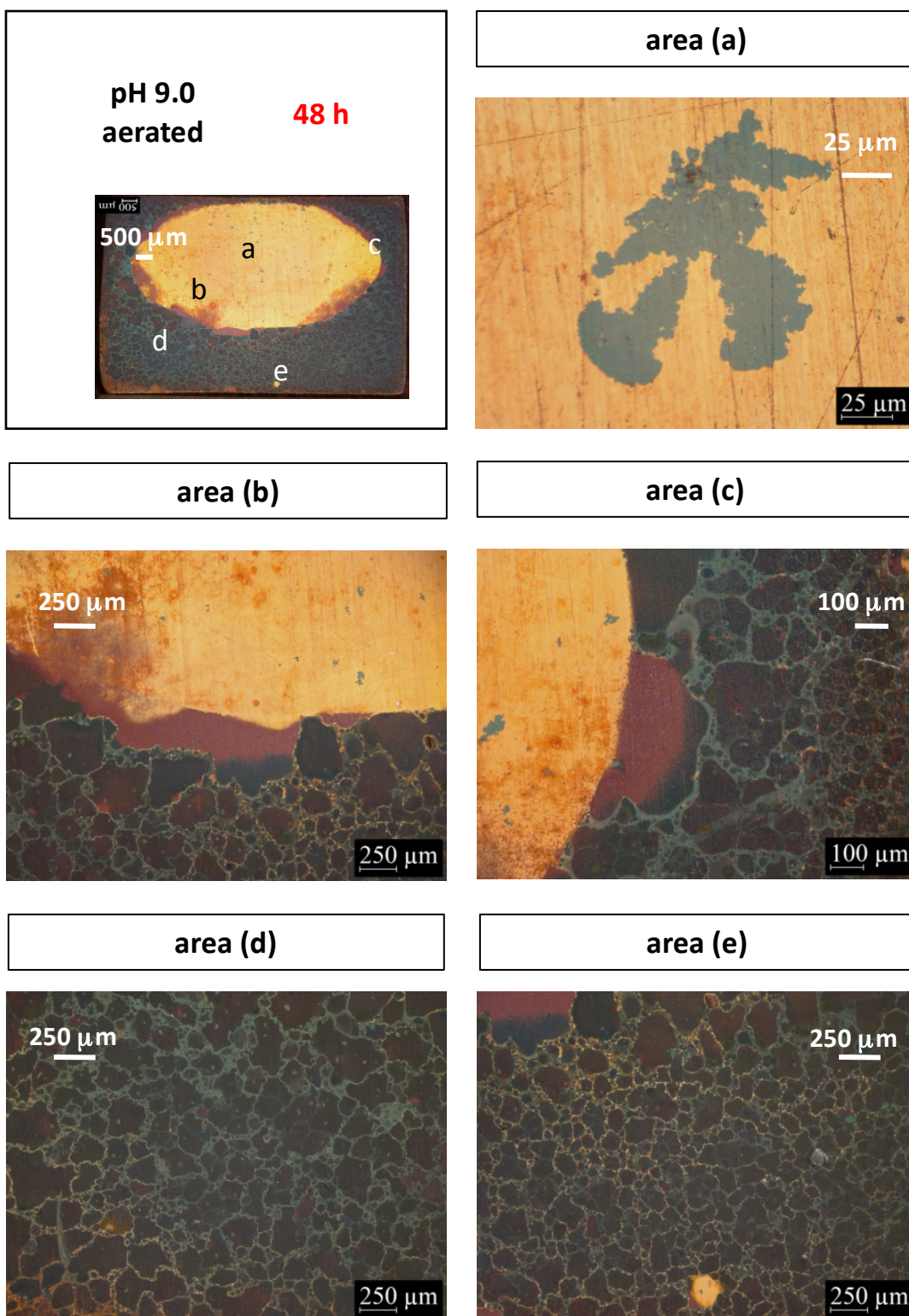


**Figure 4.7:** Optical micrographs with various magnifications of different areas of a Cu coupon corroded for 48 h in aerated water at pH 9.0 in the presence of  $\gamma$ -radiation at dose rate of  $3.0 \text{ kGy}\cdot\text{h}^{-1}$ .

The outer region (area d and e) shows a similar morphology to that of the general area of the surface corroded for 36 h (**Figure 4.6**), in which circular oxide islands separated by narrow channels are observed. The time progression of the morphology of the area containing these islands can be seen more clearly in **Figure 4.8**. Comparison of the surfaces of the coupons corroded for 36 h and 48 h reveals that some of the oxide islands containing large crystals merge to grow larger while smaller ones dissolve and thereby widen the channels separating the larger islands. The observed progression is a clear example of redox-cycle-assisted ripening or coarsening of islands.

On the 48 h corroded coupon, the channels surrounding the medium sized islands are green while the channels surrounding a few micron sized islands in-between large islands are yellow. These observations suggest that coarsening of  $\text{Cu}_2\text{O}$  islands in the presence of radiation involves  $\text{Cu}^{\text{II}}$  species ( $\text{Cu}^{2+}$ ,  $\text{Cu}(\text{OH})^+$  and  $\text{Cu}(\text{OH})_2$ ), further supporting the ‘redox-cycle-assisted’ ripening mechanism, reactions (4.1) to (4.4). The dissolved cupric ion ( $\text{Cu}^{2+}_{(\text{aq})}$ ) that is in quasi-redox-equilibrium with  $\text{Cu}_2\text{O}$  crystals can diffuse between the edges of individual islands, promoting the redox-cycle-assisted ripening (further discussion in Chapter 6).

The optical micrographs of the boundary between the central and the outer regions (areas b and c in **Figure 4.7**) show that the average size of the oxide islands becomes larger from the outer edge towards the boundary. In addition, the areas of some of the oxide islands at the boundary are magenta instead of dark green in the outer region. The SEM images of the islands presented in **Figure 4.9** show that the magenta area represents the islands of large  $\text{Cu}_2\text{O}$  polycrystals grown on top of each other. The thickness of the  $\text{Cu}_2\text{O}$  layer decreases sharply towards the central region, and large single crystals of octahedral shapes can be found adjacent to the densely packed islands.

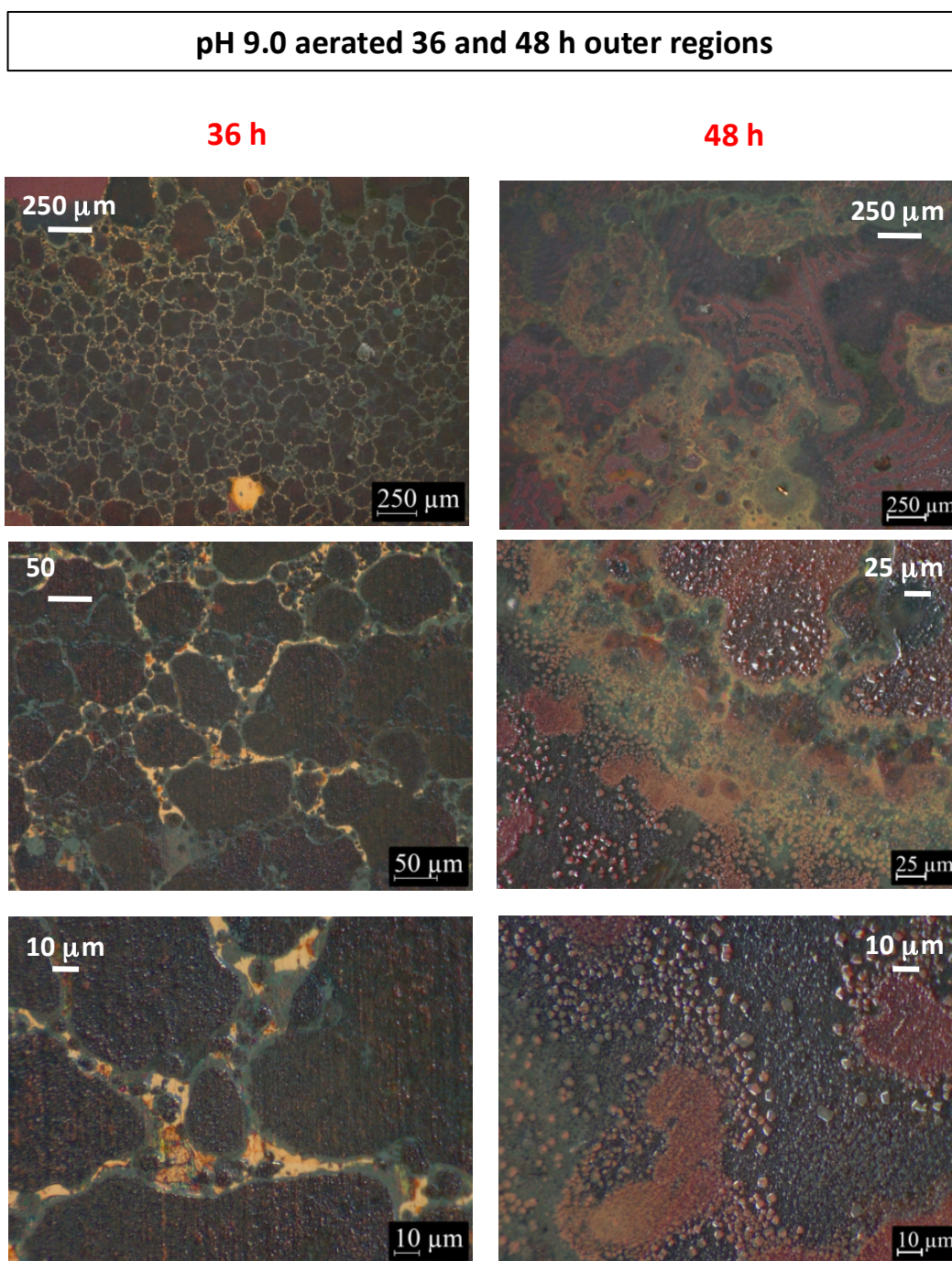


**Figure 4.8:** Comparison of optical micrographs of the areas containing circular oxide islands separated by narrow channels on Cu coupons corroded for 36 h and 48 h in aerated water at pH 9.0 in the presence of  $\gamma$ -radiation at dose rate of  $3.0 \text{ kGy}\cdot\text{h}^{-1}$ .



area (d) of Figure 4.7

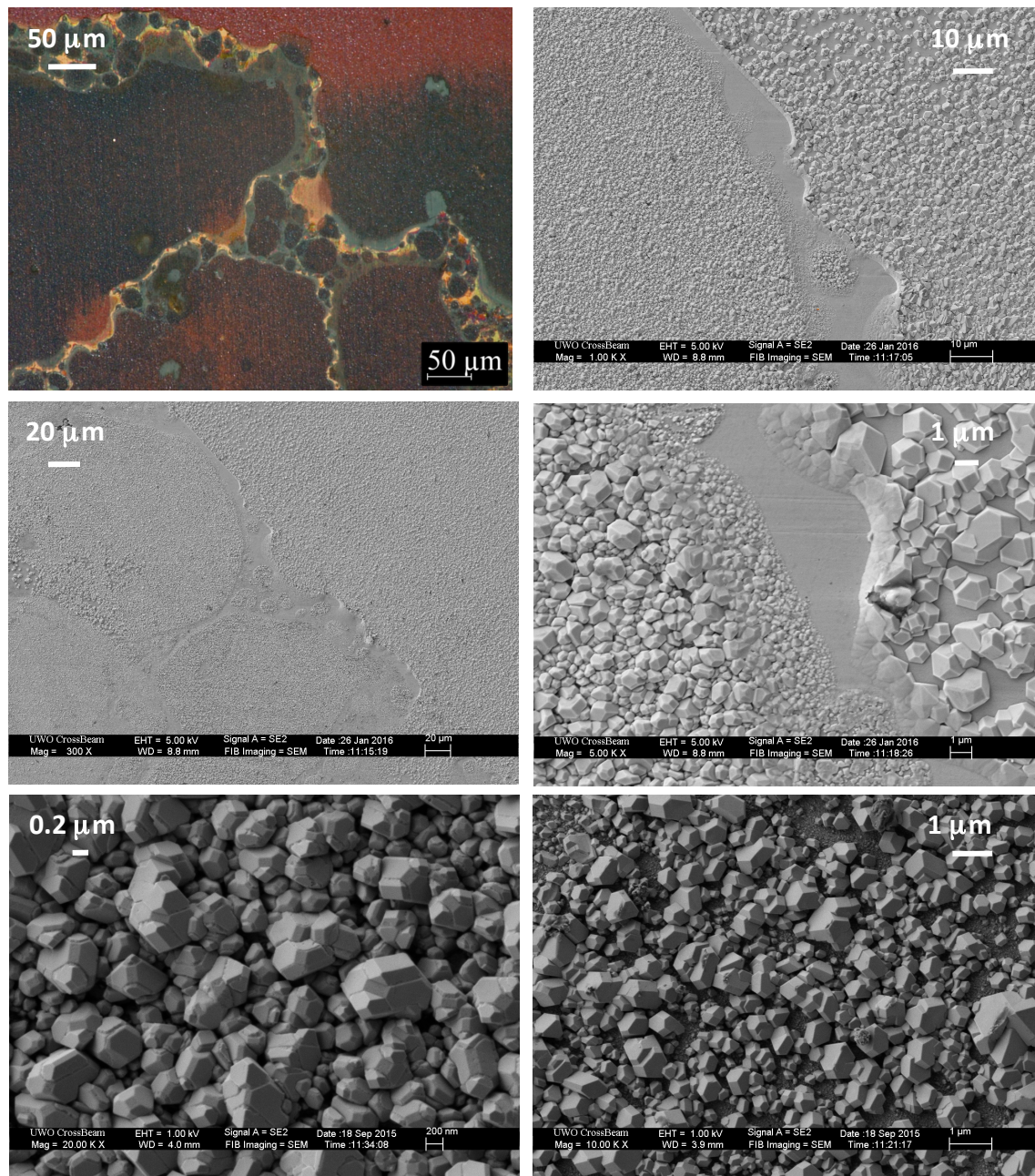


**Figure 4.9:** Optical and SEM micrographs of the boundary region (area d of Figure 4.7) on a Cu coupon corroded for 48 h in aerated water at pH 9.0 in the presence of  $\gamma$ -radiation at a dose rate of  $3.0 \text{ kGy}\cdot\text{h}^{-1}$ .

In comparison, the SEM images of the oxide islands in the outer region (area c in Figure 4.7) (**Figure 4.10**) show that the oxides are present as individual crystals. As observed for the 36 h corroded coupon, the size distribution of the oxide islands is bimodal, indicating that the redox-cycle assisted ripening is continuing. The  $\text{Cu}_2\text{O}$  crystals in some islands show clearly defined polycrystalline structures, showing the facets of the single crystals that constitute the polycrystals. The shapes suggest that these crystals would grow into the polycrystalline blocks shown in **Figure 4.9**.

area (c) of Figure 4.7

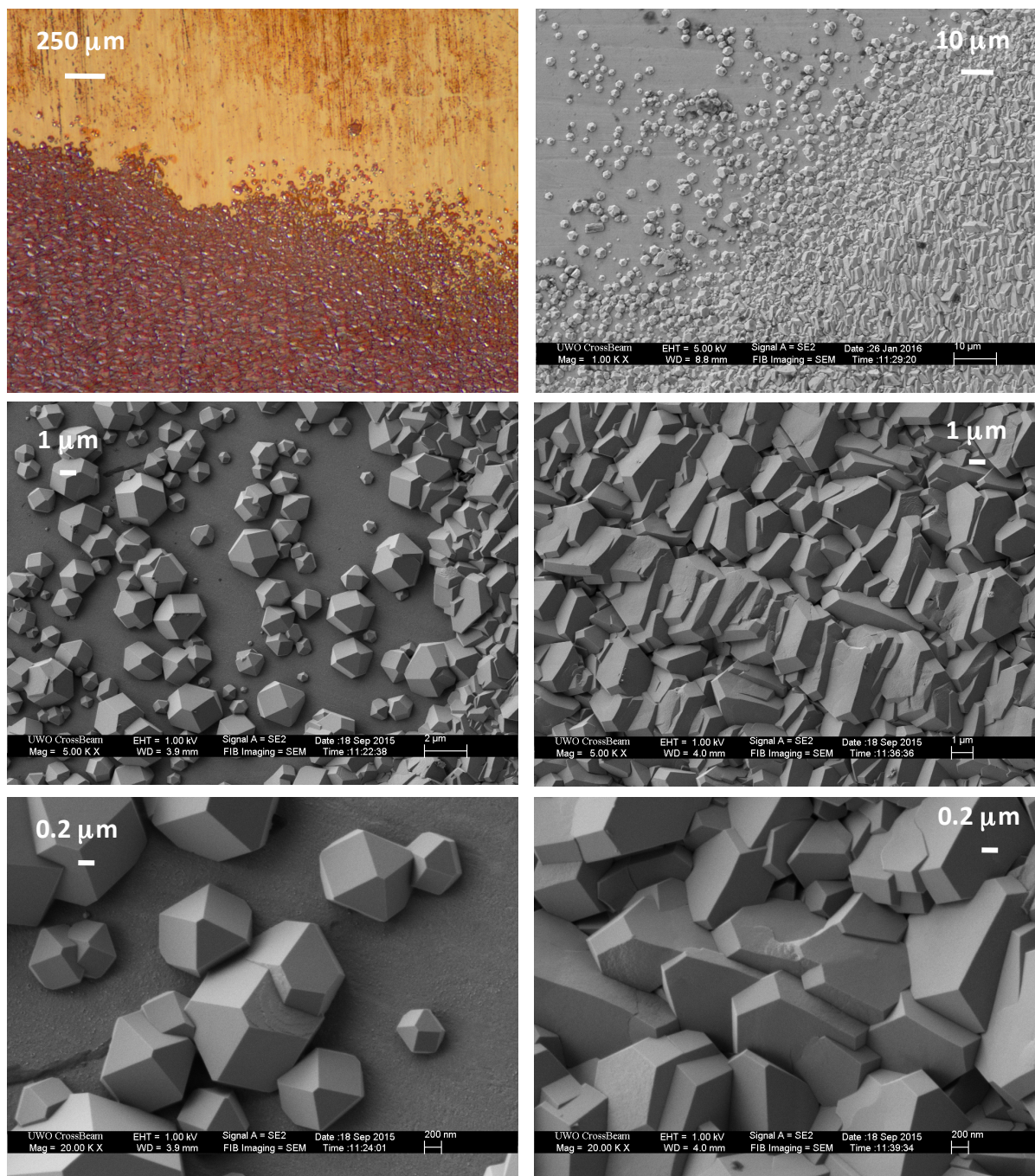


**Figure 4.10:** Optical and SEM micrographs of the oxide island region (area c of Figure 4.7) on a Cu coupon corroded for 48 h in aerated water at pH 9.0 in the presence of  $\gamma$ -radiation at a dose rate of  $3.0 \text{ kGy}\cdot\text{h}^{-1}$ .

The optical and SEM micrographs of different areas of a coupon corroded for 72 h are shown in **Figures 4.11 to 4.15**. **Figure 4.11** shows the optical micrographs of large areas. The micrograph of area (a) shows a large red to orange coloured section that is bordered with the area consisting of a light coloured and very smooth underlying surface with a series of magenta arc-shaped islands of densely packed  $\text{Cu}_2\text{O}$  crystals (see the SEM and higher magnification optical images to be shown later). Each group of the arc-shaped islands appears to form concentrically around a focal point, creating a wave pattern. Concentric arcs with different centre points intersect in certain places, creating an interference-like pattern. The micrograph of area (b) shows the transition of the area consisting of the magenta concentrically-arranged islands of  $\text{Cu}_2\text{O}$  crystals to the area consisting of mostly green-tinted circular islands with darker centres (see the micrograph of area c). The micrograph of area (d) shows that the area in between the green circular islands consists of concentric arc islands that have not yet been separated as well as those in area (a).

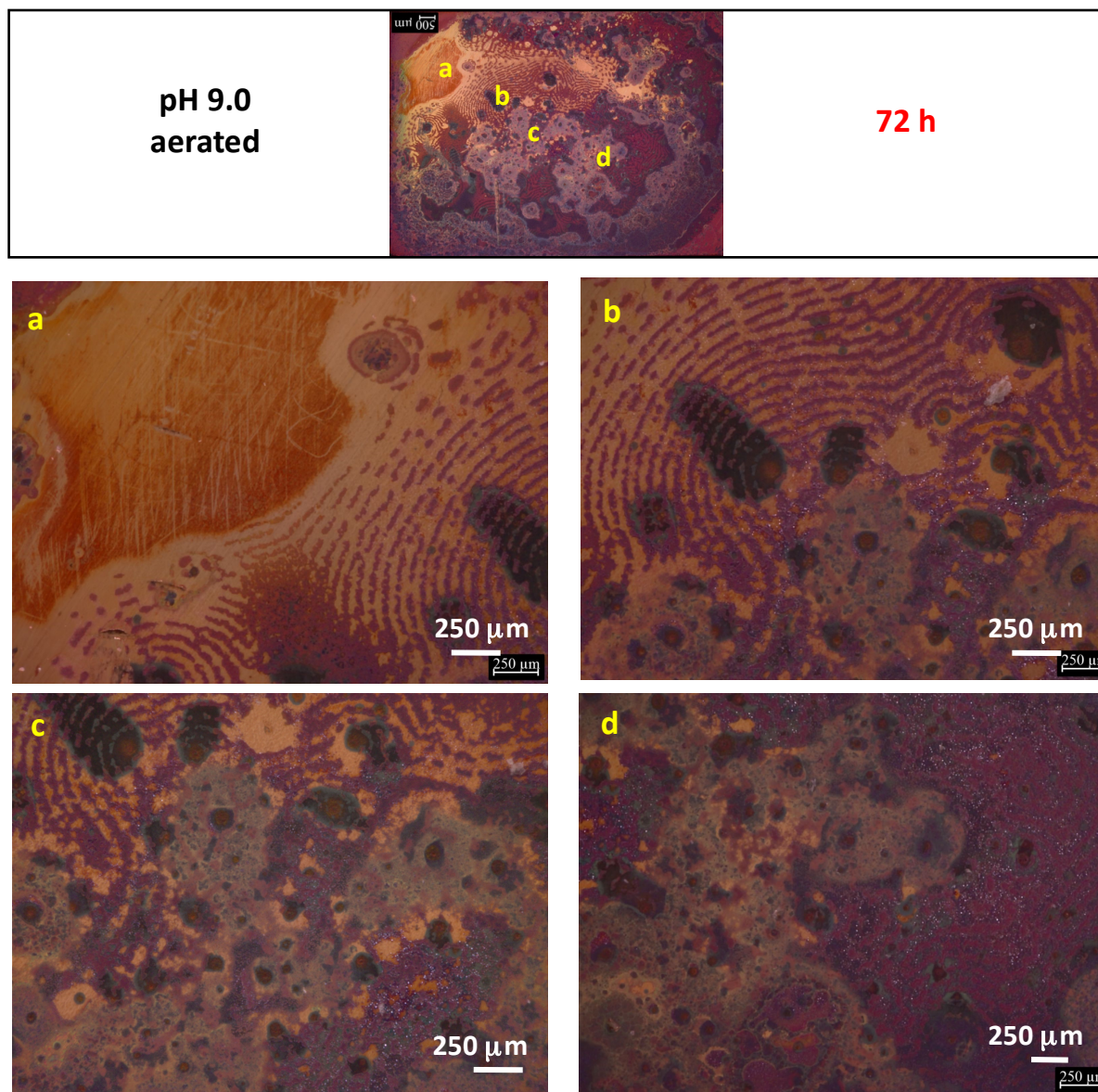


**Figure 4.11:** Optical micrographs of different areas on the surface of a Cu coupon corroded for 72 h at pH 9.0 in aerated water with radiation at a dose rate of  $3 \text{ kGy}\cdot\text{h}^{-1}$ . The approximate areas where the micrographs were taken are marked in the low magnification optical image shown on the top.

The higher magnification optical micrographs of the green-tinted circular islands with darker centres are presented in **Figure 4.12**. The SEM micrographs of similar areas are shown in **Figure 4.13**. These micrographs indicate that the green-tinted islands represent the areas where

the  $\text{Cu}_2\text{O}$  crystals had grown a few  $\mu\text{m}$  in size and then started dissolving. The green tint observed in the optical micrographs indicates that a combination of red  $\text{Cu}_2\text{O}$  particles with a blue gel-layer of  $\text{Cu}(\text{OH})_2$  is present.

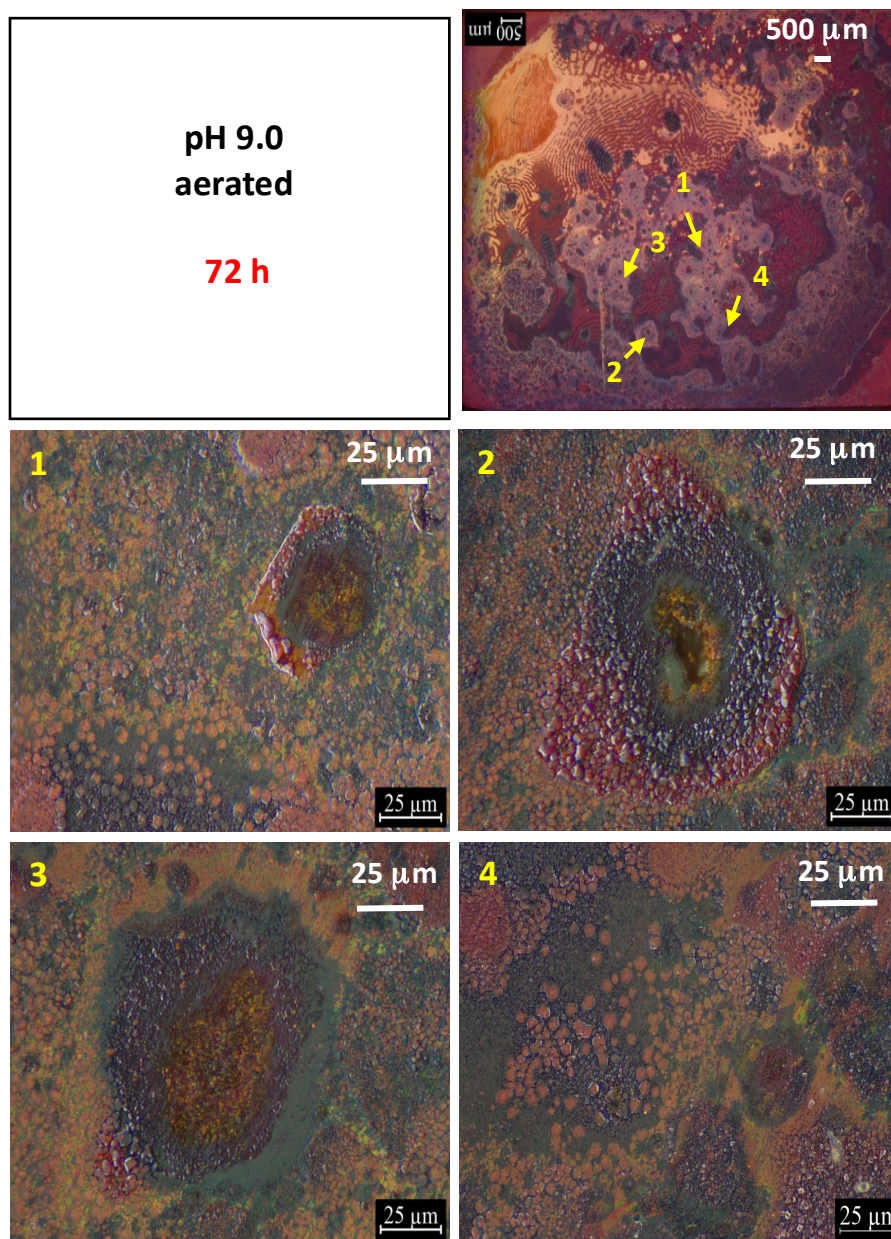


**Figure 4.12:** Optical micrographs of the areas showing partially dissolved  $\text{Cu}_2\text{O}$  crystals on a Cu coupon irradiated for 72 h at pH 9.0 in aerated water. The approximate spots where the micrographs were taken are marked in the low magnification optical image shown on the top.

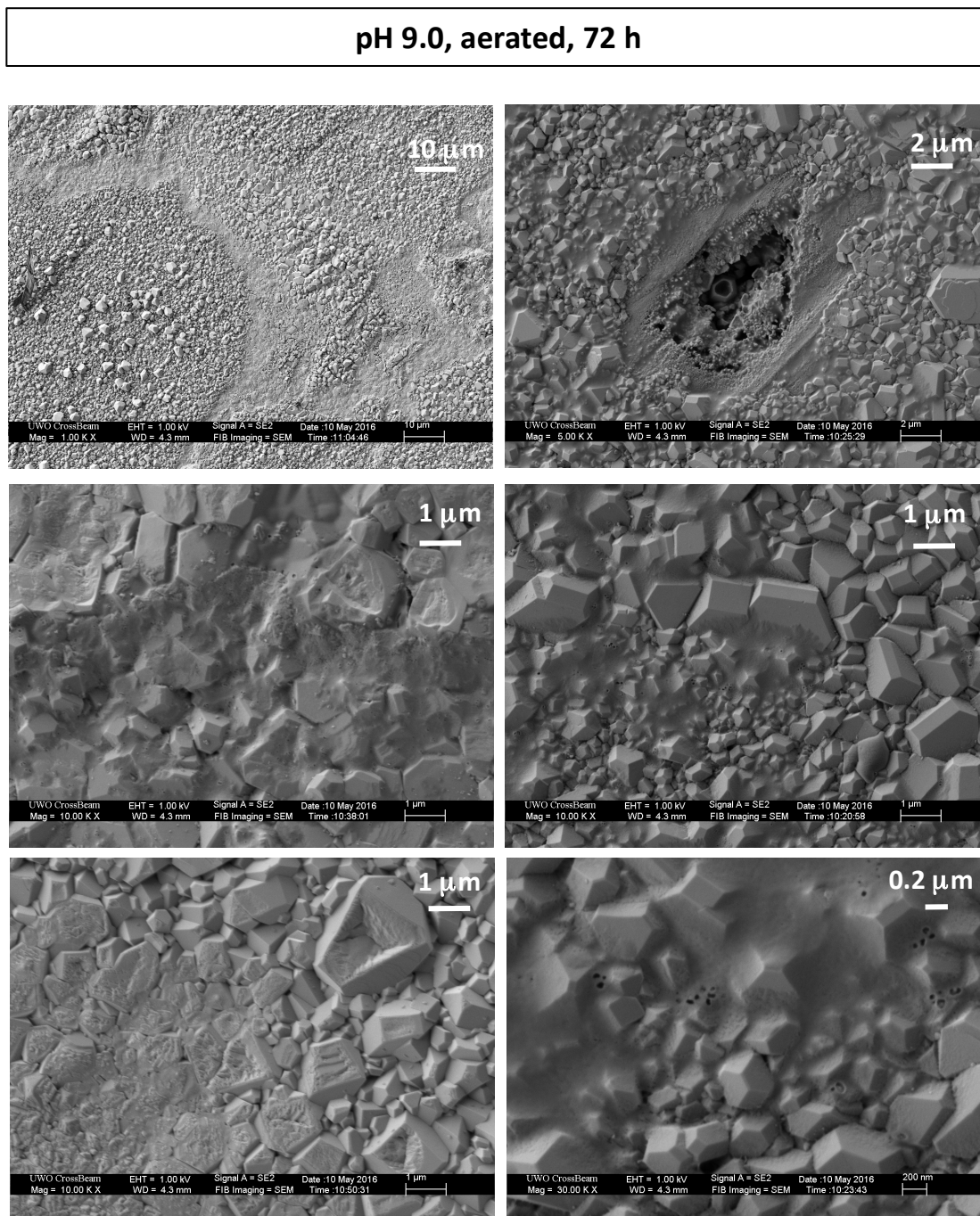


**Figure 4.13:** SEM micrographs of the areas showing partially dissolved  $\text{Cu}_2\text{O}$  crystals on a Cu coupon irradiated for 72 h at pH 9.0 in aerated water.

The optical and SEM micrographs of one of the focal point areas of the concentric-formed purple islands are presented in **Figure 4.14**. The SEM images show that the surface in

the centre of the focal area is highly etched and contains etched  $\text{Cu}_2\text{O}$  crystals with aggregates of small particles on top. The colour of the island shows that an array of different colours spread radially. The centre of the island has a mixture of green, purple, and red, but the colour changes to yellow and then green as the concentric ring area moves away from the centre. The yellow colour in the inner concentric ring and the green colour in the outer concentric ring are uniformly distributed over the small  $\text{Cu}_2\text{O}$  particles. Copper metal is yellow,  $\text{Cu}_2\text{O}$  ranges from red to magenta, while  $\text{Cu}(\text{OH})_2$  is blue. The pattern of the colour of the focal area suggests that the  $\text{Cu}_2\text{O}$  particles may disproportionate to  $\text{Cu}^0$  and  $\text{Cu}^{\text{II}}$  species and the momentum from the reaction have carried them radially away from the centre, with the soluble  $\text{Cu}^{\text{II}}$  species ( $\text{Cu}^{2+}$  and  $\text{Cu}(\text{OH})^+$ ) transported further away than the metallic copper species.



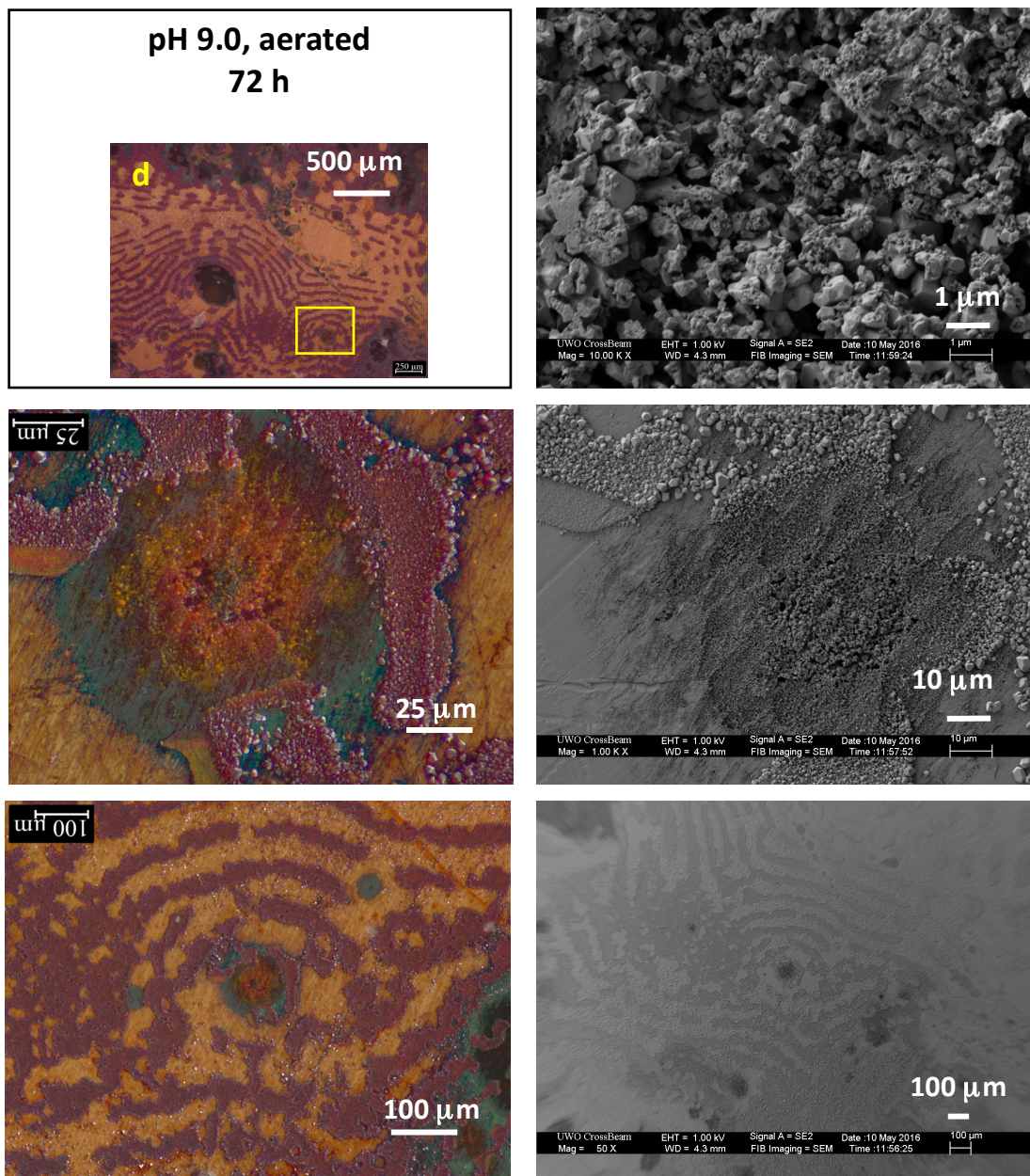


**Figure 4.14:** Optical and SEM micrographs with different magnifications of a focal area of the purple concentric crescent islands on a Cu coupon irradiated for 72 h at pH 9.0 in aerated water.

The magenta coloured areas represent high-density areas of large  $\text{Cu}_2\text{O}$  crystals. As the gap between the magenta coloured islands become wider, the colour between the gap changes from blue, green, yellow to light yellow (**Figure 4.15**). Comparison with the SEM of these areas

shows that the colour change observed in the optical micrographs correlates well with the size and the density of  $\text{Cu}_2\text{O}$  crystals; magenta to the high-density area of large  $\text{Cu}_2\text{O}$  crystals, blue to the high-density of medium sized  $\text{Cu}_2\text{O}$  crystals, green to the area consisting of a thin layer of a mixture of  $\text{Cu}(\text{OH})_2$  gel and small  $\text{Cu}_2\text{O}$  particles, and yellow and light yellow to a thin layer of amorphous  $\text{Cu}_2\text{O}/\text{Cu}(\text{OH})_2$  (based on the XPS analysis to be published elsewhere). The optical and SEM micrographs show the clear progression of 'redox-cycle assisted' ripening of  $\text{Cu}_2\text{O}$  crystals in the gaps. As the gap between the magenta islands widens, more underlying surface areas are exposed. The underlying surfaces are very smooth, smoother than the freshly polished surface. These observations suggest that the smooth surfaces between the high crystal-density islands are a result of dissolution of the  $\text{Cu}_2\text{O}$  crystals that have grown earlier.

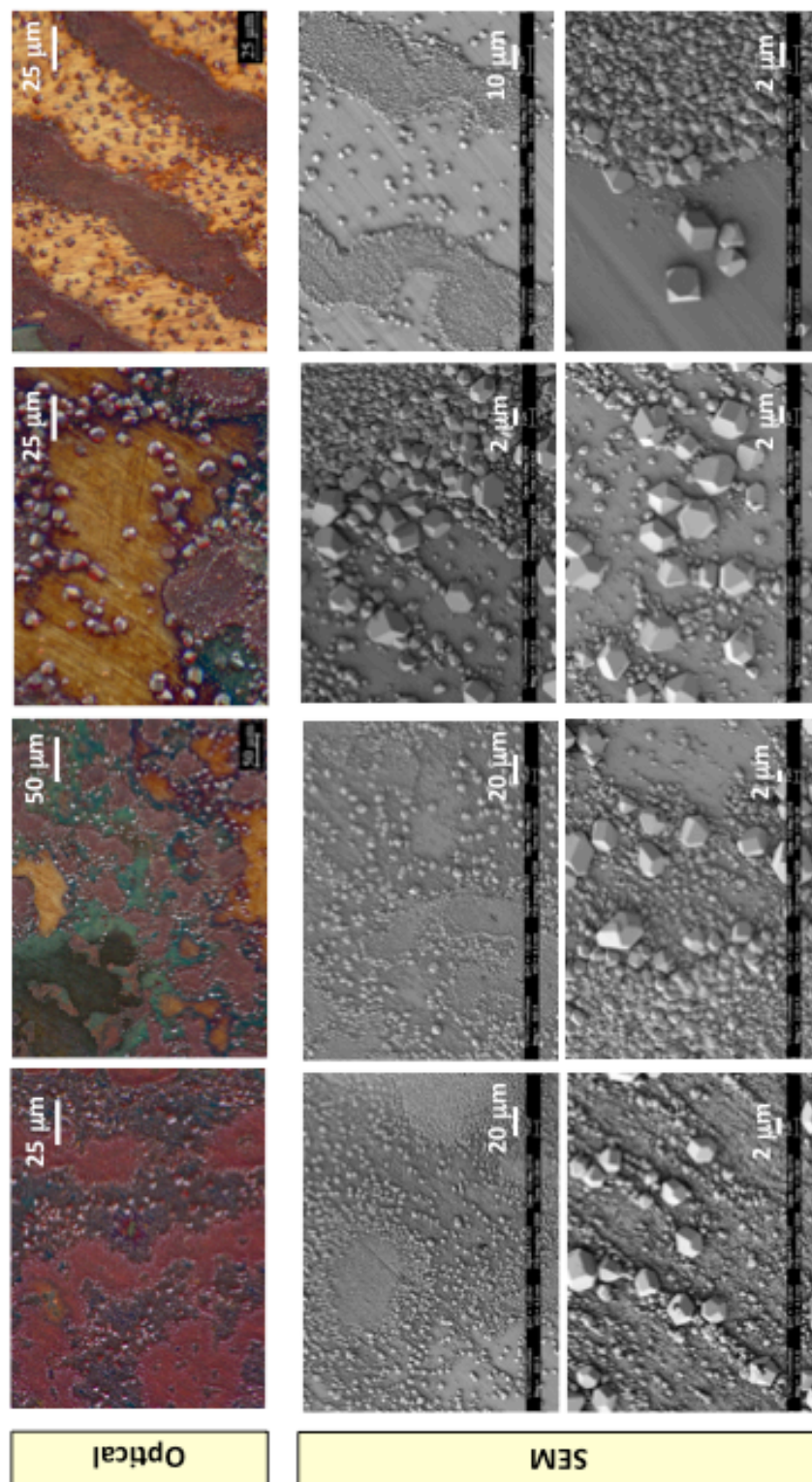


**Figure 4.15:** Optical and SEM micrographs of areas showing different stages of progression to the formation of well-separated concentric crescent islands on a Cu coupon irradiated for 72 h at pH 9.0 in aerated water.

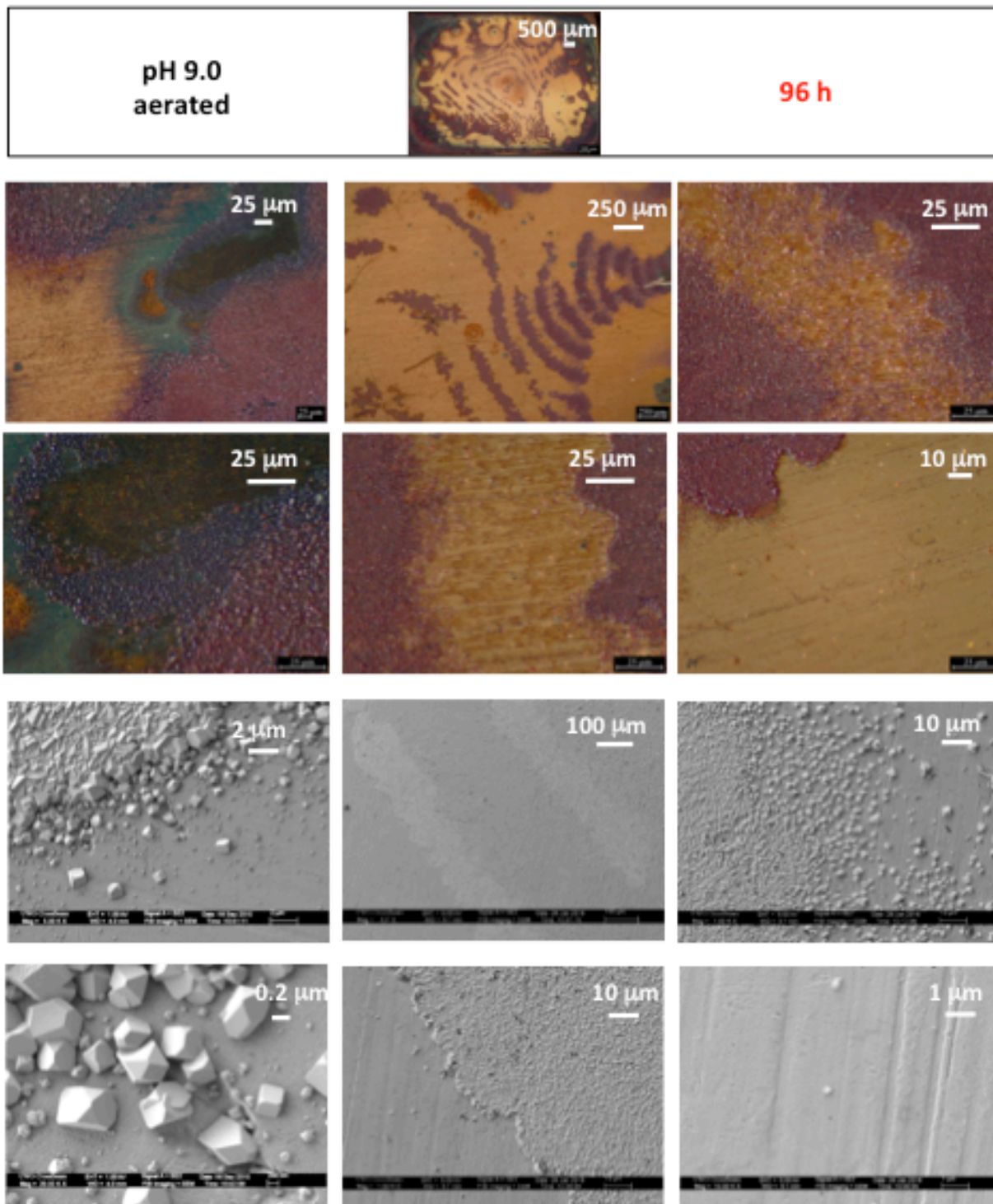


**Figure 4.16:** Optical and SEM micrographs of the surface of a Cu coupon irradiated for 96 h at pH 9.0 in aerated water.

The coupon corroded for 96 h shows mostly the concentric arc-shaped islands of densely packed  $\text{Cu}_2\text{O}$  crystals on the very smooth underlying surface (**Figure 4.16**). The density of these islands is much smaller than that observed on the coupon corroded for 72 h, indicating that while ‘redox-cycle assisted’ ripening due to the dissolution and reprecipitation of  $\text{Cu}_2\text{O}$  crystals continues at longer times, the net effect is the dissolution of the  $\text{Cu}_2\text{O}$  crystals that have grown earlier.

The progression of the underlying surface can be better appreciated from the SEM micrographs of the FIB-cut cross sections across the boundaries of high and low  $\text{Cu}_2\text{O}$  crystal density areas on the coupons corroded for different durations (**Figure 4.17**). The cross section views demonstrate that the oxide particles/crystals dissolve with time, and that the boundaries between the inner oxide layer and the outer oxide crystal layer, and between the oxide layers and the substrate metal becomes smoother with time.

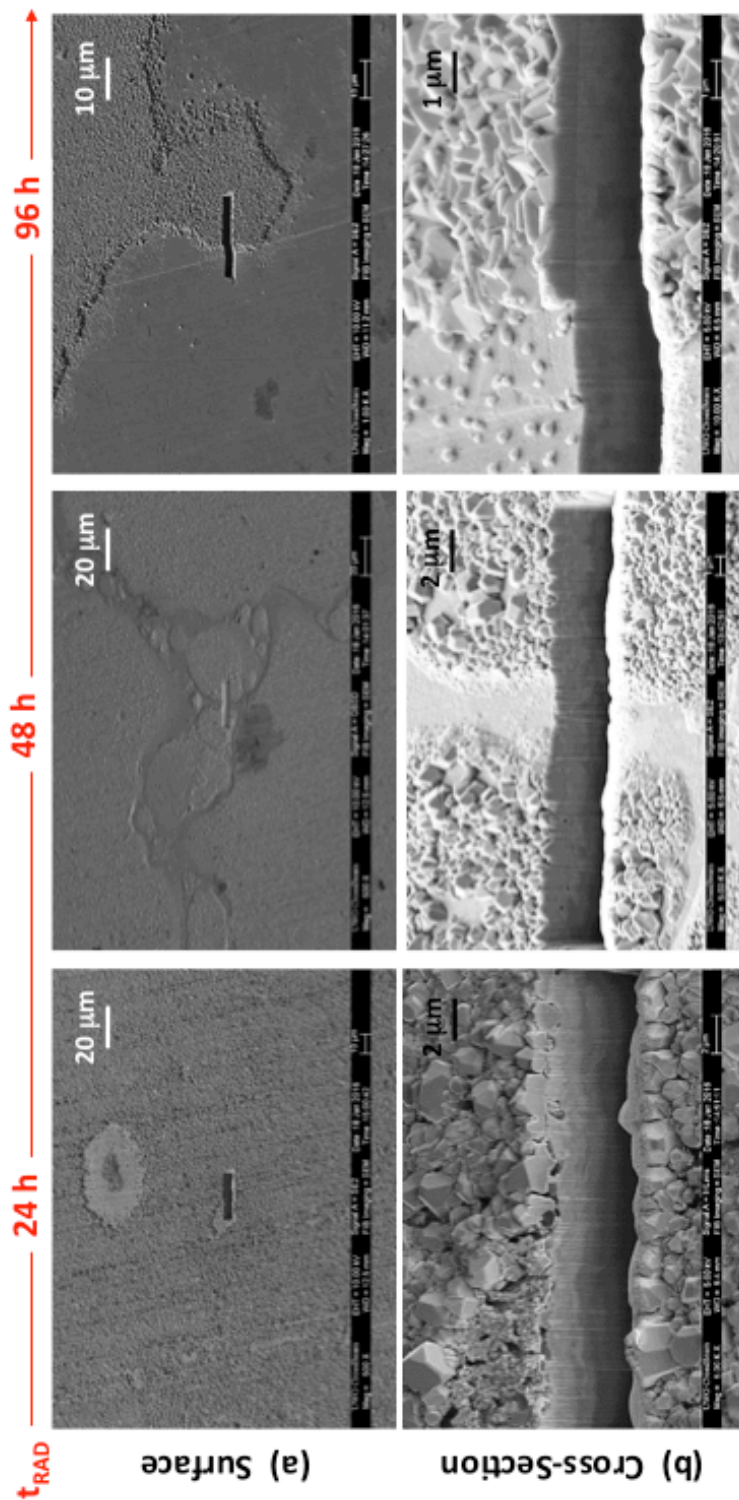


**Figure 4.17:** SEM micrographs of the surfaces and the FIB-cut cross sections of Cu coupons corroded for different durations at pH 9.0 in aerated water in the presence of  $\gamma$ -radiation at  $3 \text{ kGy}\cdot\text{h}^{-1}$ .

#### 4.4 Summary

The evolution of surface and oxide particle morphologies during water droplet corrosion of copper metal in the presence of  $\gamma$ -radiation was investigated. Raman and XRD analyses found that the particles formed on copper coupon surfaces are mainly  $\text{Cu}_2\text{O}$ . However, optical and SEM micrographs showed that the morphologies of the oxide particles and the underlying surface change as corrosion progresses. Oxide formation at any given time during water droplet corrosion is not uniform across the surface of a copper coupon, and the surface morphologies of different areas evolve differently. As different areas evolve at different rates, the individual areas undergo distinct stages of oxide formation and growth. At early stages,  $\text{Cu}_2\text{O}$  particles form preferentially along polishing lines. The oxide particles also form earlier and grow faster and larger in the outer region (defined by the droplet on the coupon surface) than in the inner region. The crystals that form earlier grow larger over the same growth period, and the density, size and morphology of the  $\text{Cu}_2\text{O}$  crystals change with time within different regions. Another interesting observation was the development of circular oxide islands at longer irradiation times. Narrow channels surrounded the oxide islands, in which larger  $\text{Cu}_2\text{O}$  crystals that had formed earlier have begun dissolving. Based on the observed  $\text{Cu}_2\text{O}$  formation and growth we have proposed a mechanism for water droplet corrosion of copper, which is discussed in Chapter 6.

#### 4.5 References

1. M. Balkanski, M.A. Nusimovici, J. Reydelle, *Solid State Comm.*, **1969**, 7, 815-818.
2. J.C. Hamilton, J.C. Farmer, R.J. Anderson, *J. Electrochem. Soc.*, **1986**, 739-745.
3. M. Naghizadeh, A.M. Jean, G. Whitaker, J.M. Joseph, J.C. Wren, *manuscript prepared for publication*, 2017.
4. S. Budavari, *The Merck Index - An Encyclopedia of Chemicals, Drugs, and Biologicals*, Merck and Co. Inc., Whitehouse Station, NJ, **1996**, 446-448.
5. K. Chen, C. Sun, S. Song, D. Xue, *Cryst. Eng. Comm.*, **2014**, 16, 5257-5267.
6. C.H. Kuo, M.H. Huang, *Nano Today*, **2010**, 2, 106.
7. L. Huang, F. Peng, H. Yu, H. Wang, *Mater. Res. Bull.*, **2008**, 43(11), 3047-3053.
8. J. Zhu, Y. Wang, X. Wang, X. Yang, L. Lu, *Powder Technol.*, **2008**, 181(3), 249-254.
9. J. Zhu, H. Bi, Y. Wang, X. Wang, X. Yang, L. Lu, *Mater. Lett.*, **2008**, 62(14) 2081-2083.
10. P. He, X. Shen, H. Gao, *J. Colloid Interface Sci.*, **2005**, 284(2) 510-515.
11. Y. Sui, W. Fu, H. Yang, Y. Zeng, Y. Zhang, Q. Zhao, Y. Li, X. Zhou, Y. Leng, M. Li, G. Zou, *Cryst. Growth Des.*, **2010**, 10(1), 99-108.
12. Y. Shang, L. Guo, *Adv. Sci.*, **2015**, 2, 1-22.
13. X. Zhang, Z. Cui, *Mater. Sci. Eng. B.*, **2009**, 162(2), 82-86.
14. G. Liu, J.C. Yu, G.Q. Lu, H.M. Cheng, *Chem. Commun.*, **2011**, 47, 6763-6783.
15. Y. Fukamori, M. Konig, B. Yoon, B. Wang, F. Esch, U. Heiz, U. Landman, *ChemCatChem*, **2013**, 5, 3330-3341.
16. M. Naghizadeh, A.M. Jean, G. Whitaker, J.M. Joseph, J.C. Wren, *to be submitted to Journal of Electrochemical Society*. 2017.



## Chapter 5

### Evolution of Surface Morphology During Corrosion of Circular Copper Coupons Under 50 $\mu\text{L}$ Water Droplets

#### 5.1 Introduction

The effect of water droplet pH on the evolution of surface morphology during corrosion of copper in the presence of  $\gamma$ -radiation was investigated using a water volume of 50  $\mu\text{L}$  on circular coupons with surface areas of 0.785  $\text{cm}^2$ . The water droplets spread to the edges of the coupons, covering the entire surface of these coupons and forming dome shapes, as shown in **Figure 5.1**. The kinetics of copper corrosion at two different pHs (6.0 and 9.0) were investigated by following the changes in surface morphology and dissolved copper concentration in the water droplet as a function of time.



**Figure 5.1:** A 50  $\mu\text{L}$  water droplet on the surface of a circular copper coupon.

#### 5.2 Experimental Details

The test sample preparation and procedure used in this study were the same as those used for the study using rectangular coupons described in Chapter 4. The main differences were that

the coupons used in this study are circular coupons with surface areas of  $0.785 \text{ cm}^2$ , the water droplet volume was  $50 \text{ }\mu\text{L}$ , and the radiation dose rate was  $2.8 \text{ kGy}\cdot\text{h}^{-1}$ .

After exposure, the coupons were rinsed with pure water to remove the droplet solution and this rinse was collected for trace copper analysis by ICP-MS. Coupons were then dried with argon and imaged using a digital microscope (Leica DVM 6A) and SEM (Zeiss LEO 1540XB) as described in Chapter 3.

## 5.3 Results and Discussion

### 5.3.1 Overall Progression of Copper Corrosion

**Figure 5.2** shows the low magnification optical micrographs of the entire surface areas of coupons corroded in aerated solutions for different durations at two different initial pHs (6.0 and 9.0). As observed with  $200 \text{ }\mu\text{L}$  water droplets on rectangular copper coupons (Chapter 4), the optical micrographs clearly demonstrate that oxide formation is not uniform on the surface. Differently coloured areas develop and evolve in a series of quasi-concentric rings as corrosion progresses. These areas can be categorized into two broad regions for their morphological evolution characteristics: the inner circle and the outer ring. Local variation within these two broad regions is also observed.

The dissolved copper concentrations in the water droplets from these experiments were measured by ICP-MS, and these results are presented in **Table 5.1** and **Figure 5.3**. In the early stages of corrosion (shorter than 36 h at pH 6.0 and 48 h at pH 9.0), dissolved [Cu] increases nearly linearly with time at a rate of  $\sim 0.1 \text{ mM/h}$ , and the rate of increase in dissolved [Cu] is nearly independent of initial pH. (In comparison, the initial rate of copper dissolution in aerated or deaerated water droplets containing  $5 \text{ mM H}_2\text{SO}_4$  (initial pH 2.0) in the absence of radiation

was 3 mM/h [1].) During the period of linear increase of dissolved [Cu], particle formation in the inner circle region is negligible with no crystalline Cu<sub>2</sub>O particles present, while the outer circular ring region undergoes more significant morphological changes (**Figure 5.2**).

At longer times, the dissolved [Cu] increases at an accelerated rate before it reaches a constant value. The steady state is reached at a slightly later time at pH 9.0 than at pH 6.0. However, the steady-state concentration reached is 11 mM, independent of initial pH. The onset of the acceleration in copper dissolution coincides with the onset of the growth of granular oxide particles in the inner region (see SEM micrographs presented later). The growth of Cu<sub>2</sub>O particles in the inner region continues while the dissolved [Cu] remains nearly constant (**Figure 5.2**). At times longer than 72 h, the boundaries between the inner and outer regions become more diffuse.

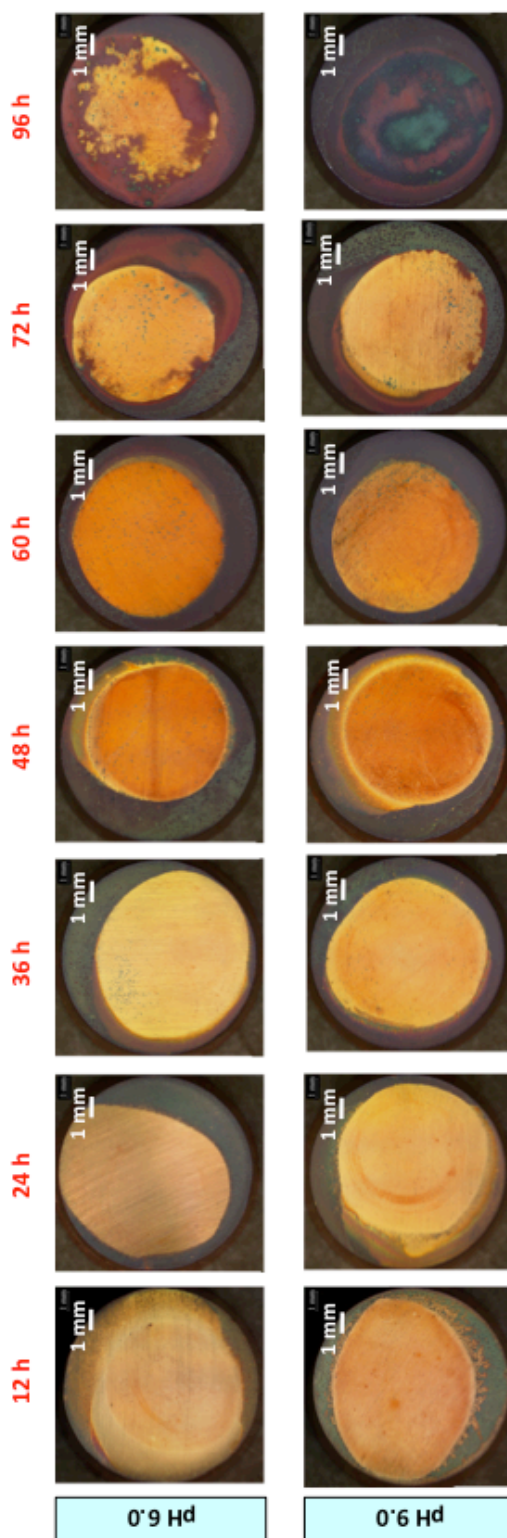


**Figure 5.2:** Optical micrographs of the entire surfaces of circular Cu coupons corroded in 50  $\mu\text{L}$  aerated water droplets at initial pH 6.0 or pH 9.0 for different durations in the presence of  $\gamma$ -radiation at dose rate of  $2.8 \text{ kGy}\cdot\text{h}^{-1}$ .

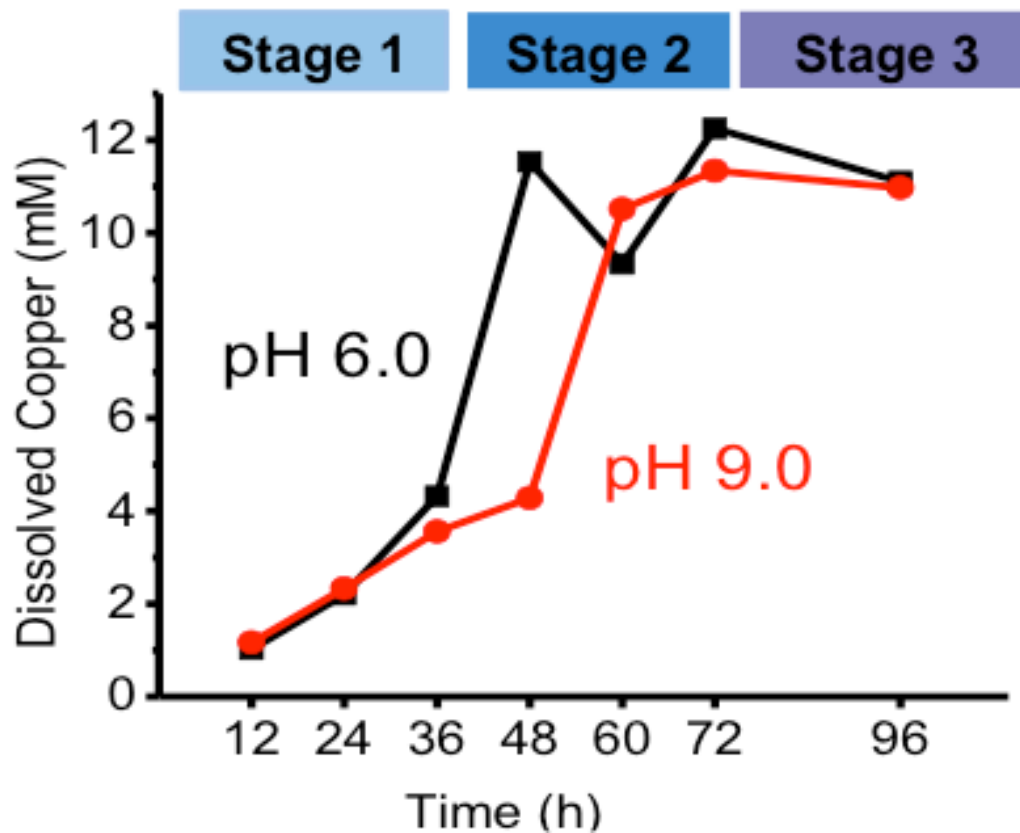


**Figure 5.3:** Concentration of copper species dissolved in the water droplets from the coupons whose optical micrographs are shown in **Figure 5.2**.

pH	Irradiation Time (h)	Dissolved [Cu] (mM)
6	12	1.02
6	24	2.20
6	36	4.32
6	48	11.53
6	60	9.33
6	72	12.25

6	96	11.10
9	12	1.17
9	24	2.33
9	36	3.56
9	48	4.28
9	60	10.51
9	72	11.34
9	96	10.97

**Table 5.1:** Values of the concentrations of copper species dissolved in the water droplets from the coupons whose optical micrographs are shown in **Figure 5.2**.

Combination of the morphological evolutions of different regions (**Figure 5.2**) and the evolution of dissolved copper concentration in the water droplets (**Figure 5.3**) indicates that corrosion of a circular copper coupon under a 50  $\mu\text{L}$  water droplet occurs in three distinct kinetic stages, in a similar manner to that observed for 200  $\mu\text{L}$  droplets on rectangular coupons, as described in Chapter 4. As observed for the rectangular coupons, the copper corrosion in the inner and outer regions evolves at different rates. This study shows that the duration of each stage also depends on the initial pH of the water droplet.

The main corrosion process at early times (**Stage 1**) is the oxidation of  $\text{Cu}^0_{(m)}$  to  $\text{Cu}^{2+}_{(aq)}$ . As the solution near the surface becomes saturated, the oxidation of  $\text{Cu}^0_{(m)}$  results primarily in the growth of  $\text{Cu}_2\text{O}$  particles (**Stage 2**). After the surface is covered by a compact layer of large  $\text{Cu}_2\text{O}$  crystals, the oxidation of the underlying metal substrate becomes negligible, while redox-cycle-assisted ripening of the  $\text{Cu}_2\text{O}$  crystals grown earlier occurs at a substantial rate and

changes the surface morphology considerably (**Stage 3**). More details are discussed in Chapter 6, describing the proposed mechanism of  $\text{Cu}_2\text{O}$  crystal growth.

### 5.3.2 Surface Variation in Corrosion Progression

Different areas on a copper coupon under a water droplet corrode at different rates, which results in non-uniformity of the oxide growth across the surface with time. This phenomenon is illustrated using the optical and SEM micrographs of the surface of a coupon corroded for 36 h at pH 9.0 in **Figures 5.4** and **5.5**. The optical and SEM micrographs presented in **Figure 5.4** show that the inner circle area (1) consists of very small (a few nm) granular particles sparsely distributed over the underlying very smooth surface (the polishing lines no longer show the sharp edges). The dark purple area (2) near the edge of the coupon consists of densely packed  $\text{Cu}_2\text{O}$  crystals with well-defined facets, and the area near the edge in the other side (area 3) consists of large dark purple to dark blue islands in the pool of green. The green deposits appear to be a gel-like layer of  $\text{Cu}(\text{OH})_2$  deposited on top of the  $\text{Cu}_2\text{O}$  oxide islands. [2]

The surface and particle morphologies of these areas are consistent with the main kinetic processes proposed to occur in different stages of corrosion. In area (1) corrosion is still in Stage 1, where the overall copper corrosion leads mainly to the production of  $\text{Cu}^{2+}_{(\text{aq})}$ . The densely packed  $\text{Cu}_2\text{O}$  crystals in area (2) indicate that corrosion in this area has progressed well into Stage 2 where the predominant effect of oxidation of  $\text{Cu}^0_{(\text{m})}$  is to grow  $\text{Cu}_2\text{O}$  crystals. In area (3) corrosion has progressed to Stage 3 where net oxidation of  $\text{Cu}^0_{(\text{m})}$  is negligible and redox-cycle-assisted ripening becomes the dominant process determining the morphological evolution of the surface.

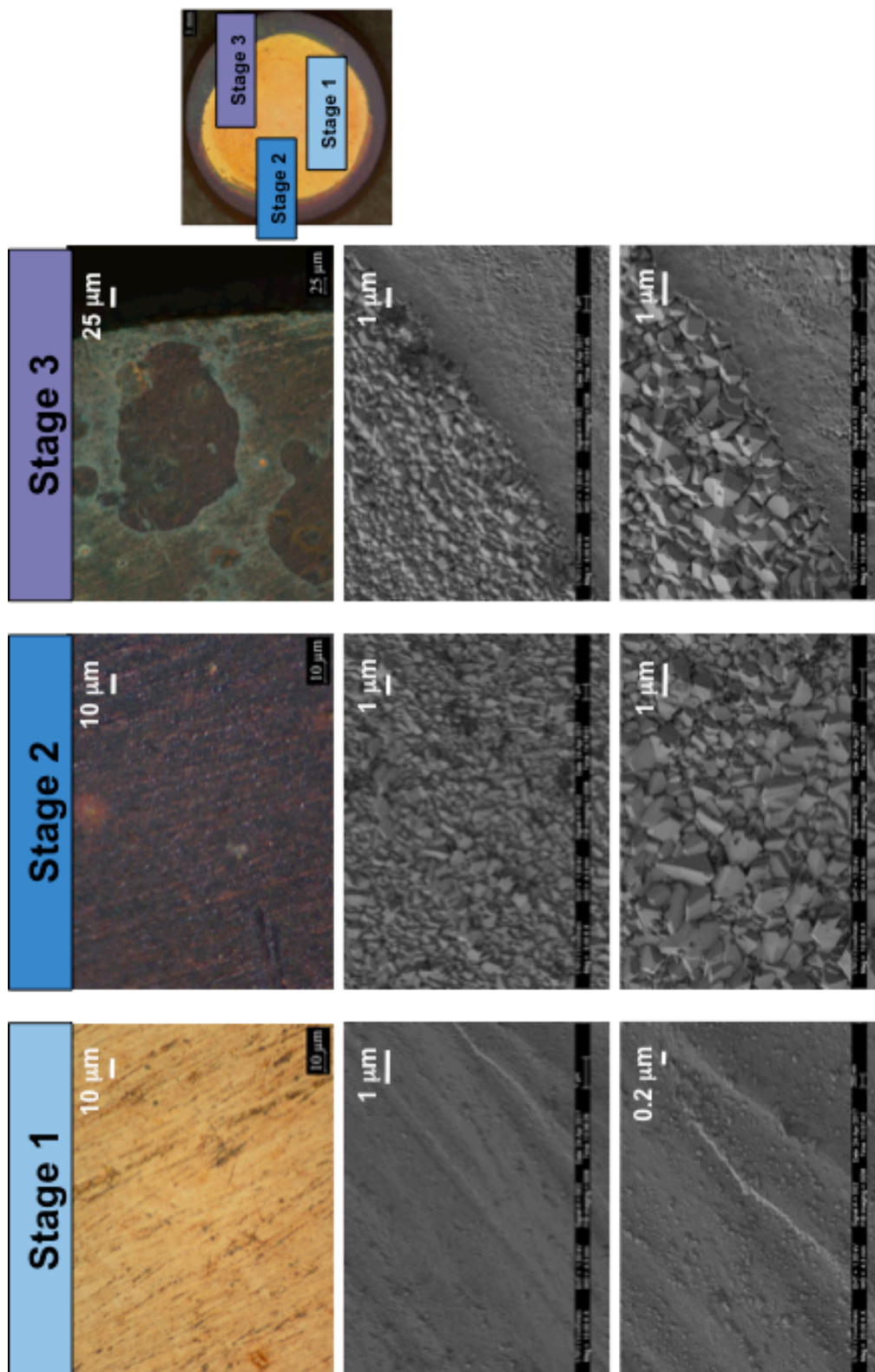


**Figure 5.4:** Optical and SEM micrographs of areas of different corrosion progressions on a circular Cu coupon corroded for 36 h in a 50  $\mu\text{L}$  aerated water droplet at pH 9.0 in the presence of  $\gamma$ -radiation at a dose rate of  $2.8 \text{ kGy}\cdot\text{h}^{-1}$ .



The optical and SEM micrographs of the boundary region between area (1) and area (2) on the same coupon are presented in **Figure 5.5**. The morphological evolution at the boundary demonstrates  $\text{Cu}_2\text{O}$  crystal growth by the ‘redox-cycle-assisted ripening’ mechanism. The SEM images show that crystals grown earlier dissolve with time to form smooth channels between the oxide islands. The thin arc-shaped island (marked x) consists of red and green coloured areas. Comparison of the optical and SEM micrographs indicates that the red colour corresponds to the area containing individual  $\text{Cu}_2\text{O}$  crystal particles of tens of nm in size, while the green colour corresponds to the area where particles are under the blanket of a gel layer and have not yet fully crystallized. The red particles are attributed to  $\text{Cu}_2\text{O}$  while the green gel-like deposits are attributed to  $\text{Cu}(\text{OH})_2$ , based on comparison of the XPS and optical micrographs of numerous areas (these results are not presented here but will be published elsewhere in the near future).

The area marked (y), further towards the edge of the coupon before transitioning to the purple area, also consists of green and red areas. The green gel layer formed in area (y) has a wider spread than in area (x). Under the thin blanket of the green layer there are small dark brown circular islands encircled by orange rings. The SEM micrographs of this area show that the dark brown islands consist of densely packed, large (a few  $\mu\text{m}$ )  $\text{Cu}_2\text{O}$  crystals, the orange rings consist of partially dissolved  $\text{Cu}_2\text{O}$  crystals, and the outer green areas consist of smaller individual  $\text{Cu}_2\text{O}$  crystals. The shapes of the  $\text{Cu}_2\text{O}$  crystals in the dark brown islands are mostly truncated cubes and are not as fully developed as those seen in area 3 in **Figure 5.4**. The observations of the particle morphology are consistent with the ‘redox-cycle-assisted’ crystal growth mechanism proposed for  $\text{Cu}_2\text{O}$  growth in Stage 2.

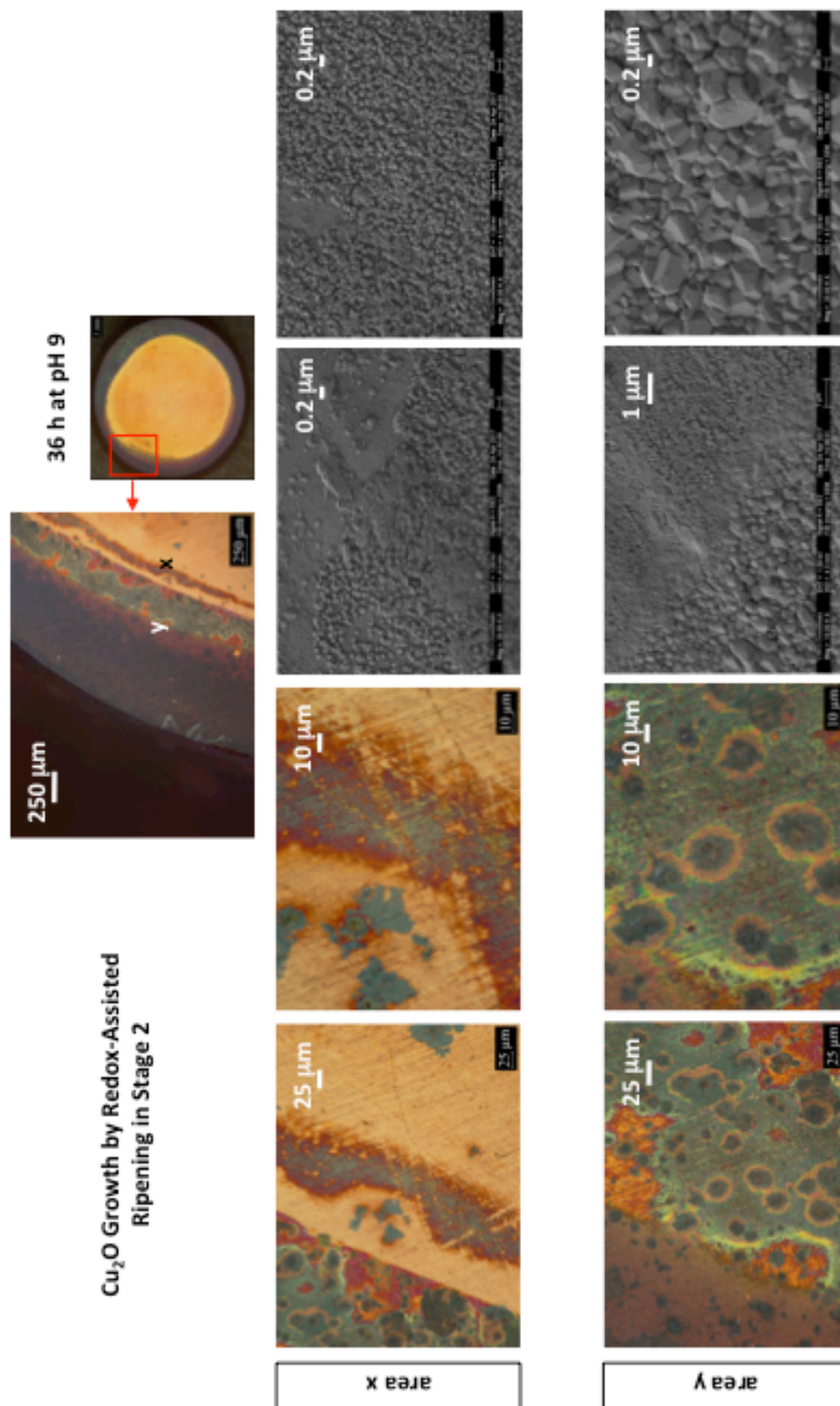


**Figure 5.5:** Optical and SEM micrographs of the area marked as Stage 1 on the optical micrograph shown in **Figure 5.4**.

### 5.3.3 Corrosion Progression of Different Areas

Because different areas progress at different rates, the effect of pH on copper corrosion was investigated by following the morphology progression in different regions separately. The optical micrographs of the central areas of the coupons corroded for different durations are presented in **Figure 5.6**. At both pHs the surface of the central region becomes smoother and its colour becomes more washed out (or light) yellow with time at early stages of corrosion (less than 36 h). Over this duration the rate of morphological evolution is similar at both pHs. The XPS analysis of corroded copper coupons suggests that the light-yellow area corresponds to a thin layer of  $\text{Cu}(\text{OH})_2$  on copper metal [1] (it may also contain a thin layer of  $\text{Cu}_2\text{O}$ ). Over the same duration  $[\text{Cu}^{2+}_{(\text{aq})}]$  increases linearly with time and the rate of increase is also the same at both pHs (**Figure 5.3**).

The observed evolution of surface morphology is consistent with the corrosion mechanism proposed for Stage 1, where the dominant process controlling the overall metal oxidation is the oxidation of  $\text{Cu}^0_{(\text{m})}$  (via  $\text{Cu}^{\text{I}}_{(\text{ad})}$ ) to  $\text{Cu}^{\text{II}}_{(\text{ad})}$  which is then hydrated and diffuses into the solution phase). While diffusing into the solution phase the cupric ions undergo hydrolysis reactions to form  $\text{Cu}(\text{OH})_2$  [3]. The evolution rate of surface morphology and  $[\text{Cu}^{2+}_{(\text{aq})}]$  are nearly independent of initial pH, and this also suggests that the rate of overall oxidation of  $\text{Cu}^0_{(\text{m})}$  in Stage 1 is not sensitive to pH, but depends more strongly on the rate of interfacial charge transfer under the studied conditions. Under irradiation conditions, the interfacial charge transfer rate may be limited by the overall radiolytic production rate of the oxidant  $\text{H}_2\text{O}_2$  in solution. [4]

At longer times ( $> 48$  h) the surface morphologies of the central areas on the coupons corroded at different pHs diverge increasingly with time. The surface of the wider inner circle

region on coupons corroded for 48 h at either pH 6.0 or 9.0 is uniformly covered with a dark orange oxide layer (**Figure 5.2**). The dark orange colour indicates the presence of a layer of small granular  $\text{Cu}_2\text{O}$  particles. After 48 h the colour of the central area (**Figure 5.6**) progresses from dark orange to light orange or light brown by 72 h, similar to the progression observed in Stage 1. Over the same duration the wider inner circle region (**Figure 5.2**) shows green  $\text{Cu}(\text{OH})_2$  deposits. **Figures 5.2** and **5.6** indicate that the central region is still at an early stage of  $\text{Cu}_2\text{O}$  particle growth (or the beginning of Stage 2) at 72 h, while the area near the boundary between the inner circle and the outer ring regions is well into Stage 2. The wider inner circle area in Stage 2 after 48 h is consistent with the observation of constant  $[\text{Cu}^{2+}_{(\text{aq})}]$  with time after 48 h. At 96 h the redox-cycle-assisted ripening has spread from the outer ring region to the inner circle region. This spread is faster at pH 9.0.

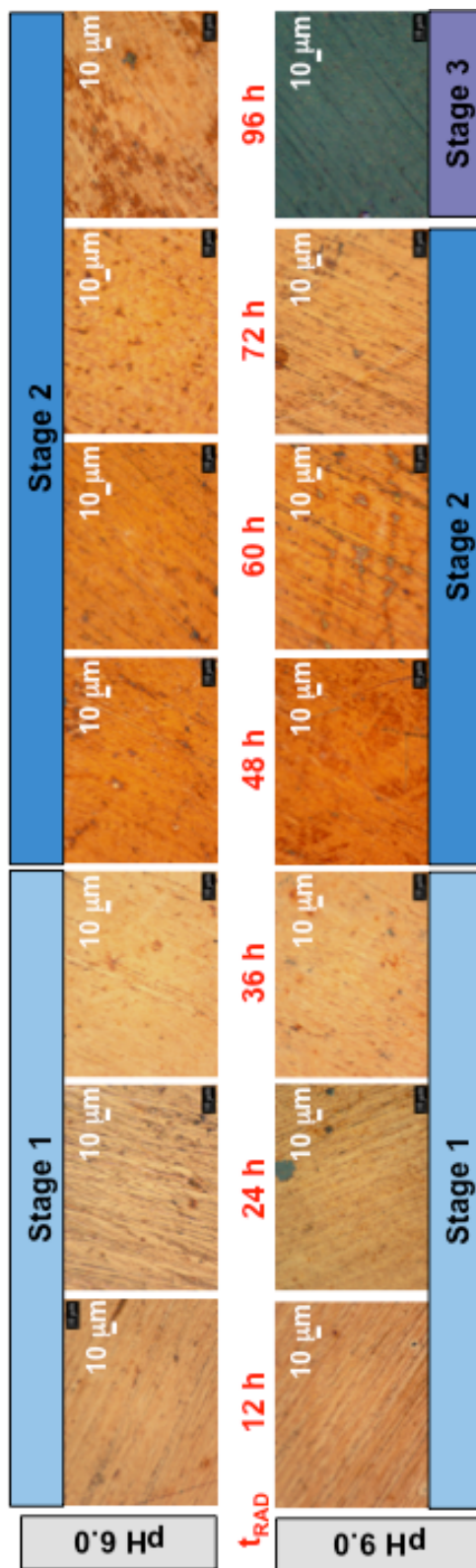


**Figure 5.6:** Optical micrographs of the central areas of the coupons corroded for different durations at pH 6.0 and 9.0 at a dose rate of 2.8 kGy·h<sup>-1</sup>.

The solution pH has a stronger effect on the evolution of surface morphology of the outer ring region than on that of the inner circle region. The formation of hydroxide and oxide deposits is faster in the outer region than in the inner circle region. **Figure 5.7** shows the optical micrographs of the most progressed areas in the outer ring region. The corrosion in the outer ring region has already progressed to Stage 2 by 12 h. The most progressed areas show dark brown circular islands of  $\text{Cu}_2\text{O}$  crystals in the pool of green  $\text{Cu}(\text{OH})_2$  gel, consistent with the mechanism proposed for  $\text{Cu}_2\text{O}$  particle growth in Stage 2. As corrosion progresses in Stage 2 the green areas merge and spread laterally while some of the dark brown circular islands grow larger while smaller islands dissolve, consistent with the proposed 'redox-cycle-assisted' growth and ripening mechanism. Although considerable ripening of  $\text{Cu}_2\text{O}$  crystals is taking place in most of these areas, the overall amount (combination of density and thickness) of  $\text{Cu}_2\text{O}$  is increasing with time until about 48 h. At 60 h, purple areas develop in the outer ring region (**Figure 5.2**). The purple areas consist of densely packed large  $\text{Cu}_2\text{O}$  crystals.

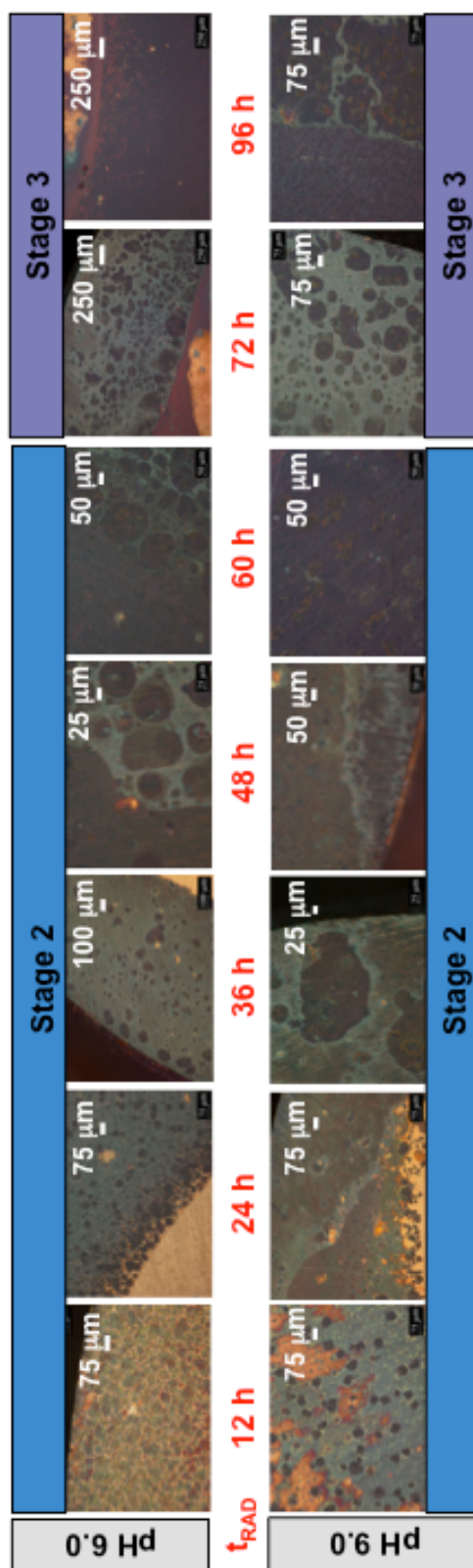


**Figure 5.7:** Optical micrographs of outer ring regions of the coupons corroded for different durations at pH 6.0 and 9.0 at a dose rate of  $2.8 \text{ kGy}\cdot\text{h}^{-1}$ .

At longer times the colour of some areas in the outer ring region changes from purple to magenta while the other areas exhibit morphology consisting of dark purple circular islands in the pool of green (**Figures 5.7 and 5.2**). The size of the dark purple islands increases with time and the boundary between the inner circle and the outer ring regions becomes more diffuse with time (**Figure 5.2**). The observed evolution indicates that the corrosion in the outer region has progressed to Stage 3 where the net metal oxidation is negligible and the redox-cycle-assisted ripening of  $\text{Cu}_2\text{O}$  crystals become the dominant process.

#### 5.4 Summary

Water droplet corrosion of copper in the presence of a continuous flux of  $\gamma$ -radiation was investigated by exposing copper metal to a limited volume water droplet as a function of irradiation time at two different pHs. The oxide growth kinetics were studied by measuring the amount of dissolved copper in the droplet as a function of time, as well as by analyzing the morphology of the oxide formed on coupon surface as a function of time.

The evolution of the surface and oxide particle morphologies observed in this study is similar to that observed in the earlier study using 200  $\mu\text{L}$  water droplets on rectangular coupons presented in Chapter 4. At either pH 6.0 or 9.0, oxide formation at any given time during water droplet corrosion is not uniform across the surface of a copper coupon, and the surface morphologies of different areas evolve differently. Different areas evolve at different rates and the individual areas undergo distinct stages of oxide formation and growth. The outer regions of the droplet progress faster than the inner circle region of the droplet for both cases.

The dissolved copper concentration and surface morphology observed as a function of time indicate that water droplet corrosion of copper in the presence of  $\gamma$ -radiation occurs in three



stages. Stage 1 involves the radiolytic oxidation of  $\text{Cu}^0_{(m)}$  to  $\text{Cu}^{2+}_{(aq)}$ . The growth of  $\text{Cu}_2\text{O}$  particles occurs in Stage 2 as the solution near the surface becomes supersaturated with  $\text{Cu}^{2+}_{(aq)}$ . Stage 3 occurs after the surface is covered by a compact oxide layer. During this stage the oxidation of the underlying metal substrate becomes negligible while the  $\text{Cu}_2\text{O}$  crystals grown earlier undergo redox-cycle-assisted ripening.

This study shows that the duration of each stage depends not only on the water layer thickness but also on the solution pH. The initial pH of water droplet has negligible effect on the corrosion kinetics in Stage 1. However, under the stagnant water droplet conditions, the solution in the outer region is where the water layer is thinner and hence becomes saturated earlier. The outer ring region reaches Stage 2 much earlier than the inner circle region. The solution pH has a stronger effect on  $\text{Cu}_2\text{O}$  crystal growth and ripening in Stage 2 and Stage 3. The progression through the kinetic stages is slower in the inner circle region than in the outer region, and slower at pH 6.0 than at pH 9.0.

A mechanism describing the kinetic stages of the oxide growth observed in this study as well as the results in Chapter 4 is presented in the following chapter.

## 5.5 References

1. M. Naghizadeh, A.M. Jean, G. Whitaker, J.M. Joseph, J.C. Wren, *to be submitted to Journal of Electrochemical Society*. 2017.
2. H.W. Richardson, *Handbook of Copper Compounds and Applications*, Marcel Dekker, Inc., New York, 1997.
3. C.F. Baes, R.E. Mesmer, *Hydrolysis of Cations*, 2nd Ed, Krieger Pub. Co., Malabar, Florida, 1986.
4. A. Björkbacka, M. Yang, C. Gasparini, C. Leygraf, M. Jonsson, *Dalton Trans.*, **2015**, 44, 16045-16051.

## Chapter 6

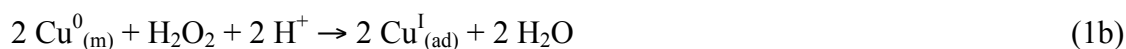
### Mechanism of Cu<sub>2</sub>O Formation and Growth During Water Droplet Corrosion of Copper

The studies described in the previous two chapters have demonstrated that water droplet corrosion of copper in the presence of  $\gamma$ -radiation occurs in three stages. Stage 1 involves the radiolytic oxidation of Cu<sup>0</sup><sub>(m)</sub> to Cu<sup>2+</sup><sub>(aq)</sub>. The growth of Cu<sub>2</sub>O particles occurs in Stage 2 as the solution near the surface becomes supersaturated with Cu<sup>2+</sup><sub>(aq)</sub>. Stage 3 occurs after the surface is covered by a compact oxide layer. During this stage the oxidation of the underlying metal substrate becomes negligible while the Cu<sub>2</sub>O crystals grown earlier undergo redox-cycle-assisted ripening. Based on the observed Cu<sub>2</sub>O formation and growth we have proposed a mechanism for water droplet corrosion of copper in the presence of  $\gamma$ -radiation, which is discussed in this chapter.

#### 6.1 Proposed Mechanism of Water Droplet Corrosion of Copper

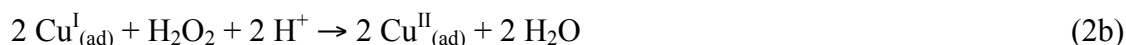
##### **Stage 1:**

In Stage 1 the copper metal surface is not yet covered with oxides and the solution near the surface is not yet saturated with copper ions. In this kinetic stage, the first step is the oxidation of Cu<sup>0</sup><sub>(m)</sub> to Cu<sup>I</sup><sub>(ad)</sub> coupled with the reduction of solution species (O<sub>2</sub> and H<sub>2</sub>O<sub>2</sub> in the presence of  $\gamma$ -radiation):



where the subscripts (m) and (ad) represent the metal and adsorbed phases, respectively.

The standard reduction potentials reported for redox reactions between metallic copper and cuprous species ( $\text{Cu}^0 \rightleftharpoons \text{Cu}^I + e^-$ ) are higher than those between cuprous and cupric species ( $\text{Cu}^I \rightleftharpoons \text{Cu}^{II} + e^-$ ) [1]. This indicates that in an environment where  $\text{Cu}^0_{(m)}$  can oxidize the copper oxidation would not stop at  $\text{Cu}^I$  but continue to  $\text{Cu}^{II}$ :



The copper ions formed at the metal-solution interface can dissolve into the solution phase.

For the copper ions to dissolve, they are first hydrated and can then diffuse away from the surface into the solution. The  $\text{Cu}^{II}_{(ad)}$  is more easily hydrated than  $\text{Cu}^I_{(ad)}$ , forming a 6-coordinated complex with  $\text{H}_2\text{O}$  ( $[\text{Cu} \cdot (\text{H}_2\text{O})_6]^{2+}$ ) [2]:



The coordination with  $\text{H}_2\text{O}$  gives the hexaaquacupric ion its blue colour [3]. The  $\text{Cu}^I_{(ad)}$  formed at the surface may be also hydrated but the solubility of cuprous ion in relatively pure water is 2-3 orders of magnitude lower than cupric ion at pHs below 9 [4-5]. Thus, the hydration of  $\text{Cu}^I_{(ad)}$  is expected to be significantly slower than that of  $\text{Cu}^{II}_{(ad)}$ , and the preferable path for  $\text{Cu}^I_{(ad)}$  is the oxidation to  $\text{Cu}^{II}_{(ad)}$  (reaction 2) over dissolution into the bulk solution.

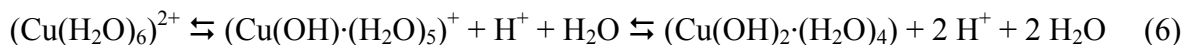
In Stage 1 the concentrations of  $\text{Cu}^I_{(ad)}$  and  $\text{Cu}^{II}_{(ad)}$  quickly reach steady state levels. The predominant corrosion path in Stage 1 is then:



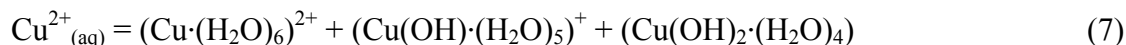
The proposed mechanism for copper corrosion in Stage 1 shows that the concentrations of  $\text{Cu}^{\text{I}}_{(\text{ad})}$  and  $\text{Cu}^{\text{II}}_{(\text{ad})}$  at the metal-solution interface depend on not only the oxidation rates of copper species (reactions 1 and 2), but also on the rates of dissolution of the copper ions (processes 3 and 4). Without the dissolution of  $\text{Cu}^{\text{II}}_{(\text{ad})}$  the rates of the reverse reactions of (1) and (2) would increase with time as the  $\text{Cu}^{\text{I}}_{(\text{ad})}$  and  $\text{Cu}^{\text{II}}_{(\text{ad})}$  accumulate on the surface. The redox equilibria between  $\text{Cu}^0_{(\text{m})}$  and  $\text{Cu}^{\text{I}}_{(\text{ad})}$  and between  $\text{Cu}^{\text{I}}_{(\text{ad})}$  and  $\text{Cu}^{\text{II}}_{(\text{ad})}$  would be established quickly, and the copper corrosion would stop.

### **Transition from Stage 1 to Stage 2:**

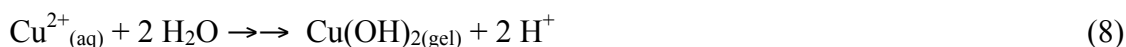
As the hydrated cupric ions diffuse into the solution phase, they are hydrolyzed:



The dissolved cupric species ( $\text{Cu}^{2+}_{(\text{aq})}$ ) thus include:



As  $[\text{Cu}^{2+}_{(\text{aq})}]$  reaches its saturation limit, the neutral hydroxide species then condense as colloidal hydroxide particles and then precipitate as a gelatinous solid hydroxide ( $\text{Cu}(\text{OH})_{2(\text{gel})}$ ):



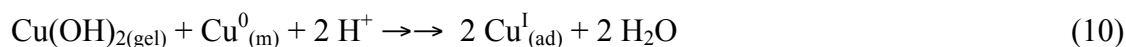
By the end of Stage 1, the concentration of  $\text{Cu}^{2+}_{(\text{aq})}$  reaches its saturation limit. Once the saturation limit is reached, the net production of  $\text{Cu}^{2+}_{(\text{aq})}$  is zero because they are produced via reactions (1) to (5) but also precipitate as solid hydroxide particles via reactions (6) to (8). This is then followed by the reductive conversion of precipitated  $\text{Cu}(\text{OH})_{2(\text{gel})}$  to  $\text{Cu}_2\text{O}_{(\text{cr})}$  in Stage 2.

**Stage 2:**

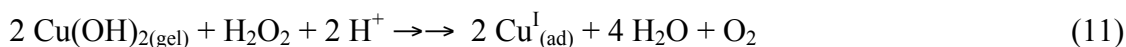
In Stage 2, the  $\text{Cu(OH)}_{2(\text{gel})}$  is continuously produced by the oxidation of  $\text{Cu}^0_{(\text{m})}$  to  $\text{Cu}^{2+}_{(\text{aq})}$  (process 5) followed by the precipitation of  $\text{Cu}^{2+}_{(\text{aq})}$  as  $\text{Cu(OH)}_{2(\text{gel})}$  (process 8). The net production process for  $\text{Cu(OH)}_{2(\text{gel})}$  is then:



On the copper metal surface (as well as on the growing  $\text{Cu}_2\text{O}$  crystals, see below), the cupric hydroxide can reduce to  $\text{Cu}^I_{(\text{ad})}$  by  $\text{Cu}^0_{(\text{m})}$ :



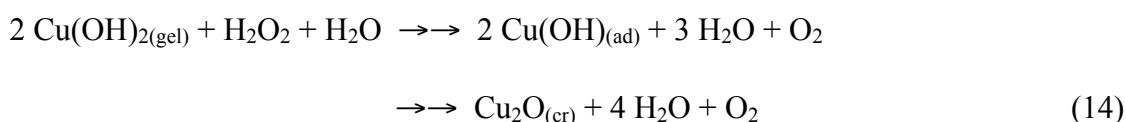
and by a solution reductant, if present, such as  $\text{H}_2\text{O}_2$ :



In Stage 2, because the solution near the surface is saturated with  $\text{Cu}^{2+}_{(\text{aq})}$  the oxidation pathway of  $\text{Cu}^I_{(\text{ad})}$  to  $\text{Cu}^{2+}_{(\text{aq})}$  (reaction 2) is no longer available. Thus, the production of  $\text{Cu}^I_{(\text{ad})}$  from  $\text{Cu(OH)}_{2(\text{gel})}$  in Stage 2 leads to primarily the growth of  $\text{Cu}_2\text{O}$  crystals ( $\text{Cu}_2\text{O}_{(\text{cr})}$ ).



The exact nature of  $\text{Cu}^I_{(\text{ad})}$  is difficult to characterize. It is possible that the reductive conversion of  $\text{Cu(OH)}_{2(\text{gel})}$  to  $\text{Cu}_2\text{O}_{(\text{cr})}$  may go through an intermediate step forming  $\text{CuOH}_{(\text{gel})}$  [6]:



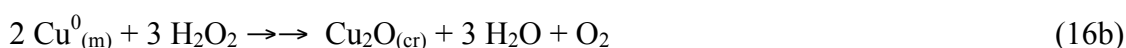
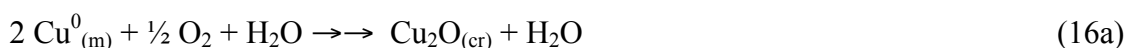
However,  $\text{Cu}_2\text{O}$  is thermodynamically more stable than  $\text{Cu(OH)}$  [7] and, if formed,  $\text{CuOH}_{(\text{ad})}$  will quickly convert to  $\text{Cu}_2\text{O}_{(\text{cr})}$ .

In Stage 2, the  $\text{Cu(OH)}_{2(\text{gel})}$  is continuously produced by the oxidation of  $\text{Cu}^0_{(\text{m})}$  to  $\text{Cu}^{2+}_{(\text{aq})}$  (process 5) followed by the precipitation of  $\text{Cu}^{2+}_{(\text{aq})}$  as  $\text{Cu(OH)}_{2(\text{gel})}$  (process 8). Hence, the amount of  $\text{Cu(OH)}_{2(\text{gel})}$  present on the crystal surfaces quickly reaches steady state. The thickness of the  $\text{Cu(OH)}_{2(\text{gel})}$  layer that covers the surfaces of  $\text{Cu}_2\text{O}_{(\text{cr})}$  remains constant as the  $\text{Cu}_2\text{O}_{(\text{cr})}$  crystals grow.

A small fraction of  $\text{Cu(OH)}_{2(\text{gel})}$  may be converted to  $\text{CuO}_{(\text{s})}$ , particularly if the surface becomes dehydrated before it can be reduced to grow  $\text{Cu}_2\text{O}_{(\text{cr})}$ :



The predominant corrosion pathway in Stage 2 is then:



In Stage 2 the copper corrosion leads mainly to the growth of  $\text{Cu}_2\text{O}_{(\text{cr})}$  with a thin layer of  $\text{Cu(OH)}_{2(\text{gel})}$ . Note that  $\text{Cu}_2\text{O}_{(\text{cr})}$  is a p-type semiconductor and the electrochemical reduction of  $\text{Cu(OH)}_{2(\text{gel})}$  can be coupled with the electrochemical oxidation of  $\text{Cu}^0_{(\text{m})}$  by transferring electrons through  $\text{Cu}_2\text{O}_{(\text{cr})}$ . That is, reactions (9) and (10) (or (13)) can occur with and without direct contact of  $\text{Cu(OH)}_{2(\text{gel})}$  with the metal substrate.

The  $\text{Cu}_2\text{O}_{(\text{cr})}$  growth mechanism via the reduction of  $\text{Cu(OH)}_{2(\text{gel})}$  has been observed and is supported by experimental evidence. For copper corrosion experiments performed in the absence of radiation with water droplets and small water volumes (1.5 mL), the growth of  $\text{Cu}_2\text{O}_{(\text{cr})}$  was observed once the dissolved copper concentration reached the solubility limit of  $\text{Cu}^{2+}_{(\text{aq})}$  (based on ICP-MS analysis of the dissolved copper in the test solution) [8-9]. Additionally, the crystal sizes and morphologies of  $\text{Cu}_2\text{O}$  formed during copper corrosion were similar to the crystals synthesized by the chemical reduction of cupric salts (hydrothermal

synthesis) [6-13]. In hydrothermal chemical synthesis, the production of  $\text{Cu}^+$  is generally accomplished by reduction of  $\text{Cu}(\text{OH})_2$  using a chemical reductant at a temperature typically higher than  $120\text{ }^\circ\text{C}$ . The starting solution containing  $\text{Cu}(\text{OH})_2$  as a colloid is prepared by dissolving a cupric salt (such as a sulphate, nitrate, or chloride) in a basic solution. The XPS analysis of the polyhedral  $\text{Cu}_2\text{O}(\text{cr})$  crystals formed during copper corrosion surfaces indicates that the surfaces of these crystals are covered by a few-nm layer of  $\text{Cu}^{\text{II}}$  species [14].

The transition from Stage 1 to Stage 2 occurs in a time scale significantly shorter than the durations of the two stages. This abrupt transition can be attributed to the fact that the nucleation of  $\text{Cu}(\text{OH})_{2(\text{gel})}$  particles from which  $\text{Cu}_2\text{O}(\text{cr})$  can grow is a stochastic event. The probability of particle nucleation increases with an increase in overall production of  $(\text{Cu}(\text{OH})_2 \cdot (\text{H}_2\text{O})_4)$  and an increase in the number of nucleation sites.

The duration of Stage 1 depends strongly on the ratio of solution volume to surface area as well as the solution pH. [15] The strong dependences arise because copper corrosion in Stage 1 consumes  $\text{H}^+$  while producing  $\text{Cu}^{2+}_{(\text{aq})}$ . Due to the pH dependence of  $\text{Cu}^{2+}_{(\text{aq})}$  solubility the saturation capacity of the solution decreases as corrosion progresses and pH increases. Thus, the corrosion time required to reach the saturation limit decreases faster than the increase in corrosion rate.

The time to reach the saturation limit also decreases with a decrease in the solution volume to surface area ratio. This could explain why the transition from Stage 1 to Stage 2 occurs at a much earlier time in a smaller volume of water if only the effect of the solution volume to surface area ratio on the rate of approaching the saturation limit is considered [15].

The water droplet corrosion experiments with radiation show that the  $\text{Cu}_2\text{O}(\text{cr})$  formation and growth starts from the circumferences or edges of the water droplets which then spread to



the centre. These observations are consistent with the strong dependence of time for saturation of the solution volume. Because of the smaller water volume to surface area ratio, the transition from Stage 1 to Stage 2 occurs earlier near the circumference than in the centre. Once nucleated, particles also grow preferentially from the nucleation sites. Hence, the earlier the nucleation occurs, the larger the  $\text{Cu}_2\text{O}_{(\text{cr})}$  crystals can grow over the same duration.

Due to their low surface hydration energy, metal hydroxides submerged in solution generally do not grow into coherent large crystals in the absence of complexing anions such as  $\text{SO}_4^{2-}$ ,  $\text{NO}_3^-$ ,  $\text{CO}_3^{2-}$ , etc. [16]. In the absence of other anions cupric hydroxide is also known to form a thin gel-like layer or aggregates of small particles, hence the term,  $\text{Cu}(\text{OH})_{2(\text{gel})}$  [17]. On the other hand, cuprous oxide can grow into large single crystals of polyhedral shapes [6-13]. Pure cupric hydroxide is blue while the cupric crystals of mixed hydroxide and anion are typically green [18]. The colour of  $\text{CuO}_{(\text{s})}$  is black. The colour of  $\text{Cu}_2\text{O}_{(\text{cr})}$  ranges from red to pink depending on the size of crystals [18].

The optical images (**Figure 5.4**, Chapter 5) show green deposits that appears to be a gel-like layer of  $\text{Cu}(\text{OH})_2$  deposited on top of  $\text{Cu}_2\text{O}$  oxide islands. The XPS analysis of the polyhedral  $\text{Cu}_2\text{O}_{(\text{cr})}$  crystals formed during copper corrosion surfaces also confirms that the surfaces of these crystals are covered by a layer of  $\text{Cu}^{\text{II}}$  species [14]. Under a continuous radiation flux, the radiolytically produced  $\text{H}_2\text{O}_2$  can act as a reductant converting  $\text{Cu}(\text{OH})_2$  to  $\text{Cu}_2\text{O}_{(\text{cr})}$  on the crystal surface.

The main corrosion product in Stage 2 is  $\text{Cu}_2\text{O}_{(\text{cr})}$  and the rate of  $\text{Cu}_2\text{O}_{(\text{cr})}$  growth represents the overall copper corrosion rate in Stage 2. Because the overall oxidation of  $\text{Cu}^0_{(\text{m})}$  to  $\text{Cu}_2\text{O}_{(\text{cr})}$  in Stage 2 does not involve protons or hydroxide ions, the pH of the solution will not change significantly with time in Stage 2.

As discussed earlier, the size and shape of  $\text{Cu}_2\text{O}_{(\text{cr})}$  change with time because of different crystal planes grow at different rates. The surface area perpendicular to the faster growing plane diminishes with time, and the crystals grow into shapes with slower growing crystal planes.

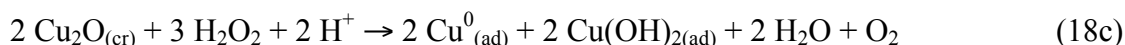
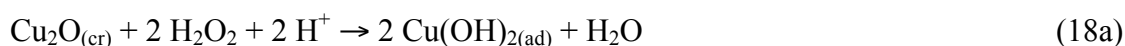
Thus,  $\text{Cu}_2\text{O}$  single crystals change their shapes from cubic crystals to truncated cubic, truncated octahedral and octahedral crystals as they grow [6-13]. Single crystals merge and form single-twin or multiple-twin or polycrystalline blocks.

### **Transition from Stage 2 to Stage 3:**

As the  $\text{Cu}_2\text{O}_{(\text{cr})}$  grows via the reductive conversion of  $\text{Cu}(\text{OH})_{2(\text{gel})}$  on the crystal surface,  $\text{Cu}_2\text{O}_{(\text{cr})}$  can also reduce back to  $\text{Cu}^0_{(\text{ad})}$  accompanied by its oxidation to  $\text{Cu}(\text{OH})_{2(\text{ad})}$ , which is the process known as a disproportionation reaction:



The disproportionation reaction can be accelerated in the presence of a redox active species that can switch from an oxidant to a reductant depending on its redox couple. For example, the reduction of  $\text{H}_2\text{O}_2$  to  $\text{H}_2\text{O}$  can couple with the oxidation of  $\text{Cu}_2\text{O}_{(\text{cr})}$  to  $\text{Cu}(\text{OH})_{2(\text{ad})}$ , while the oxidation of  $\text{H}_2\text{O}_2$  to  $\text{O}_2$  can couple with the reduction of  $\text{Cu}_2\text{O}_{(\text{cr})}$  to  $\text{Cu}^0_{(\text{ad})}$ :



(This acceleration can also occur in nitrate solutions because  $\text{NO}_3^-$  can oxidize  $\text{Cu}_2\text{O}_{(\text{cr})}$  to  $\text{Cu}(\text{OH})_{2(\text{ad})}$  while its reduction product  $\text{NO}_2^-$  can reduce  $\text{Cu}_2\text{O}_{(\text{cr})}$  to  $2 \text{Cu}^0_{(\text{ad})}$ .)

The products of the disproportionation,  $\text{Cu}^0_{(\text{ad})}$  and  $\text{Cu}(\text{OH})_{2(\text{ad})}$ , diffuse out from the crystal surface back into the solution phase.



The  $\text{Cu}(\text{OH})_{2(\text{ad})}$  is hydrated and dissolves into the solution phase.



This is the reverse process of the hydrolysis (reaction 6) and precipitation (process 8) of dissolved cupric ions.

The net result of the disproportionation reactions (17) is to reduce the size of  $\text{Cu}_2\text{O}_{(\text{cr})}$  which has the opposite effect to that of reactions (10) to (14). In Stage 2 when the overall oxidation of  $\text{Cu}^0_{(\text{m})}$  to  $\text{Cu}_2\text{O}_{(\text{cr})}$  via  $\text{Cu}(\text{OH})_{2(\text{gel})}$  (process 16) is still significant, the rate of formation of  $\text{Cu}_2\text{O}_{(\text{cr})}$  is faster than the rate of  $\text{Cu}_2\text{O}_{(\text{cr})}$  dissolution. The net result is the growth of  $\text{Cu}_2\text{O}_{(\text{cr})}$ . However, by the end of Stage 2 the metal substrate is extensively covered with thick  $\text{Cu}_2\text{O}_{(\text{cr})}$  crystals. The reduction of  $\text{Cu}(\text{OH})_{2(\text{gel})}$  coupled by the oxidation of  $\text{Cu}^0_{(\text{m})}$  either on the bare metal or on the oxide surfaces to grow  $\text{Cu}_2\text{O}_{(\text{cr})}$  becomes negligible, and the overall oxidation rate of  $\text{Cu}^0_{(\text{m})}$  approaches zero in Stage 3.

### **Stage 3:**

In Stage 3 the solution is saturated with  $\text{Cu}^{2+}_{(\text{aq})}$  and the overall production of oxides ( $\text{Cu}(\text{OH})_{2(\text{gel})}$  and  $\text{Cu}_2\text{O}_{(\text{cr})}$ ) is negligible. That is, the overall oxidation of copper metal is negligible and there is no more production of cupric or cuprous species. However, the  $\text{Cu}_2\text{O}_{(\text{cr})}$  disproportionation (reactions 17 and 18) continues to occur at an appreciable rate.

The disproportionation products formed on the crystal surfaces are  $\text{Cu}^0_{(\text{ad})}$  and  $\text{Cu}(\text{OH})_{2(\text{ad})}$ . These products are transported away from the surfaces by the momentum generated from the reactions forming the outer concentric ring pattern observed on the rectangular coupons after 72 h and 96 h of radiation exposure (Chapter 4). The metallic atoms are not stable in

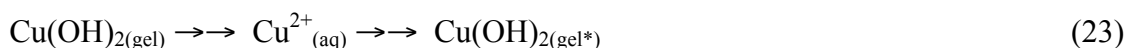
solution and hence are not likely to diffuse far; instead they quickly precipitate as solid particles ( $\text{Cu}^0(\text{s})$ ) on the surfaces near where they are formed:



The dissolved  $\text{Cu}^{2+}_{(\text{aq})}$  is transported further away before it precipitates back as  $\text{Cu}(\text{OH})_{2(\text{gel}^*)}$  but on the surface of a different  $\text{Cu}_2\text{O}_{(\text{cr}^*)}$  crystal:

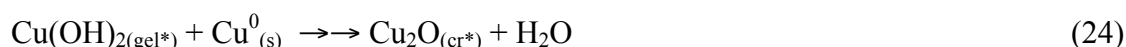


This process is the reverse of process (20) (via process 8). The net effect of processes (8), (20) and (22) is to transport  $\text{Cu}(\text{OH})_{2(\text{gel})}$  from one site to another, without changing the overall amount of  $\text{Cu}(\text{OH})_{2(\text{gel})}$  present on  $\text{Cu}_2\text{O}$  crystals:

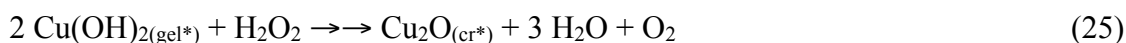


On individual crystals both the dissolution (process 20) and reprecipitation (process 22) of cupric hydroxide occurs but at different rates. The rate of dissolution is increasingly slower than the rate of reprecipitation as the size of  $\text{Cu}_2\text{O}$  crystal increases as discussed earlier. This leads to the redox-cycle-assisted ripening of  $\text{Cu}_2\text{O}$  crystals to be discussed below.

The  $\text{Cu}(\text{OH})_{2(\text{gel}^*)}$  formed is then reduced by  $\text{Cu}^0_{(\text{s})}$ :



and, if present, by a solution reductant (e.g.,  $\text{H}_2\text{O}_2$ ):



These are the same as reactions (10) and (11) in combination with reaction (12) except for they occur at different sites and grow different crystals.

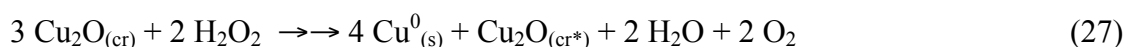
As in Stage 2, a small fraction of  $\text{Cu}(\text{OH})_{2(\text{gel}^*)}$  may be converted to  $\text{CuO}_{(\text{s}^*)}$ .

In the absence of a solution reductant, the overall process in Stage 3, consisting of elementary steps of reactions (17) and (19) to (23), is:

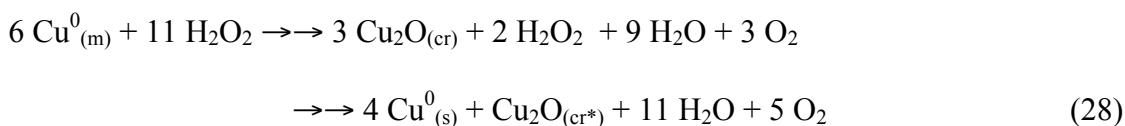


That is, in the absence of a solution reductant, the net rate of oxidation of  $\text{Cu}^0_{(\text{m})}$  is negligible, while the  $\text{Cu}_2\text{O}$  crystals formed in Stage 2 undergo ‘redox-cycle-assisted ripening’ [14]. That is, the larger  $\text{Cu}_2\text{O}$  crystals grow larger while the smaller crystals get smaller, without affecting the total amount of  $\text{Cu}_2\text{O}$  crystals present on the surface. The morphological evolution at the boundary of the circular coupons (**Figure 5.5**, Chapter 5) clearly demonstrates that  $\text{Cu}_2\text{O}$  crystal growth occurs by the ‘redox-cycle-assisted’ mechanism.

In the presence of a redox species such as  $\text{H}_2\text{O}_2$  that can switch from an oxidant to a reductant depending on the copper redox reaction that it can effectively couple with, the overall process, consisting of elementary steps of reactions (18), (19) to (22) and (24), is:



Thus, although the net oxidation of copper species is still zero and the redox-cycle-assisted ripening process occurs in Stage 3, the total amount of  $\text{Cu}_2\text{O}$  crystals decreases while producing metallic copper particles. The copper corrosion in this environment results in a slow transfer of metallic copper atoms from the metal phase ( $\text{Cu}^0_{(\text{m})}$ ) to form metallic particles ( $\text{Cu}^0_{(\text{s})}$ ):



## 6.2 Summary

The mechanism proposed in this chapter can explain the observed evolution of size and morphology of  $\text{Cu}_2\text{O}$  crystal growth mechanism and its effect on radiolytic corrosion of copper. The elementary reactions and transport processes included in the proposed mechanism help to

understand how the rates of the individual reactions can change as corrosion progresses, and how solution pH and redox environments can influence the kinetics of the individual reactions.

### 6.3 References

1. A.J. Brad, L.R. Faulkner, *Electrochemical Methods: Fundamentals and Applications*, 2nd Ed, John Wiley & Sons Inc., New York, 2001.
2. C.F. Baes, R.E. Mesmer, *Hydrolysis of Cations*, 2nd Ed, Krieger Pub. Co., Malabar, Florida, 1986.
3. J.R. Davis, *Copper and copper alloys*, ASM International, Materials Park, Ohio, 2001.
4. D.A. Palmer, *J Solution Chem.*, **2011**, *40*, 1067-1093
5. D.A. Palmer, P. Benezeth, *Solubility of copper oxides in water and steam*, 14th International Conference on the Properties of Water and Steam in Kyoto, 2004, 492-296
6. K. Chen, C. Sun, S. Song, D. Xue, *Cryst. Eng. Comm.*, **2014**, *16*, 5257-5267.
7. C.H. Kuo, M.H. Huang, *Nano Today*, **2010**, *2*, 106.
8. L. Huang, F. Peng, H. Yu, H. Wang, *Mater. Res. Bull.*, **2008**, *43*(11), 3047-3053.
9. J. Zhu, Y. Wang, X. Wang, X. Yang, L. Lu, *Powder Technol.*, **2008**, *181*(3), 249-254.
10. J. Zhu, H. Bi, Y. Wang, X. Wang, X. Yang, L. Lu, *Mater. Lett.*, **2008**, *62*(14) 2081-2083.
11. P. He, X. Shen, H. Gao, *J. Colloid Interface Sci.*, **2005**, *284*(2) 510-515.
12. Y. Sui, W. Fu, H. Yang, Y. Zeng, Y. Zhang, Q. Zhao, Y. Li, X. Zhou, Y. Leng, M. Li, G. Zou, *Cryst. Growth Des.*, **2010**, *10*(1), 99-108.
13. Y. Shang, L. Guo, *Adv. Sci.*, **2015**, *2*, 1-22.
14. M. Naghizadeh, A.M. Jean, G. Whitaker, J.M. Joseph, J.C. Wren, *to be submitted to Journal of Electrochemical Society*, 2017.
15. A.M. Jean, M. Naghizaheh, G. Whitaker, J.M. Joseph, J.C. Wren, *manuscript prepared for publication*, 2017.
16. M. Drogowska, L. Brossard, H. Menard, *Corrosion*, **1987**, *43*(9), 549-552.

17. H.W. Richardson, *Handbook of Copper Compounds and Applications*, Marcel Dekker, Inc., New York, 1997.
18. S. Budavari, *The Merck Index - An Encyclopedia of Chemicals, Drugs, and Biologicals*, Merck and Co. Inc., Whitehouse Station, NJ, **1996**, 446-448.



## Chapter 7

### Conclusions and Future Work

The evolution of surface morphology during water droplet corrosion of copper in the presence of  $\gamma$ -radiation was investigated using a water volume of 200  $\mu\text{L}$  on rectangular coupons. The copper metal coupons were exposed to a continuous flux of  $\gamma$ -radiation in an aerated environment for different durations. The oxide composition and morphology was analysed as a function of time. The study provided a qualitative approach to the oxide growth mechanism described in this thesis.

The effect of pH on the water droplet corrosion of copper was investigated by exposing copper metal to a 50  $\mu\text{L}$  water droplet as a function of irradiation time at two different pHs. The oxide growth kinetics were studied by measuring the amount of dissolved copper in the droplet as well as by analysing the morphology of the oxide formed on coupon surface as a function of time. For coupons corroded with pH 6.0 water droplets, the progression of the kinetic stages was slower than those corroded with pH 9.0 water droplets for both the inner and outer regions of the surface. The morphology of the inner and outer regions change with time, and the outer regions develop faster than the inner circle region for both pHs. The outer regions contained high-density areas of  $\text{Cu}_2\text{O}$  crystals, which formed oxide islands at long irradiation times as a result of redox-cycle assisted ripening. Redox-cycle assisted ripening was not observed in the inner regions of the surface, except after 96 h of irradiation for pH 9.0.

The dissolved copper concentration and surface morphology observed as a function of time indicated that water droplet corrosion of copper in the presence of  $\gamma$ -radiation occurs in

three stages. Stage 1 involves the radiolytic oxidation of  $\text{Cu}^0_{(m)}$  to  $\text{Cu}^{2+}_{(aq)}$ . The growth of  $\text{Cu}_2\text{O}$  particles occurs in Stage 2 as the solution near the surface becomes supersaturated with  $\text{Cu}^{2+}_{(aq)}$ . During Stage 3 the oxidation of the underlying metal substrate becomes negligible while the  $\text{Cu}_2\text{O}$  crystals grown earlier undergo redox-cycle assisted ripening.

The study showed that the duration of each stage depends on the water layer thickness and the solution pH. The initial pH of the water droplet has negligible effect on the corrosion kinetics in Stage 1. However, under the stagnant water droplet conditions, the solution in the outer region where the water layer is thinner becomes saturated earlier. The outer ring region reaches Stage 2 much earlier than the inner circle region. The solution pH has a stronger effect on  $\text{Cu}_2\text{O}$  crystal growth and ripening in Stage 2 and Stage 3. The progression through the kinetic stages is slower in the inner circle region than in the outer region, and slower at pH 6.0 than at pH 9.0.

This work has provided insight into the mechanism of  $\text{Cu}_2\text{O}$  formation and growth. The mechanism for  $\text{Cu}_2\text{O}$  formation and growth depends on several factors, and the reaction rates of the individual steps can significantly affect the growth of the  $\text{Cu}_2\text{O}$  particles and influence the final morphologies of the particles observed on the metal surface. The radiolytic oxidation of copper metal was studied as a function of pH, solution volume, and irradiation time. The effect of these parameters on the individual steps of the mechanism was discussed.

The non-uniformity of the surface morphology observed in different regions on the copper surface indicate that the corrosion of copper would be highly variable on a copper used fuel container exposed to radiation in the deep geologic repository. The studies presented in this thesis also showed that as irradiation time increases, the  $\text{Cu}_2\text{O}$  covers the surface uniformly, and

the metal/oxide interface becomes smoother and free of voids. However, long-term studies must be done in order to predict the corrosion behaviour of copper in DGR environments.

Future work for this project includes studying the effect of different anions in solution on the copper oxide formation and growth. Droplet corrosion of copper with nitric acid, sulphuric acid, and hydrochloric acid will be studied. The evolution of surface morphology was studied using nitric acid droplets as the test solution (pH 2.0) as part of this project, but the results of the experiments were not presented in this thesis. A manuscript that compares the effects of  $\gamma$ -radiation and different anions in solution on copper oxide formation and growth is being prepared for publication.

The next step will then be to develop a kinetic model to simulate the oxide growth based on the kinetic stages discussed in Chapter 6. This model will be useful for simulating the corrosion of copper metal under radiolytic conditions. The model would also be useful for optimizing parameters and reaction conditions to control  $\text{Cu}_2\text{O}$  crystal growth to yield  $\text{Cu}_2\text{O}$  crystals with a desired morphology.

## Arielle M. Jean

### EDUCATION

---

**Western University**, London, ON, Canada April 2017

*Master of Science, Specialization in Physical and Analytical Chemistry*

- Thesis: Evolution of Cu<sub>2</sub>O Morphology During Copper Corrosion in the Presence of Gamma-Radiation (Supervisor: Dr. Clara Wren)
- Relevant coursework: Radiation Induced Chemistry, Spectroscopy & Microscopy in Materials Research

**Western University**, London, ON, Canada May 2014

*Bachelor of Science, Specialization in Chemistry*

- Thesis: Fabricating and Analyzing Thin Films in CZTS Solar Cell Devices (Supervisor: Dr. Zhifeng Ding)
- Relevant coursework: Chemical Research Discovery & Scientific Communication, Instrumental Analytical Chemistry, Advanced Analytical Chemistry

### ACADEMIC EXPERIENCE

---

**Western University**, London, ON, Canada September 2014 - December 2016

*Graduate Research Assistant*

- Theoretical and practical knowledge of spectroscopy, microscopy, and chromatography instrumental techniques: Raman, FT-IR, UV-Vis, SEM, TEM, GC-MS, HPLC, TLC, IC
- Designed experiments, developed experimental procedures, and carried out experiments
- Communicated technical findings using written reports and oral presentations to a wide range of audiences, using Microsoft Word, PowerPoint, and other data visualization tools

**Western University**, London, ON, Canada September 2014 - December 2016

*Graduate Teaching Assistant*

- Demonstrated experimental techniques and the use of laboratory instrumentation and software to undergraduate students

### PUBLICATIONS

---

- (2017) Evolution of Cu<sub>2</sub>O Morphology During Copper Corrosion in the Presence of Gamma-Radiation (*manuscript in progress for publication*)

### CONFERENCES AND PRESENTATIONS

---

- (2016) Presented at the Canadian Nuclear Society (CNS) Student Conference (Toronto, ON)
- (2015) Presented at the University Network of Excellence in Nuclear Engineering (UNENE) R&D Workshop (Toronto, ON)
- (2015) Presented at the Nano Ontario Conference (Ottawa, ON)
- (2015) Attended the National Association of Corrosion Engineers (NACE) Student Symposium (Toronto, ON)
- (2014) Presented at the Southern Ontario Undergraduate Student Chemistry Conference (SOUSCC) (Windsor, ON)

### OTHER ACTIVITIES & INTERESTS

---

**Canadian Nuclear Society (CNS)**, Member 2016 - Present

**Women in Nuclear (WiN) Canada**, Member 2016 - Present